A Smoothed Particle Hydrodynamics Model for the Simulation of Laser Fusion Additive Manufacturing Processes

by

Marc Russell

A dissertation submitted in partial satisfaction of the
requirements for the degree of
Doctor of Philosophy

in

Engineering-Mechanical Engineering

and the Designated Emphasis

in

Computational Data Science and Engineering

in the

Graduate Division
of the
University of California, Berkeley

Committee in charge:

Professor Tarek Zohdi, Chair
Professor Hayden Taylor
Professor Per-Olof Persson

Spring 2018

A Smoothed Particle Hydrodynamics Model for the Simulation of Laser Fusion Additive Manufacturing Processes

Abstract

A Smoothed Particle Hydrodynamics Model for the Simulation of Laser Fusion Additive Manufacturing Processes

by

Marc Russell
Doctor of Philosophy in Engineering-Mechanical Engineering

University of California, Berkeley

Professor Tarek Zohdi, Chair

Additive Manufacturing (AM), aka 3D-Printing, is a broad class of rapidly emerging manufacturing technologies that build-up parts layer-by-layer through the addition of raw materials, under the guidance of a digital model. They are set to revolutionize the manufacturing world by allowing for rapid production of net-shape, customizable, ready-to-use parts in a variety of novel materials and designs. The development of numerical methods suited to the simulation of AM processes to aid in the optimization of current technologies and in the creation of new methods is of prime importance to industry and academia.

In this work, the Smoothed Particle Hydrodynamics (SPH) method, a Lagrangian mesh-free numerical scheme, is adapted for the first time to resolve thermal-mechanical-material fields in a range of Laser Fusion Additive Manufacturing processes. The method is capable of simulating large-deformation, free-surface melting, flow, and re-solidification of metallic materials with complex physics and material geometries. A novel SPH formulation for modeling isothermally-incompressible fluids, which allows for the accurate simulation of thermally driven liquid metal expansion/contraction, is presented and verified. Fundamental validation of the methodology is performed via comparison with real world, spot laser welding experiments. The methodology is then used to investigate the the specific Additive Manufacturing Process of the Selective Laser Melting of Metallic, micro-scale Particle Beds. The physics of a track deposition process is explored through numerical experiments and the influence of processing parameters on the finished laser weld track quality is investigated. The unique abilities of using a Lagrangian mesh-free method, as opposed to continuum numerical schemes, to model this process is highlighted. The SPH method is found to be a viable and promising numerical tool for simulating laser fusion driven Additive Manufacturing processes.

I would like to dedicate this work to my family and friends.

Contents

List of Figures

List of Tables

List of Acronyms

AM	Additive Manufacturing
SLM	Selecitve Laser Melting Process
SPH	Smooth Particle Hydrodynamics Method
WC	Weakly Compressible Formulation

Acknowledgments

Marc Russell acknowledges the support of the National Science Foundation. This material is based upon work supported by the National Science Foundation Graduate Research Fellowship.

Chapter 1

Introduction

1.1 Overview of Numerical Modeling in Engineering

In industry, broadly speaking an engineer can be classified as holding one of three roles: a Designer, an Analyzer, or a Builder/Tester. A designer's job is to create a design of a process/part/etc., an analysis engineer's job is to evaluate the design an ensure its functionality, and a build/test engineer will manufacture the design and ensure its correctness. Of particular interest to this body of work is the role of the Analysis Engineer. There are many tools for an Analyst to call upon in their work; from text-book equations to physical experimentation, or even gut experience. However for the modern engineer, the most ubiquitous tool is that of a Computer Model/Simulation.

A computer model allows an engineer to simulate/predict a real world event solely in the digital realm of a computer. A computer simulation replicates reality by solving mathematics formulae that model natural laws; a basic example being solving the motion of an apple falling from a tree using Newton's Law, $Force = Mass * Acceleartion$. As with a physical experiment, data can be obtained from these computational experiments. This data can be analyzed, results obainted, and ultimately real world design choices made. A diagram of this process is shown in Figure 1.1for the case of a 3D printed part. Analysis of a 3D printing machine/process is desired to make real world improvements; for example a smooth part finish. A numerical model, which is composed both of mathematical formulae that describe the natural laws governing the physics of 3D printing as well as computer models (aka numerical models) that can be used to solve these highly complicated mathematical equations, are used to create a computer simulation of the process, in this case extruding hot plastic out of a nozzle. Data can be gathered from this process, analyzed, and then used to suggest real world changes that can lead to real world process improvements.

There are numerous reasons why numerical modeling is used/preferred over traditional physical experimentation. (1) It can be significantly cheaper. Computational expenses are much lower then real-world expenses; e.g. it is cheaper to crash test a digital vehicle model then a real vehicle. (2) It allows for greater insight and data collection then a real world experiment. In a digital model one has precise information throughout the problem domain at all times, for example; its possible to know the temperature inside a digital model of cast part while this would be impossible to obtain in the real world. (3) Optimization processes are faster when using numerical models as several iterations of design can be tested with minimal effort. (4) Finally, numerical models can simulate processes that are just impossible to experiment on in the real world; for example the collision of two stars or the landing of a rover on Mars.

Numerical modeling is of course not without faults. Simulations are not perfect replications of the real world, they are merely very close approximations. They must be validated heavily by comparison with physical experiments before they can be trusted. In addition, they are incapable of simulating everything. For some physical phenomena, we don't have the necessary mathematical or numerical models to model them. For others, the computational resources to solve existing numerical models are too great. However,

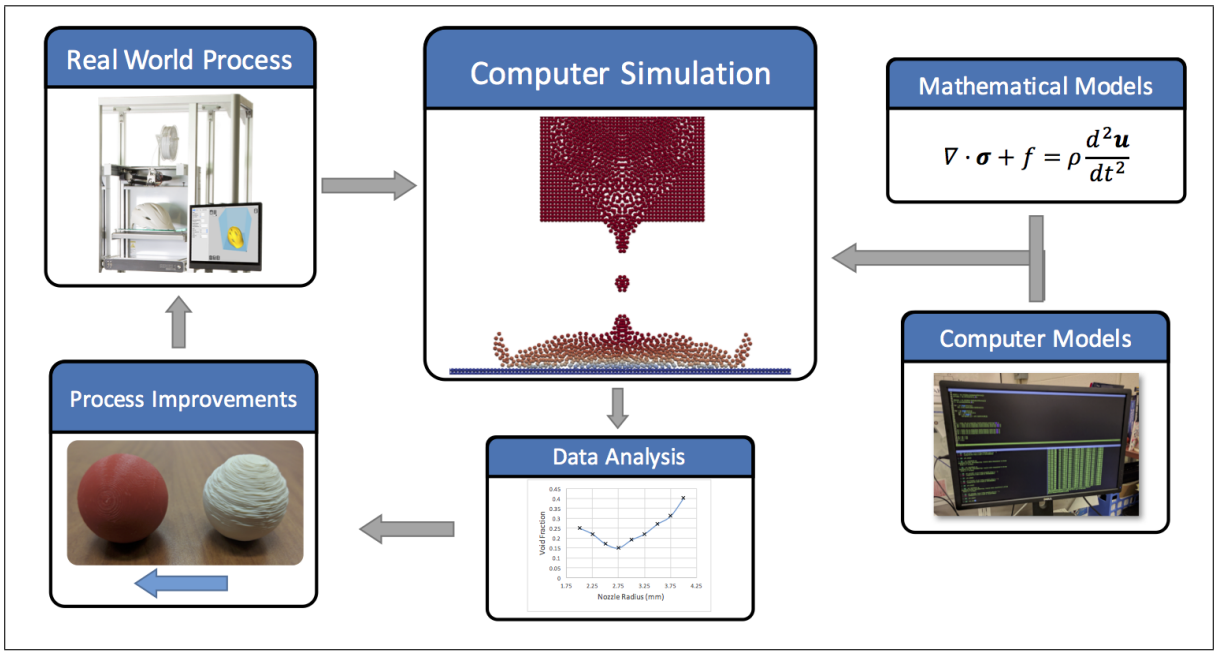

Figure 1.1: Flow chart indicating role of computer simulation in Engineering Analysis of a real world process, in this case 3D printing.

with more and more research being undertaken in the field and the development of ever better computer technologies, the range of real world events that are possible to simulate will only grow.

The goal of this work is provide another tool in the toolbox of an Engineering Analyst. A numerical method capable of simulating the real world Additive Manufacturing processes will be developed, validated, and implemented to suggest real-world process improvements.

1.2 Application of Interest: Additive Manufacturing

Additive Manufacturing (AM) is a set of rapidly emerging manufacturing technologies that will revolutionize the manufacturing world by allowing for rapid production of net-shape, customizable, ready-to-use parts. The umbrella term Additive Manufacturing covers a broad range of novel manufacturing processes that build-up of parts layer-by-layer through the addition of raw materials, under the guidance of a digital model. This is in opposition to traditional manufacturing processes in which material is removed, e.g. milling, or a fixed net shape is created in a single process, e.g. injection molding/casting. AM development has been spurred on by the need in the engineering industry for rapid prototyping, flexible design options to create more complex part geometries, and to build with novel materials. AM techniques have many benefits over traditional manufacturing

methods including: (a) single step processing of complex parts (b) creation of functionally gradient and novel designs (c) reduction of production time, and (d) minimized material waste[44]. For these reasons and many more, AM methods are rapidly gaining interest in industry, government, and academia.

The American Society for Testing and Materials group (ASTM) categorizes the various AM processes into seven classes: (1) vat photo-polymerization, (2) binder jetting, (3) material extrusion, (4) material jetting, (5) sheet lamination, (6) powder bed fusion, and (7) direct energy deposition[1, 26]. A complete decscitption of each of the classes is given below:

- VAT Photo-polymerization: Selective curing of liquid resin in a vat via a heat source, usually UV/laser
- Binder Jetting: Selective addition of bonding agent droplets to join deposited raw materials
- Material Extrusion: Selective deposition of heated raw material through a scanning nozzle, later cooling into a solid body
- Material Jetting: Selective deposition of raw material droplets onto a surface.
- Sheet Lamination: Layer by layer deposition of raw material sheets upon one-another.
- Powder Bed Fusion: Selective melting/sintering of fine powders in a bed layer-by-layer using a controlled heat source, e.g. a laser
- Direct Energy Deposition: Selective simultaneous deposition and heating of raw material, usually in powder or wire form, using a controlled heat source attached to the novel head.

In general, these processes involve extremely complicated, rapid thermo-mechano-material-chemical fields acting on complex geometries with length scales from the micrometers to meters. In addition they can be implemented on a wide range of materials; ceramics, metals, plastics, organics, as well as hybrids of these. They have been adopted by several industries from aerospace (3D printed rocket engines), to the automotive industry (customized engine components), to biology/medical (e.g. 3D printed organs and custom medical implants), and even the food industry(3D printed food). The field is growing rapidly and with its expansion, there is a growing need to be able to understand the complex phenomena occurring in these processes to both improve existing AM technologies as well as develop news ones.

A strong tool in accomplishing this goal are numerical simulations. Numerical models are capable of providing insight into physics of these processes as they allow for precise data collection of the thermo-mechano-material-chemical fields through-out the entire

process domain. This will allow researchers/developers to precisely identify controlling features in these process and appropriately adjust process inputs to optimize the final part design. In addition the ability to run hundreds of models simultaneously make optimization of process parameters trivial.

Of particular interest to this thesis is the numerical modeling of AM process that involve the heating, liquifying, and subsequent cooling of deposited raw material to create a finalized part(Material Extrusion and Powder bed fusion process in particular). These processes often involve extreme cooling/heating rates, extremely volatile liquid free surfaces, rapidly evolving material/state boundaries, and large material movement and as such are difficult to adequately and efficiently model using traditional numerical methods. In this work, a relatively new numerical method, the Smooth Particle Hydrodynamics Method, which is typically used for large scale fluid flows will be applied to the simulation of these types of AM process, in particular the selective laser melting of metallic particles bed.

1.3 Motivation of Work

Selective Laser Melting (SLM) is a particularly promising AM technique for producing complex, 3D, metallic structures through a repetitive process of deposition and guided laser melting of an atomized metallic particle bed (Figure 1.2}). Subsequent layers are melted into previously deposited layers to produce 99.9% density parts with feature sizes of $200\mu m$[29]. Applications for the process are widespread including customizable porous bone implants and die tooling for one-off runs, with the aerospace and defense industry particularly interested in using the method to cut production times and cost for complex metallic components. Use of SLM parts however, currently requires a lengthy process of part qualification and certification to detect processing flaws including high residual stresses, porosity, disconnected layers, and undesired microstructures[29]. A better understanding of SLM is required to minimize these defects and allow for its full adoption by industry.

Powder bed SLM, however, involves extremely complex and coupled physical-metallurgical processes (melting and solidification, inter-particle conduction and radiation, laser heating, material expansion/contraction, recoil pressure, mechanical stresses, wetting and dewetting, sintering, Marangoni convection, capillary forces, vaporization, etc.) occurring at micro time-and-length scales. Relying on physical experimentation alone to understand and improve the process would be too costly, time consuming, and complex. Numerical simulation, validated by physical experimentation, provides a means of both effectively understanding and optimizing the process by allowing for in-situ analysis as well as efficient optimization of process parameters.

While traditional (continuum) based numerical methods (FEM, FVM) are capable of producing high fidelity solutions and have been adapted to AM modeling, and SLM in particular[37], they are ill-suited (computationally expensive) for simulating AM processes

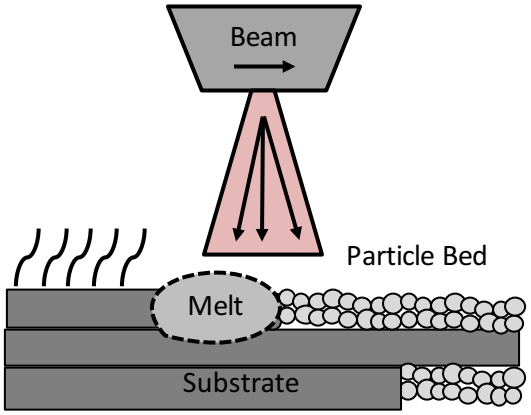

Figure 1.2: Schematic of SLM process.

which typically involve free-surfaces and material interfaces with significant and complex movement. It is believed the Smooth Particle Hydronamics (SPH) method, a mesh-free Lagrangian particle method, can offer approximate solutions at a fraction of the cost of traditional numerical methods.

In the present work, the SPH method is adapted to accurately resolve thermal, mechanical, and material fields in a wide range of AM process with particular focus on the SLM process. Fundamental validation of the proposed methodology as well as, for the first time, application of the SPH methodolgoy to simulating to practical, real-world AM processes will be preformed.

Chapter 2

Background Theory

2.1 Smooth Particle Hydrodynamics Method

The Smooth Particle Hydrodynamics (SPH) is a numerical method for obtaining approximate solutions to systems of physically inspired differential equations over a problem domain. It was developed by Gingold and Monaghan in 1977[27] as a hydrodynamic code to simulate astronomical motions. Since then, its simulation capabilities have been expanded to a wider range of thermal-mechanical-material-chemical problems. SPH is a meshless (mesh-free) numerical method which discretizes the problem domain into a set of Lagrangian numerical particles with no a-priori connectivity. Interpolation between these sets of particles is used to discretize the governing differential equations and determine the thermal-mechanical-material fields existing over each particle (e.g. their motion, temperature, material properties...etc). The particles represent distinct entities of mass and hence the scheme is Lagrangian in nature. Various analytical forms of the interpolant exist, and their forms have a variety of impacts on the solution, as will be discussed later. Spatial derivatives of the interpolated values, used to discretize the governing differential equations, are obtained using methods of calculus and statistical approximation of values over the particles.

Meshed vs Mesh-Free Methods In meshed methods, a continuum domain is divided(or discretized) into a discrete subdomains where the nodes (or grid points) of these subdomains are connected in a pre-defined manner(the mesh). The governing equations are converted to a set a algebraic equations that solve for the field variables the the nodal locations. The methods have been proven very efficient and useful for a wide range of numerical problems. However, the need to maintain the physical compatibility condition(in the case of Eulerian meshes across the nodal boundaries) or the need to maintain a well defined mesh(the case of of Lagrangian meshes) can create significant computational expenses in problems dealing with free surfaces, deformable boundaries, moving interfaces, and large deformations.

Meshfree methods, such as SPH, on the other hand rely on the discretization of governing physical equations over a set of randomly distributed nodes with no apriori connectivity. Connectivity is established in each time step through a neighbor search in a region of influence. Connectivity is fluid and ever-changing allowing for reliable simulation of problems with large deformations, splits, and moving interfaces.

2.1.1 Derivation of the Fundamental SPH Discretization

2.1.1.1 Integral Kernel Approximation, Smoothing Function, and Particle Approximation

The derivation of the SPH numerical discretization is a three step process. (1) The value of a primary variable is exactly represented by an integral interpolation of the form;

$$f(\mathbf{x}) = \int_{\Omega} f(\mathbf{x}')\,\delta(\mathbf{x}-\mathbf{x}')\,dV' \tag{2.1}$$

where $f(\mathbf{x})$ is the primary variable, Ω the entire problem domain, $\delta(x)$ the Dirac delta, and dV' a differential volume element. This integral smoothing form is the basis of the method and is similar to the weak form of certain continuum methods. (2) The infinite domain integral is next reduced to a finite domain integral by approximating the Dirac delta function by a smoothing function $W(\mathbf{x}-\mathbf{x}', h)$ that exists over a finite smoothing domain Ω_S,

$$f(\mathbf{x}) \approx \langle f(\mathbf{x})\rangle = \int_{\Omega_S} f(\mathbf{x}')\,W(\mathbf{x}-\mathbf{x}', h_{sml})\,dV' \tag{2.2}$$

where h_{sml} is the smoothing length, and $\langle\cdot\rangle$ indicates an integral approximation of a value. The smoothing length controls the size of the compact support domain, also known as the domain of influence of the smoothing function. This compactness ensures that the approximation of $f(x)$ is given only by local neighboring values, allows for practical implementation of the method, and as will be shown increases the order of accuracy of the method. The compactness requirement is generally formulated as.

$$W(\mathbf{x}-\mathbf{x}', h) = 0 \;\; for \;\; (\mathbf{x}-\mathbf{x}') \geq 2h_{sml} \tag{2.3}$$

The smoothing length is chosen as a factor of the initial mesh spacing, dx,

$$h_{sml} \approx \alpha \cdot dx$$

where the factor α is commonly chosen to be in the range of 1.1 *to* 1.5.

Sometimes $W(\mathbf{x}-\mathbf{x}', h))$ is referred to as the smoothing kernel and Eq. 2.2the kernel approximation.

Smoothing kernels, in general, should also preserve unity over the smoothing domain,

$$\int_{\Omega_S} W(\mathbf{x}-\mathbf{x}', h)\,d\mathbf{x}' = 1 \tag{2.4}$$

, therefore guaranteeing that a constant function can be recovered, C^0 consistency, as well as be smooth, symmetric, positive, and decay away from $\mathbf{x}$. Various analytical forms for the smoothing function that meet these requirements can be found in the literature. The choice of smoothing kernel can significantly impact the accuracy and stability of an SPH simulation([17]). Specifically, the shape of the first and second derivatives of the smoothing function are important in ensuring the physicality of the smoothing function. For this work the Wendland C2 kernel[69] was used,

$$W_{C2} = \begin{cases} \alpha\,(DIM)\left(\frac{1-q}{2}\right)^4 (2q+1) & q \leq 2 \\ 0 & q > 2 \end{cases} \tag{2.5}$$

where α is the normalization factor for the $2D$ and $3D$ forms of the kernel,

$$\alpha(DIM) = \left\{(-), \frac{7}{4\pi h^2}, \frac{21}{16\pi h^3}\right\}$$

and where $\mathbf{q} = (\mathbf{x} - \mathbf{x}')/h_{sml}$.

The first derivates of W_{C2} are given as,

$$\frac{\partial W_{C2}}{\partial \mathbf{x}} = -5\alpha\left(1 - \frac{q}{2}\right)^3 q \frac{(\mathbf{x} - \mathbf{x}')}{|\mathbf{x} - \mathbf{x}'| h_{sml}}.$$

A recent comparison of a variety of popular kernel functions by W. Dehnen and H. Aly[17] showed the Wendland C2 to be the optimal kernel for preserving simulation stability, hence its use in this work.

(3)The third and final step in deriving the SPH discretization is to transform the kernel approximation, Eq. 2.2, into a summation over neighboring particles. First, note that Eq. 2.2 can be re-written as an integral over masses instead of volume,

$$\langle f(\mathbf{x})\rangle = \int_{\Omega_S} \frac{f(\mathbf{x}')}{\rho(\mathbf{x}')} W(\mathbf{x} - \mathbf{x}', h)\rho(\mathbf{x}')\, dV' = \int_{\Omega_S} \frac{f(\mathbf{x}')}{\rho(\mathbf{x}')} W(\mathbf{x} - \mathbf{x}', h)\, dm'.$$

Recalling that SPH particles are Lagrangian we can therefore approximate this integral as a summation over distinct mass elements, in this case neighboring SPH particles,

$$\langle f(\mathbf{x})\rangle \approx \sum_{j=1}^{N} \frac{f(\mathbf{x}_j)}{\rho_j} W(\mathbf{x} - \mathbf{x}_j, h)\, m_j, \tag{2.6}$$

where N is the total number of neighboring particles within the compact radius and $(\cdot)_j$ the value of $(\cdot)$ at particle j. This final equation is referred to as the particle approximation or summation approximation, and is the fundamental discretization used within SPH.

Figure 2.1 shows the smoothing function profile and neighboring particles for a given location, in this case particle i ,

The calculation of primary variable values in SPH is simply a matter of summing over the values of neighboring particle scaled by the smoothing function value at their locations. For example the temperature at x can be given as;

$$T(x) \approx \sum_{j=1}^{N} \frac{m_j}{\rho_j} T_j W(\mathbf{x} - \mathbf{x}_j, h).$$

2.1.1.2 First Derivative Discretizations

Particle approximations for the derivatives of a function can be obtained using the divergence theorem and the product rule. We start with the kernel approximation for the derivative of the function;

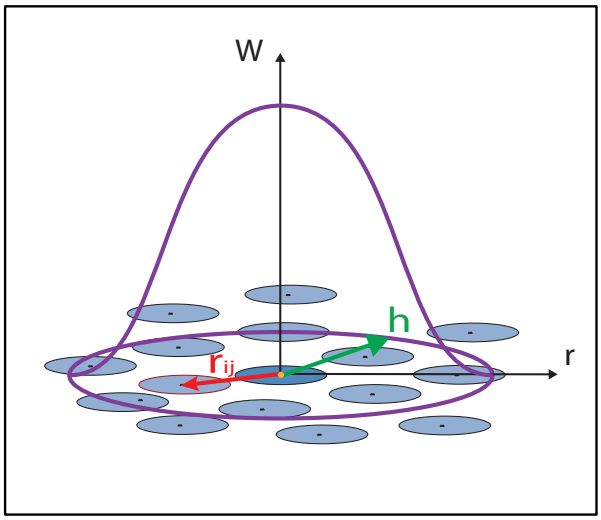

Figure 2.1: Schematic of SPH smoothing function.

$$\langle \nabla f(\mathbf{x}) \rangle = \int_{\Omega_S} \nabla f(\mathbf{x}') W(\mathbf{x} - \mathbf{x}_j, h) \, dV'.$$

We can expand this using the product rule ,

$$\langle \nabla f(\mathbf{x}) \rangle = \int_{\Omega_S} \nabla \left(f(\mathbf{x}') W(\mathbf{x} - \mathbf{x}_j, h) \right) dV' - \int_{\Omega_S} f(\mathbf{x}') \nabla W(\mathbf{x} - \mathbf{x}', h) \, dV',$$

and using the divergence theorem, re-write the first term as a surface integral with normal $\mathbf{n}$

$$\langle \nabla f(\mathbf{x}) \rangle = \int_{\partial\Omega_S} f(\mathbf{x}') W(\mathbf{x} - \mathbf{x}_j, h) \, \mathbf{n} dV' - \int_{\Omega_S} f(\mathbf{x}') \nabla W(\mathbf{x} - \mathbf{x}', h) \, dV'.$$

Due to the compact support requirement on the smoothing function, Eq. 2.3, in general $W(\mathbf{x} - \mathbf{x}_j, h) \to 0$ on $\partial\Omega_s$ and hence the first term disappears leaving,

$$\langle \nabla f(\mathbf{x}) \rangle = - \int_{\Omega_S} f(\mathbf{x}') \nabla W(\mathbf{x} - \mathbf{x}', h) \, d\mathbf{x}' \tag{2.7}$$

which can be written in the particle approximation form,

$$\langle \nabla f(\mathbf{x}) \rangle \approx \sum_{j=1}^{N} \frac{m_j}{\rho_j} f(\mathbf{x}_j) \nabla W(\mathbf{x}_i - \mathbf{x}_j, h). \tag{2.8}$$

This is the fundamental SPH discretization for the first derivative of a function. The SPH discretization transfers the derivative requirement from the primary function to the

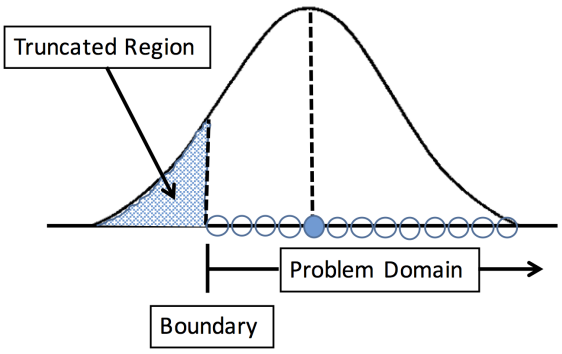

Figure 2.2: Loss of support of smoothing function near the problem boundary.

smoothing function making its calculation trivial. The assumption that $W(\mathbf{x}-\mathbf{x}_j,h)\to 0$ on $\partial\Omega_s$, however, only holds true in the interior of the domain. On the domain boundaries, $W\neq 0$ and hence $\int_{\Omega_S} W dx' \neq 1$ and $\int_{\partial\Omega_s} f(x) W n dx' \neq 0$, as demonstrated in Figure 2.2. This leads to errors in the approximation which will be discussed in more detail later. Using the first derivative particle approximation, we can discretize many of the governing differential equations, for example the continuity equation,

$$\frac{D\rho}{Dt} = -\rho\nabla\cdot\mathbf{v}$$

can be discretized as;

$$\frac{D\rho}{Dt} = -\rho_i \sum_{j=1}^{N} \frac{m_j}{\rho_j}\mathbf{v}_j \frac{\partial W_{ij}}{\partial \mathbf{x}_i}.$$

2.1.1.3 Second Derivative Discretizations

There are numerous methods for SPH discretization of second order derivatives. As a first approach, second order derivatives can be derived much in the same manner as the first order derivatives, removing the differentiations off the primary variable and placing them on the smoothing function;

$$\left\langle \nabla^2 f(\mathbf{x}) \right\rangle \approx \sum_{j=1}^{N} \frac{m_j}{\rho_j} f(\mathbf{x}_j)\, \nabla^2 W(\mathbf{x}_i-\mathbf{x}_j,h)\, \Delta V_j$$

. This form however is known to have several undesirable issues including sensitivity to particle disorder and a lack of positivity[53]. The sign of $\nabla^2 W(\mathbf{x}_i-\mathbf{x}_j,h)$ can flip with increasing particle separation leading to unphysical behavior in a system, for example, heat flow from colder to warmer regions[53].

A second method of discretizing second derivatives in the SPH methodology is through nested first derivatives;

$$\langle \nabla \left(\nabla f \left(\mathbf{x} \right) \right) \rangle \approx \sum_{j=1}^{N} \frac{m_j}{\rho_j} \nabla f \left(\mathbf{x}_j \right) \nabla W \left(\mathbf{x}_i - \mathbf{x}_j, h \right)$$

where,

$$\langle \nabla f \left(\mathbf{x} \right) \rangle \approx \sum_{j=1}^{N} \frac{m_j}{\rho_j} f \left(\mathbf{x}_j \right) \nabla W \left(\mathbf{x}_i - \mathbf{x}_j, h \right).$$

This scheme is easy to implement and maintains positivity of the kernel, however it can lead to oscillating instabilities(checker-boarding) in stiff problems and can rapidly increase the computational costs of the scheme as now two sets of neighbor summations must be preformed[22, 45].

A final, and the most popular, method of handling second derivatives is to preform both derivative operations in the same kernel but to implement one of the derivative operations on the smoothing function algebraically;

$$\left\langle \nabla^2 f \left(\mathbf{x} \right) \right\rangle \approx \sum_{j=1}^{N} \frac{m_j}{\rho_j} \left(f \left(\mathbf{x}_j \right) - f \left(\mathbf{x}_i \right) \right) \frac{\nabla W \cdot \left(\mathbf{x}_i - \mathbf{x}_j \right)}{\left| \mathbf{x}_i - \mathbf{x}_j \right|^2}. \tag{2.9}$$

This method is more stable then the previous two and in addition maintains a low computational cost. While this is the most basic form, numerous variations of the algebraic discretizations exists for the various second derivative terms that appear in physical models, e.g. heat conduction, diffusivity; etc.. These variations have more desirable properties and will be covered in more detail in the next Chapter.

2.1.2 Accuracy and Stability of SPH methods

The SPH method is considered to a be a lower order numerical method. Its theoretical limit on the order of accuracy is approximately $\mathcal{O}\left(h^2\right)$. As I will discuss, this order of accuracy is often difficult to guarantee in practice. When considering the accuracy of the method care must be taken to distinguish between the consistency guaranteed by the Integral Form of the method, Eq. 2.2&2.7, and the consistency of the subsequent Particle Approximation, Eqs. 2.6&2.8. It possible to analytically derive the consistency of the integral form, however outside of a regular structured grid (rarely preserved in practice) the consistency of the particle approximation is impossible to guarantee in an analytical manner. However, confirmation of adequate consistency in practice via mesh-refinement studies or comparison with validation problems has proven the accuracy of the SPH method[53].

2.1.2.1 Consistency of the Integral Form

In the ideal case, the regular Smoothed Particle Hydrodynamics method (SPH) can be considered to have accuracy of $\mathcal{O}(h^2)$, or 1st order consistency, i.e. it can accurately model polynomials up order 1. The proof is as follows:

We begin with the standard SPH kernel approximation for a function $f(x)$:

$$\langle f(x)\rangle = \int f(x')\, W(x'-x,h)dx'$$

Taking the taylor series expansion we get

$$\langle f(x)\rangle = \int \left[\left\{f(\mathbf{x}) + f'(\mathbf{x})\,(\mathbf{x}-\boldsymbol{x'}) + \mathcal{O}\left(h^2\right)\right\} W\,(\boldsymbol{x'}-\mathbf{x},h)\right] dx'$$

Recalling the conditions on the smoothing function of unity, Eq. 2.4, and of symmetry, or evenness; and that $(\mathbf{x}-\boldsymbol{x'})$ is an odd function we can show:

$$\langle f(x)\rangle = f(\mathbf{x})\cancelto{1}{\int W\,(\boldsymbol{\xi}-\mathbf{x},h)\,d\xi} + f'(\mathbf{x})\cancelto{0}{\int \left[(\mathbf{x}-\boldsymbol{\xi})\,W\,(\boldsymbol{\xi}-\mathbf{x},h)\right] d\xi} + \mathcal{O}\left(h^2\right)$$

$$\langle f(x)\rangle = f(\mathbf{x}) + \mathcal{O}\left(h^2\right) \Rightarrow 2^{nd}\ Order$$

Likewise for the derivative of f, taking the product rule, applying the divergence theorem, and recalling our condition of compactness on the smoothing function we get:

$$\begin{aligned}
\langle \nabla f\,(\boldsymbol{\xi})\rangle &= \int \nabla f\,(\boldsymbol{\xi})\, W\,(\mathbf{x}-\boldsymbol{\xi},h)\,d\xi \\
&= \int \nabla\cdot\left[f\,(\boldsymbol{\xi})\, W\,(\mathbf{x}-\boldsymbol{\xi},h)\right] d\boldsymbol{\xi} \\
&= \cancelto{0\ ;\ compact}{\int_{\delta\Omega} f\,(\boldsymbol{\xi})\, W\,(\mathbf{x}-\boldsymbol{\xi},h)\cdot\mathbf{n}dA} - \int_{\Omega} f\,(\boldsymbol{\xi})\,\nabla\cdot W\,(\mathbf{x}-\boldsymbol{\xi},h)\,d\boldsymbol{\xi} \\
&= -\int_{\Omega} f\,(\boldsymbol{\xi})\,\nabla\cdot W\,(\mathbf{x}-\boldsymbol{\xi},h)\,d\boldsymbol{\xi}
\end{aligned}$$

To which we can apply the same proof as before to establish $\mathcal{O}(h^2)$ accuracy. Similar proofs are available for higher order derivatives. In practice, however, the standard SPH formulation fails to achieve the stated second order accuracy due to a failure to meet the conditions that were set on the smoothing function. Truncation of the smoothing function on any open boundary can lead to: (1) Failure to meet unity (guarantee C^0 of $\langle f(x)\rangle$) , (2) Failure to meet symmetry (guarantee C^1 of $\langle f(x)\rangle$) , and (3) Failure to meet compactness requirement (guarantee C^1 of $\langle \nabla f(x)\rangle$). Inaccuracies on the boundary can propagate into the interior of the domain affecting accuracy everywhere.

To overcome these failings, novel forms of the integral approximation have been developed to restore consistency to the SPH formulation on boundaries to at least $\mathcal{O}(h)$.

These sometimes have specific forms related to the physical nature of the quantity (or its derivative) which is being derived. A commonly used technique for restoring consistency is the Shepard Kernel[62]. It involves a renormalization of the integral approximation using the integral of the kernel;

$$W_S\left(\mathbf{x}-\mathbf{x}',h\right)=\frac{W\left(\mathbf{x}-\mathbf{x}',h\right)}{\Gamma\left(\mathbf{x}\right)} \tag{2.10}$$

where the renormalization factor $\Gamma\left(\mathbf{x}\right)$ is the integral of the smoothing function;

$$\Gamma\left(\mathbf{x}\right)=\int_{\Omega}W\left(\mathbf{x}-\mathbf{x}',h\right)dV'. \tag{2.11}$$

This methods uses the inconsistency error in calculating $\Gamma\left(x\right)$ to offset the error in the calculation of the integral approximation of a function. Randles & Libersky [58], re-derived this kernel form, and used it for restoring the first order consistency of the $\langle f(x)\rangle$ discretization on a free surface boundary[45],

$$\langle f(x)\rangle_S=\frac{1}{\Gamma\left(x\right)}\int f\left(\mathbf{x}'\right)W\left(\mathbf{x}-\mathbf{x}',h\right)dV'. \tag{2.12}$$

Collagrossi [11] showed that for case where a physical property is known to be zero on the boundary (e.g. pressure on a free surface) the Shepard Kernel restores $\mathcal{O}\left(h\right)$ accuracy to the integral approximation to the gradient on the boundary;

$$\langle \nabla f(x)\rangle_S=-\frac{1}{\Gamma\left(x\right)}\int f\left(\mathbf{x}'\right)\nabla W\left(\mathbf{x}-\mathbf{x}',h\right)dV'. \tag{2.13}$$

.

More complex methods exists for restoring the consistency of a wider variety of SPH kernel operators on the boundary including the Moving Least Squares-SPH method developed by Dilts[18, 19], Randles and Libersky renormalization scheme for the calculation of divergence[59], and the integral kernel correction proposed by Bonet and Lok[5]. These methods are very successful at restoring the consistency of SPH operators however they come at extra, not insignificant, numerical costs which makes there use only viable in simulations that require extreme accuracy on the boundary.

2.1.2.2 Consistency of the Particle Approximation

While its possible to satisfy the requirements for full consistency at the integral approximation level, there is no guarantee that consistency will hold when these integral approximations are translated to to the particle/summation approximation(Eqs. 2.8 & 2.6). In fact, in general the particle approximation forms of the consistency requirements;

$$\sum_{j=1}^{N}\frac{m_j}{\rho_j}\left(\mathbf{x}-\mathbf{x}_j\right)W_{ij}=0;\quad symmetry \tag{2.14}$$

and

$$\sum_{j=1}^{N} \frac{m_j}{\rho_j} W_{ij} = 1; \quad unity \tag{2.15}$$

are not satisfied due to the presence of particle disorder. For a regularly spaced mesh, these requirements are met, but in any practical simulation, the relation of particles to one another will fluctuate and evolve making it impossible to guarantee the satisfaction of Eqs2.15&2.14. Some particles may have unsymmetric neighboors or not enough/too many neighbors to satisfy unity. This has led many authors to declare the classical SPH method unusable as a numerical method[45]. However in practice the order of errors resulting from a disorderly mesh are often much lower then predicted[53]. This is because the particles will often maintain some amount of order, due to the physics they are being used to model, while overall their positioning may seem disordered. In general the error from a lack of consistency is often much lower then assumed.

2.1.2.3 Accuracy of Practical Simulations

In classical mesh based methods, were some level of mesh order is preserved, its possible to devise closed form estimations on the order of error of the method. This is not possible for mesh-free methods such as SPH. The randomness of the particles motion and the every evolving connectivities of particle make such estimations impossible. Instead, SPH practitioners have had to rely on comparison of results to analytical solutions or physical experiments, or mesh convergence studies to ascertain the order of accuracy. This method of practical verification of the method has proven the SPH method to be significantly more accurate then one would expect from the hypothesized lack of consistency. The reasons for this have been proposed to be two fold[53]. First, as mentioned above, the level of disorder in an SPH mesh is often smaller then expected meaning errors in accuracy are minimal. Secondly, the use of conservative forms of the SPH formulas, those that conserve physical properties like momentum and energy, minimize the effects of discretization errors. The model can still track the correct solution due to the conservative nature of the method even if discretization errors exists. In this author's opinion, the numerous examples of the practical and accurate application of the SPH method to physical problems prove its accuracy to a sufficient degree.

2.1.3 SPH Simulation of Incompressible Fluids

All material flows in AM processes are incompressible. There are two main methods for the simulation of incompressible fluids using SPH, the Incompressible SPH method (ISPH) and the Weakly-Compressible SPH method (WCSPH).

The ISPH method, developed by Cummins et al.[14], is an adaption of the classical projection-scheme for the solving of the incompressibility constraint on the fluid. Its a two step process where the velocity is advanced in time by ignoring the constraint

pressure, and then corrected by projecting it onto an incompressible space (usually a velocity divergence free space). The method requires the solution of the matrix Poisson-Pressure Equation(PPE) which can be computationally intensive.

The WCSPH method, first introduced by Monaghan[52], solves the compressible Navier-Stokes equations with a very stiff equation of state to maintain nearly constant density. Small fluctuations in density produce large corrective pressures which maintain pseudo-incompressability. The stiffness is generally a function of the max velocity in the fluid and is chosen to keep density fluctuations less then 1%. WCSPH fluids have a corresponding strict CFL condition.

In general the WCSPH method is more popular then the ISPH method. The WCSPH is more reliable and stable when compared to ISPH as it only weakly enforces the incompressibility requirement. In terms of speed of computation, the ISPH method can allow for larger time steps to be taken then WCSPH but it has the added computational effort of solving the pressure-poisson matrix equation which is not insignificant. For most problems, the CFL conditions on WCSPH are not strict enough to render the method significantly slower then ISPH (however this is not always true). Most importantly, unlike ISPH, the WCSPH method is trivially parallelizable significantly increasing its speed of operation and is easier to implement.

An early noted downside of the WCSPH method however was that the use of the method resulted in small, locally fluctuating density errors. These local errors could lead to globally incorrect values . The $\delta - SPH$ method was developed to remove these fluctuations and preserve the accuracy of the WCSPH formulation. The method works by smoothing out the fluctuations in the density field via the addition of a diffusion term to the continuity equation. A more in-depth description of the method will be provided later in this work. A $\delta - SPH$ WCSPH scheme was used in this work.

2.2 Selective Laser Melting Process

2.2.1 Process Overview

The metallic Selective Laser Melting (SLM) process is a powder bed fusion Additive Manufacturing process for producing full density, complex, 3D, metallic/metallic-composite parts through a repetitive process of deposition and guided laser melting of an atomized metallic particle bed. A schematic of a typical SLM machine is shown in Figure 2.3. The SLM process is as follows:

1. Setup
   (a) A digital part file is “sliced” using manufacturing algorithms into a series of 2D scan profiles.
   (b) A scaffolding is secured to the part bed and the apparatus filled with inert gas.

2. Build

   (a) Microscale spherical material powders (metallic/composite) are evenly distributed in a single layer(multiple particles in thickness) onto the part bed from a powder reserve, with either a wiper blade, roller, or alternative system.

   (b) A scanner systematically directs a laser beam over the surface of the particle bed in the profile of the 2D "slice" for that layer. The laser melts the particles into a melt pool that penetrates into the previously solidified under-layers, joining the two upon cooling.

   (c) Once the 2D profile for a layer is completed, the particle bed is incrementally lowered one layer thickness.

   (d) The process is repeated until all layers are completed.

3. Post processing

   (a) Upon completion, the un-melted powder left in the part bed is removed and potentially recycled.

   (b) Thermal cycling, surface polishing/milling can be used to improve the state of the finalized part

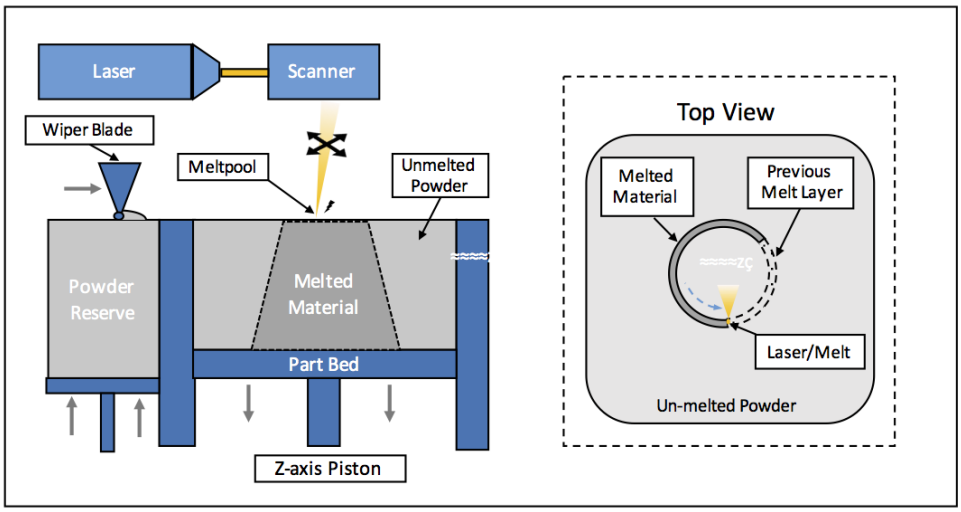

Figure 2.3: Schematic of a typical SLM machine is given on the left. A top view of a ringed slice being printed on the particle bed is shown on the right.

The result of this process is a fully dense (99.9% density) part with resolution in the range of $200\mu m$[29]. Typical particle diameters used in the process are in the range of $20\mu m - 60\mu m$. Laser powers can vary on the order of $10W - 1000W$ with scan speeds from $0.5\frac{m}{s} - 5\frac{m}{s}$. A variety of laser types are used including Ytterbium fibre laser, Nd :

YAG laser, Continuous wave fibre laser[29]. In addition a variety of material types can be used with SLM including Al, Fe, Cu, Ni, and Ti alloys in addition to Ceramic-Matrix-Composites[29].

SLM is highly desired by a variety of industries for numerous reasons. First it reduces time and cuts the cost of manufacturing small-run, high complexity 3D metallic components. For example, a full-scale aerospace engine component printed by Lawrence Livermore National Labs in 8 days using SLM at a fraction of the cost of traditional manufacturing methods is shown in Figure 2.4. Cost and time reductions are mainly achieved via minimization of labor/machining time through single step processing of parts eliminating the need for multiple machine/setups. For example, the eyelets on the engine component in Figure 2.4would traditionally need to be affixed separately as weldments and the component remounted to complete machining. Such a process is time consuming and expensive while for SLM they can be added directly during the single build process. In the future, further cost reductions can be achieved through a minimization of material waste as AM process only place material where it is needed. The SLM engine component in Figure 2.4 highlights an additional, highly-desirable unique feature of SLM , the ability to easily create novel part designs that are un-manufacturable with traditional techniques. The engine component features internal cooling pores down the length of the interior of the nozzle. These pores would be impossible to create using for example a casting process but are trivial to produce using SLM. A second unique attribute of the SLM processes is the ability to functionalize a component by altering the composition of the component as its printed. For example the thermal conductivity of the rocket engine could be increased towards the base while lowered towards the tip via the inclusion or exclusion of highly conductive particles in the powder bed. A final unique benefit of SLM is that it allows for on-site manufacturing of a wide variety of components due to its small machine footprint(current machines are about the size of two refrigerators) and its ability to create any component shape. On-site manufacturing can lower transportation time/costs as well as allowing for parts to be manufactured previously impossible locations, e.g. at sea or in space.

Beyond the afore mentioned utilization by aerospace/military industries, the mold making industry and medical industry are also very interested in using SLM technology. SLM can be used to make custom molds for plastic extrusion processes cheaper and quicker then current methods. The medical industry could use SLM to improve orthopedic-implants by customizing them each patient. A patient specific metallic skull implant is shown in Figure 2.4. The use of SLM printed implants can increase the success of medical operations without signifiacntly increasing cost.

However, the current use of SLM parts by industry is limited due to the existence of hidden processing flaws in the components(voids, cracks, etc.) and low manufacturing reliability, accuracy/tolerance, functionality, and reproducibility of the process. At the moment the SLM process is not “plug and play” and extra-efforts (machine tuning, multiple prints, extensive post-processing, etc.) are required to successfully produce components. In order for complete adoption of SLM by industry, a greater understanding of

(a) SLM aerospace engine component[34].

Fig 6. Radiographic (postero-anterior) showing the position and stabilization of the implant 2 year later. Symmetry in width and orbital size is obtained.

(b) SLM skull implant for facial reconstruction[16].

Figure 2.4: Two applications of SLM use by industry.

the complex link between the process parameters, the physical processes they induce, and the outcome of the manufactured part (accuracy, flaws, etc.) must be made. This is the goal of current research efforts in the area, including this work.

2.2.2 SLM Physical Processes Overview

Powder bed SLM involves complex thermal-mechanical-material physical processes occurring at multiple length scales: part, feature, and powder-melt scale. The success of a print is heavily influenced by these processes and a thorough understanding of them is necessary to devleop a proper numerical model. A description of the relevant physics, as they are currently understood, will be presented below. Focus will be placed on the powder-melt scale as this is the scale of interest for this thesis however it should be understand the the SLM process is a multi-scale problem, occurring at the part level, feature level, and the powder/melt scale.

Powder-Melt Scale Fundamental to SLM is the conversion of microscale powders of material into a continuous solid part using a laser-source. A laser is usually scanned in a semi-continuous manner to melt adjacent lines of powder, which upon cooling, form into a continuous track of solid material. Track width is controlled by the physics of

the process and process parameters, predominantly the laser power/scan speed, and is usually on the order of $50 - 200\mu m$. A schematic of a typical process of creating a melt track is shown in Figure 2.5. (A) The laser beam is scanned over a section of newly deposited particles heating them to their melting point. (B) The powders melt forming a melt-pool that penetrates into the previously deposited substrate layer. The laser beam is then advanced in the track direction and a combination of laser and melt-pool conductive/convective heating melts oncoming powder material. (C) As the laser beam sources passes on a region, the liquid melt pool there cools through heat conduction into the substrate and radiation, eventually solidifying. Voids can occur if vapor is trapped within the melt pool upon solidification.

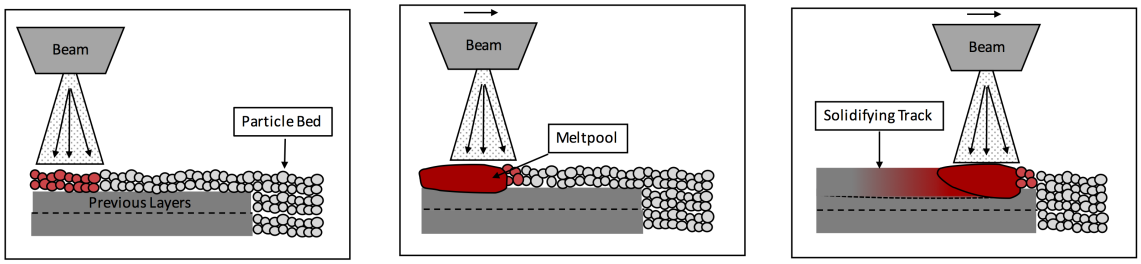

(a) (b) (c)

Figure 2.5: Schematic of an SLM track lasering process.

The shape and depth of this melt track is heavily controlled by numerous coupled thermal-mechanical-material phenomena. These are listed by field in Table 2.1.

The mechanical field is dominated by a highly complex melt flow motion, strongly driven by Marangoni convection and thermal expansion of the fluid. Velocities in the melt pool can be on the order of $1m/s$ over a diameter of $\sim 100\mu m$. The liquid melt is inviscid and incompressible. High normal surface tension forces result from the high surface tension coefficient for liquid metals, $\sigma \approx 1.500\frac{N}{m}$, and small curvature of the melt pool. In addition extreme Marangoni convection is induced by significant thermal gradients and large $\frac{\partial\sigma}{dT}$ values for liquid metal. The Marangoni convection drives the melt flow from the laser spot (hottest location) to the rear of the melt pool (coolest location). The shape of the free surface, which is highly volatile due to the low fluid viscosity influences the direction of the Marangoni convection motion. At high-enough rates of laser heating a switch from a conductive melt pool to a laser "keyhole" type melt pool can occur[39]. Keyholing occurs when the melt pool reaches vaporization temperatures. The vaporizations leaves a cavity in the melt pool and produces significant vapor-recoil pressure. This results in an opening of the melt pool as fluid is pushed to the edges allowing for deeper laser "drilling" and a greater melt pool penetration. Extreme cooling rates, on the order of $10^3 - 10^8\ K/s$, can result in significant thermal/residual stresses and mechanical failure(cracking/disbonding)[29]. The cooling solid can experience elasto-plastic strains and residual stresses. Finally, the melt pool and oncoming powders can be

Field	Phenomena
Mechanical	· **Viscous-Incompressible Fluid Flow** · **Capillary Forces** · **Marangoni Convection** · **Thermal Expansion** · Powder Flow/Ejection · Recoil Pressure · Buoyancy · Elasto-Plastic Solid Deformation of Substrate · Residual/Thermal Stresses · Mechanical Failure (cracking, disbonding)
Thermal	· Particle Bed (PB)**laser absorption**/ scattering /emmitance · **Melt Laser Absorbtion** · **Melt Radiation** · **Convective & Conductive Heating Melt** · **Convective & Conductive Heating PB** · **Conduction Substrate** · Solid Work Heating · External Convective Cooling
Material	· **Melting-Solidification** · **Thermal Dependence** · Vaporization · Ablation · Microstructure Formation · Mushy Zone properties

Table 2.1: A list of the mechanical-thermal-material field phenomena occurring in the melt pool. Listed in bold are the phenomena modeled in this work.

ejected ahead of the melt pool resulting in splattering.

The thermal field is a complex mix of laser surface heating, surface radiative cooling, melt convection/conduction, conduction in the particle bed, and conduction into the substrate layer. The laser absorption process varies spatially and temporally. In the particle bed, laser ablation, scattering, and emission among the particles determine the rate of laser absorbtion. Material absorptivity is a function of material state and temperature and evolves significantly over the process. However, unfortunately little data is available for the material absorptivity of the liquid state as function of temperature due to the difficultly in obtaining it. Finally, work heating can occur in the melt flow. Even though the fluid viscosity is low, the melt speeds are significant and shear heating is possible.

The material state is extremely complicated as-well. The extreme rate of laser heating and subsequent cooling induces rapid phase changes from solid to liquid to gas over minute time scales. In addition a large mushy zone can occur between the melt and substrate. Thermal dependence in combination with the vast temperature ranges of the SLM process (around $293K - 6000K$) result in significant variation of the material properties over the SLM process. Significant density changes and material hardening and softening can occur. The strength, and for steel materials the sign, of the Marangoni convection coefficient is dependent on temperature. Extreme rates of cooling of the melt pool can lead to anisotropic microstructures and hence directionally oriented material properties. These microstructures can evolve over subsequent heating cycles as layers are added upon each other further complicating the material state.

Overall within each field, several forms of phenomena exist and influence the physics of the track formation process. A strong coupling between the fields, also complicates the situation.

Feature Scale Several tracks can be combined to create part features using SLM, for example overhangs, holes, or even flat regions. The layering of tracks can create thermal cycling and a complex thermal-material-mechanical history for the part. Of primary importance are the interactions of the thermal and mechanical fields to create residual stresses in the part. Extreme cooling through the track substrate causes rapid contraction of the newly deposited layer and high residual stresses, and potentially micro cracking, at this scale. Material microstructure is ever evolving as subsequent heating of layers through deposition of new material on top of them leads to an ever evolving microstructure.

Part Scale At the part scale, the thermal state is controlled by conduction through the part geometry, conduction through the surrounding unmelted particle bed, and heat addition at the source location. The distribution of temperatures at this scale can lead to significant thermal/residual stresses developing and cracking at the part scale. The material properties are influenced by the feature scale processes.

2.2.3 SLM Process Improvement: The Need for Numerical Modeling

While several industries have already adopted SLM technology, the current use of SLM manufactured parts requires significant part qualification post manufacturing to detect hidden processing flaws: (1) micro-cracking, (2) disbonded/discontinuous layers, (3) voids, (4) undesirable microstructures, (5) residual stresses, (6) and macro-cracks. Micro-cracks form at the feature/track scale of the part. They are the result of thermally induced localized residual stresses. While they may not be visible post-manufacturing, they can cause premature failure of SLM parts by serving as initiation sites for fatigue induced macrocracks. Disbonded/discontinuous layers and voids are also sources of fatigue failure (Figure 2.6a). They can result from a lack a melt pool penetration, violent melt pool motion creating trapped vapor pockets or unmelted particles, and the spheroidisation of long liquid melt tracks from Rayliegh-Taylor instabilities commonly referred to as balling (Figure 2.6b). Prevention of the balling process is a major focus of research efforts. The high rate of cooling in SLM can result in anisotropic microstructures making prediction of part properties difficult[29]. Residual stresses are possible due to extreme thermal activity and state changes that occur during SLM. They can occur at all scales of the SLM process from the micro-scale track level to the macro-scale part level (Figure 2.6c).

In addition to these flaws, current SLM technologies are unable to reliably produce parts to 100% accuracy of a CAD model design. Each part may require several print iterations, and an intuition based tuning of the machine process to be produced correctly and to the desired tolerance. This hands-on tuning requirement hampers the ability of the SLM process to produce highly customizable components on demand and in short time frames.

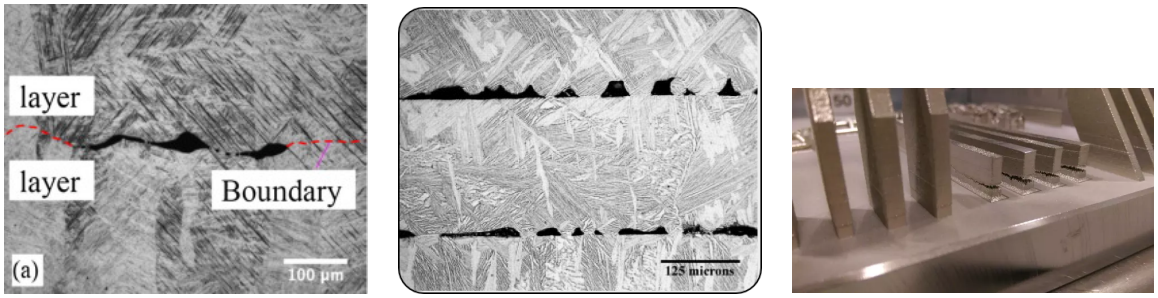

(a) Microscale defects in a Ti SLM part [7].

(b) Balling defect between track layers in a steel SLM part [29].

(c) Part scale cracking of a steel SLM manufactured part[21].

Figure 2.6: Examples of flaws/defects in SLM parts.

The goal of current SLM research efforts is to provide a fundamental understanding of how to overcome these flaws and successfully print components through optimization of process parameters. This is challenging due to the significant number of process parame-

ters involved in the SLM process. A list of them is provided by Sun et al. [64], shown in Figure 2.7.

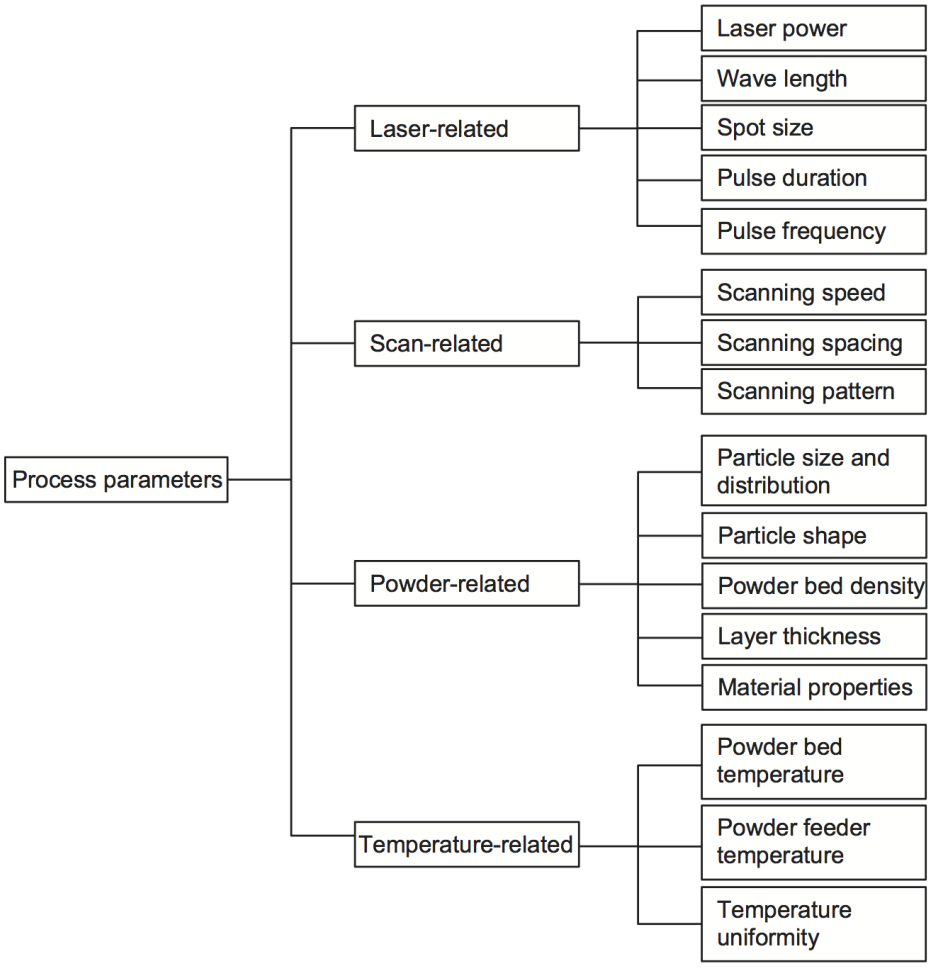

Figure 2.7: A list of SLM process parameters compiled by Sun et al. [64].

The significant number of parameters involved makes tuning and improvement of the SLM process difficult. Relying on physical experimentation alone to understand and optimize the process would be too costly, time consuming, and complex. Numerical simulation has two significant benefits over traditional physical experimentation for researching the SLM process. First, it allows for in-situ analysis of the microscale laser melting process and the gathering of data that is impossible with physical experiments. For example, in a physical experiment it would be impossible to know precisely the size and temperature of the melt pool during a given lasering experiment. This information is generated for all time and at every location within a numerical method and could be easily gathered and analyzed. Secondly, optimization is significantly easier and cheaper with numerical methods as opposed to physical experiments. Through parallelization and optimization

algorithms, hundreds of digital models can be run and a processes tuned for a given machine, part design, and material choice at a fraction of the time and cost it would take to do so in the physical world. For these reasons and more, there have been significant research efforts in the area of computer modeling of the SLM process.

2.3 State of the Art: SLM Numerical Modeling

As SLM is a multi-scale phenomena, a variety of numerical methods operating at multiple scales(part, feature, and track/melt) are necessary to fully capture the process. Any complete simulation tool used to model SLM would need to be a multi-scale, multi-methodology model that feeds information between the part-feature-track scales to adequately capture the process. Most methods at the part and feature scale are continuum-mesh based methods. There have been several promising efforts using FEM to model the physical process at these scales, e.g. Hodge et al. [33]. The focus of this current work however is the track/melt scale, an arguably harder problem with more complex physics and material/state movement. A summary of current research efforts at this scale will be given and argument for the use of the SPH method to address simulation will be presented. Finally a review of past research efforts in the SPH community that are simmillar to the research efforts in this work will be covered.

State of the Art in SLM Simulation Over the past few years, several efforts have been made to model SLM at the particle and melt scale using continuum mesh-based numerical methods. Initial work focused on using homogenized models with analytical equations for powder bed heating and melting. These models were inherently ineffective at modeling the flow mechanics of physically in-homogenous powder beds. More recent works solved continuum discretization of physical laws on a meshed particle bed geometry. One of the earliest of these efforts was that of Khariallah et al. [37] in 2014 at Lawrence Livermore National Lab. They simulated the problem using an in-house Eulerian FEM package (Diablo) developed for thermo-mechano-material simulation efforts at the national lab. They used an analytical laser absorption scheme developed by Gusarov et al [30] and solved for the deformation of the solid substrate layer. They included most of the relevant physics but neglected Marangoni convection. While highly-accurate their simulation time for a $1mm \times .3mm \times .3mm$ section of material was on the order of $100,000\ CPUhrs$. They noted this was the result of the CFL condition imposed by solution of the mechanical field in the body as we well as the need to track the complex free-surface and solidification surfaces with the Eulerian scheme. Khariallah et al.[38] (2016) increased the fidelity of their model through the inclusion of additional physical phenomena. They included Marangoni convection, recoil pressure, and a simplified (no reflection) ray tracing scheme. They argued the inclusion of these phenomena is necessary in order to correctly simulate the SLM process at the track scale. They validated their code through comparison with experimental track melt geometries. They are able to pro-

vide great insight into the physical processes occurring at the microscale during an SLM process and confirm experimental findings. No information on the computational cost was provided. A recent work by Lee & Zhang [42] used a commercial FD-VOF code to simulate the laser beam melting of a particle bed geometry similar to that of Khariallah et al.. A DEM scheme was used to place the particles in the bed and the FLOW-3D VOF code used to solve their melting and flow. They reported significant efficiency increases over the FEM code of Khariallah et al, solving a similar sized problem in 40 CPU hrs. However they appeared to implement less physics, failed to report information about their numerical scheme and the chosen time step conditions, and failed to validate against physical experiments. In addition their results were counter to some of the findings of Khariallah et al. [38]. Complete reviews of research effort into the computer modeling of SLM were preformed by Schoinochoritis et al. [61] and King et al. [40].

In addition to continuum methods, there have also been attempts to use microscale mesh-based numerical methods, such as the Lattice Boltzmann (LBM), with e.g. Korner et al. [41]} using LBM to model the laser melting processes specifically. However LBM has numerous limitations for such problems including the need for a fine lattice-mesh to accurately capture the melt motion as well as an unclear methodology for modeling some of the thermal effects in the energy equation [41]}.

Finally, in addition, alternative mesh-free methods have been applied to laser-particle bed AM applications, with Ganeriwala & Zohdi [25] and Zohdi [72]using the Discrete Element Method (DEM) to model the process. It was observed that the DEM method was useful for modeling the powder deposition and heating process prior to melting but was unable to accurately model the liquid-melt pool motion.

Motivation for SPH /Current Work It is proposed that the application of meshless techniques to the study of the SLM process can provide results at a fraction of the computational cost of mesh-based methods and serve as a design-tool for industry. The SPH method is a natural and effective means for modeling SLM, and AM processes in general, as free surfaces, mass conservation, material state boundaries, and large material movement are handled implicitly by the methodology. SPH methods are easily parallelizable and can complete with traditional numerical methods in simulating a wide variety of free surface fluid motion situations. SPH discretizations of fundamental physical laws, e.g. Balance of Linear Momentum and the First Law of Thermodynamics, for a number of materials and phases have been implement and verified. In addition SPH formulations for the wide variety of physical phenomena apparent in the SLM process (phase change, surface tension, etc.) have been implemented to some degree.

There have even been some efforts in the SPH community to model laser based manufacturing processes. Hu et al. [35] modeled the melting process in laser spot melting of Aluminum with SPH. In another work, they also considered metal vaporization as a consequence of the laser induced heating [35]. Although these works are relevant, they lacked the full physics required to simulate AM process as well as validation by comparison with physical experiments. Another interesting work by Alshaer et al. [3]focused

on the ablation of metal layer with pulsed laser. However this work mostly focused on the ablation component and didn't seek to preform melt pool simulations. SPH has been applied to other manufacturing processes as well with varying degrees of success including high pressure die casting (Cleary et al. 2007 [10]) and thermal spray coatings (Zhang et al. [70]). Its believed that enough numerical groundwork exists to adapt the SPH methodology to the simulation of AM processes and in particular the SLM process. This adaption is covered in the following chapter.

Chapter 3

AM-SPH Methodology

A novel SPH methodology capable of simulating thermal-mechanical Additive Manufacturing(AM) processes (in particular the Selective Laser Melting(SLM) of metallic particle beds) was developed in this work. It combines previously established SPH discretizations from disparate fields for the first time while supplementing them with novel formulations necessary for laser based AM simulations. While this author believes the current rampant use of acronyms in the SPH field is inappropriate, for the sake of succinctness, and to reflect its intent, the proposed methodology of this work will be referred to as AM-SPH within this thesis.

As covered in Section 2.2.2, numerous physical phenomena occur at the microscale during the SLM process. Simulating all these phenomena would be well outside the scope of this thesis as well as unnecessarily increase model complexity and reduce efficiency. Only the most relevant of the numerous physical phenomena will be modeled. These are highlighted in bold in Table 2.1.

Referring to the mechanical field phenomena in Table 2.1, of primary importance to this work is the flow, shape, and properties of the melt pool. These directly determine the quality of the melt track and the success of track depositions. Powder flow/ejection is incapable of being simulated by the current model but could be modeled efficiently using a coupled Discrete Element Method scheme[71]. Buoyancy is difficult to model accurately using the Weakly Compressible formulation in SPH and is negligible over the time scale of the problem so it excluded. Elasto-Plastic solid deformation is ignored because of the strict CFL condition required for simulating solid mechanics. Its also assumed that the deformation of the solid body is minimal compared to the liquid flow and as such can be neglected. The modeling of solid deformation is only relevant for predicting material failure from thermal/residual stresses which is outside the scope of this work. Other researchers have addressed this problem and note the prohibitive time step that modeling the solid phase puts on the simulation[37]. Not bolded in Table 2.1 but of importance at higher laser powers is the recoil pressure caused by material vaporization. The temperatures of the melt under the laser source exceed the boiling point of steel and the energy loss from vaporization has been noted by Khariallah et al [38] as primary source of heat loss in the melt. The vaporization phenomena was not included in this model due to time constraints but can be implemented through a material damage parameter and vaporization energy sink term.

Referring to the thermal field phenomena in Table 2.1, of prime importance is the heat flow in the melt pool and conduction into the substrate. Such information can determine the extent of material heating and be fed into macroscale models. Solid work heating is minimal for SLM and is ignored as the solid deformation is minute. External convective cooling could be easily added but real world values are unavailable to this author and are ignored. Laser heating of the particle bed is of prime importance to the thermal field. A precise calculation of this phenomena would require a ray-tracing algorithm. Although straightforward to implement, such algorithms are computationally expensive and avoided in this work. Instead a uni-directional Beer-Lambert type laser absorption model is used.

Referring to the material field phenomena in Table 2.1, of prime importance is cap-

turing the melting/re-solidification of the powder bed material as well as the thermal dependence of properties. While the microstructural phase and direction has a significant effect on determining property values, such calculations are more suitable to grain growth specific numerical methods and are left out of this model. Ablation and vaporization can be easily simulated by including a damage parameter for the individual SPH particles but are not included in this work.

The following description of the methodology has been subdivided into the three main fields; mechanical, thermal, and material; with an additional section to cover a novel Isothermal incompressible WCSPH formulation. Derivation of the governing mathematical models will be will be presented first followed by SPH discretizations.

3.1 Mechanical Field

3.1.1 Mechanical Mathematical Model

The scope of this research covers free-surface incompressible viscous flow. It is common in numerical simulation literature to define liquid metals as incompressible as their compressibility is an order of magnitude greater then that of water[63]. While liquid metals are generally inviscid, viscous forces can play an important factor in their flow, especially at lower temperatures, where the material thickens, or high velocities. The flow of liquid metals therefore may be modeled by the general Navier-Stokes(NS) equations:

$$\begin{aligned} 0 =& \frac{d\rho}{dt} + \rho \nabla \cdot \boldsymbol{u} \\ \rho \frac{d\boldsymbol{u}}{dt} =& \rho \mathbf{g} - \nabla p \mathbf{I} + \nabla \cdot \left(2\mu\left(T\right)\mathbf{D}\right) + \nabla\left(\lambda\left(\nabla \cdot \boldsymbol{u}\right)\right) + \mathbf{F}_B \\ & \frac{d\boldsymbol{r}}{dt} = \boldsymbol{u} \end{aligned} \tag{3.1}$$

where $\boldsymbol{u}$ is the fluid velocity, $\boldsymbol{r}$ the displacement, ρ the fluid density, μ the fluid shear viscosity (a function of temperature), p the pressure, and λ the bulk viscosity. $\mathbf{D}$ is the rate of deformation tensor, $\mathbf{D} = \left(\nabla \boldsymbol{u} + \nabla \boldsymbol{u}'\right)/2$, and $\mathbf{F}_b$ volumetric external body forces, in this case surface tension, $\boldsymbol{F}_{st}$. The incompressibility constraint is enforced by assuming the fluid to be weakly-compressible. This assumption is generally used in order to avoid the solution of a matrix Poisson equation for the pressure field, which can be computationally expensive and comes with the strict enforcement of incompressibility. Weak-Incompressibility is formulated through the use of a stiff EOS. A typical EOS is

$$p = c_0^2\left(\rho - \rho_0\right) \tag{3.2}$$

where p is the pressure, c_0 the sound speed, and ρ_0 a reference density. The compressible Navier Stoke's equations, 3.1 implemented with Eq 3.2 and discretized with the SPH method are referred to as Weakly Compressible SPH (WCSPH). The standard weakly

compressible EOS assumes the fluid to be baratopic. While this assumption is acceptable for most fluids solved with SPH, it is unsuitable for simulating the SLM process where there is significant thermal expansion of the melt. To model this, a novel isothermally WCSPH that is not baratopic was developed. This will be detailed later in this chapter.

In the weakly compressible regime, the compressible viscosity term is negligible for the flows studied in this work (see e.g. [46] and [13]) and it is not further considered. A benefit of the SPH formulation as opposed to the Finite Volume or Eulerian FEM method is that its Lagrangian in nature eliminating the non-linearity components of the velocity material derivative in Eq. 3.1:

$$\frac{d\left(\cdot\right)}{dt} = \frac{\partial\left(\cdot\right)}{dt}.$$

Under these conditions, and with the additional hypothesis of constant dynamic viscosity, the weakly-compressible Navier Stokes equations to be solved become

$$\begin{aligned} \frac{\partial \rho}{\partial t} + \rho \nabla \cdot \boldsymbol{u} &= 0, \\ \rho \mathbf{g} - \nabla p \boldsymbol{I} + 2\mu \nabla^2 \boldsymbol{u} + \mathbf{F}_{st} &= \rho \frac{\partial \boldsymbol{u}}{\partial t} \\ p = c_0^2 \left(\rho - \rho_0\right), \;\; \boldsymbol{u} &= \frac{\partial \boldsymbol{r}}{\partial t} \end{aligned} \tag{3.3}$$

$$\begin{aligned} \frac{\partial \rho}{\partial t} + \rho \nabla \cdot \boldsymbol{u} &= 0, \\ \rho \mathbf{g} - \nabla p \boldsymbol{I} + 2\mu \nabla^2 \boldsymbol{u} + \mathbf{F}_{st} &= \rho \frac{\partial \boldsymbol{u}}{\partial t} \\ \boldsymbol{u} &= \frac{\partial \boldsymbol{r}}{\partial t} \end{aligned} \tag{3.4}$$

The value of c_0 is chosen such that density variations are minimized[52];

$$100 * \left(\frac{\rho - \rho_0}{\rho_0}\right) < 1\% \tag{3.5}$$

A priori estimates for the sound speed can be made through non-dimensional comparison of the pressure force term with other terms in in the Balance of Linear Momentum(BLM) equation, second line of Eq. 3.3. With a weakly compressible EOS, the pressure term in the BLM, can be approximated as

$$\frac{1}{\rho}\nabla p \approx \frac{c_0^2 \Delta \rho}{\rho}.$$

Equating this to the vicious diffusion term one can derive an estimate for the max sound speed required to balance the viscous forces,

$$\begin{aligned}\frac{1}{\rho}\nabla p \sim & 2\mu\nabla^2\boldsymbol{u} \\ \frac{c_0^2\Delta\rho}{\rho L_)} \sim & 2\mu\frac{U_0}{L_0^2}\end{aligned}$$

solving for c_0,

$$c_0^{visc} \sim \sqrt{\mu\frac{U_0 p}{\Delta\rho L_0}} \tag{3.6}$$

where U_0 the problem velocity scale, and L_0 the problem length scale.
Similar estimates can be made for the advection term:

$$\begin{aligned}\frac{1}{\rho}\nabla p \sim & \frac{\partial\boldsymbol{u}}{\partial t} \\ \frac{c_0^2\Delta\rho}{\rho L} \sim & \frac{U_0}{t} \\ c_0^{adv} \sim & \sqrt{U_0^2\frac{\rho}{\Delta\rho}}\end{aligned} \tag{3.7}$$

and the body force term,

$$c_0^{body} \sim \frac{F\rho}{L\Delta\rho} \tag{3.8}$$

where F is the magnitude of the body force. These equations can be used for initial estimates of the required sound speed and refined upon once simulation data is available.

The deformation of the solid phase is not modeled in this work. Its assumed that the motion of the solid phase is negligible compared to that of the liquid phase and has no effect on the fluid motion. The solution of the mechanical field in the solid phase is only necessary for the calculation of thermal residual stresses and material failure. Although these are important aspects of the SLM process, they are outside the current scope of this work due to the added complexity of implementing a solid framework and the very restrictive time step restrictions imposed by a solid phase simulation([37]). In addition the simulation of solid deformation is more suited to continuum methods such as the Finite Element Method.

Although the rigid body motion of solids is possible within the SPH framework, it is not implemented in the current work, therefore all solid bodies are assumed to act as fixed-rigid bodies. It is desired to simulate their motion in future work to investigate their effect on flaw formation (voids, unmelted particles, ejected particles, etc.)

The continuum surface force (CSF) model proposed by Brackbill [14] is used to model the normal and tangential surface tension forces in the AM-SPH method. The CSF method transforms the surface tension traction into a volumetric force via a delta function that acts in a finite interface region,

$$\boldsymbol{F}_{st} = (\sigma\kappa\hat{\boldsymbol{n}} + \nabla_s\sigma)\,\delta_f, \tag{3.9}$$

where, σ is the surface-tension coefficient, κ the interfacial curvature, $\hat{\boldsymbol{n}}$ the interface unit normal, $\nabla_s(\cdot)$ the tangential surface gradient, and δ_f the interface delta function. It is assumed that the surface tension coefficient is a function solely of temperature. Therefore the second term of Eq. 3.9 can be re-written as

$$\nabla_s\sigma = \frac{d\sigma}{dT}\frac{dT}{ds} \tag{3.10}$$

where $\frac{d\sigma}{dT}$, the surface-tension-temperature coefficient, controls the magnitude of the Marangoni convection. A color function, c_f, is used to track the position of the interface where

$$c_f^{(i)} = \begin{cases} 1 & if\ in\ phase\ i \\ 0 & otherwise. \end{cases} \tag{3.11}$$

The surface normal and curvature can be calculated via the gradient of c_f,

$$\boldsymbol{n} = \frac{\nabla c_f}{[c_f]}, \tag{3.12}$$

$$\kappa = -\nabla\cdot\hat{\boldsymbol{n}}, \tag{3.13}$$

where $[c_f]$ is the jump in the color function across the interface. Finally, while inter-particle surface tension formulations (e.g. Tartakovksy & Meakin [15]) have been implemented within SPH, they are unable to accurately capture Marangoni convection and therefore were not used in this work.

3.1.2 Mechanical SPH Discretization

Navier-Stokes Discretization The well known $\delta - SPH$ scheme proposed by Antuno et al. [4] is adopted in the numerical discretization of the continuity equation in the Weakly Compressible NS equations (Eq. 3.3). The $\delta - SPH$ framework smooths out localized spatial fluctuations in the density/pressure fields that are often apparent in SPH simulations of violent free-surface flows and can lead to inaccurate results. It does so by augmenting the continuity equation with a diffusion term;

$$\left\langle \frac{d\rho}{dt} \right\rangle \approx \frac{d\rho_a}{dt} = \rho \sum_{b=1}^{N_{neigh}} \left(\mathbf{u}_{ab} + \mathbf{F}_{ab}^{diff}\right)\cdot\nabla_a W_{ab} V_b \tag{3.14}$$

where $(\cdot)_a$ is the value at the $a-th$ SPH particle, the summation is performed over N_{neigh} neighboring particles, ∇_a indicates the gradient with respect to the $a-th$ SPH particle, $\mathbf{F}^{diff}$ the is the $\delta - SPH$ diffusion term, and the notation $(\cdot)_{ab} \equiv (\cdot)_a - (\cdot))_b$. Various forms of the density diffusion term have been proposed and formulated. For

example a form proposed by Molteni and Collagrossi [49] and later modified by Antuono et al. [**?**] relies on density differences,

$$\mathbf{F}_{ij}^{An} = -2\delta h c_0 \left(\left(\rho_j - \rho_i\right) \frac{\mathbf{r}_{ij}}{\left|\mathbf{r}_{ij}\right|^2} + f_l\left(\rho_i, \rho_j\right) \right) \tag{3.15}$$

where δ is smoothing parameter and f_l an optional renormalization term. A second form proposed by Fatehi and Manzari[23] as well as Hashemi et al.[23][23] relies on pressure differences between neighboring particles,

$$\mathbf{F}_{ij}^{Ha} = -\frac{-\Delta t \rho_i}{\rho_0} \left(\left(p_j - p_i\right) \frac{r_{ij}}{\left|\mathbf{r}_{ij}\right|^2} \right). \tag{3.16}$$

A description of the various forms of the density diffusion term and their impact on the solution is covered in-depth by Ceros Pita [8]. The form chosen for this methodology will be discussed later in this chapter as it is tied to the novel Isothermal WCSPH formulation devloped in this thesiss. All forms of the diffusion term are designed to be of a higher order then the spatial resolution and disappear under mesh-refinement.

A variety of SPH formulations exists for discretizing the pressure gradient and viscosity terms of the NS equation. For this work, low complexity SPH formulations that are consistent on the free surface or globally convergent were chosen. For the pressure gradient term, a free surface formulation developed by Collagrossi et al. [19] is used,

$$\left\langle \frac{1}{\rho} \nabla p \right\rangle \approx -\sum_b \frac{m_b}{\rho_a \rho_b} \left(\frac{p_b}{\Gamma_a} + \frac{p_a}{\Gamma_b} \right) \nabla_a W_{ab} \tag{3.17}$$

where $\Gamma_a = \sum_b W_{ab} V_b$ is a renormalization factor. Eq. 3.17 is a symmetrized form of the Shepard's Kernel. It is first order consistent as well as conservative on the free surface. The Monaghan and Gingold [50] viscous term formulation, adapted by Marrone et al.[47] for multi-phase fluids, is used in this work;

$$\left\langle \frac{1}{\rho} 2\mu \nabla^2 \boldsymbol{u} \right\rangle \approx \sum_b \left(\frac{\mu_a \mu_b}{\mu_a + \mu_b} \right) \frac{m_b}{\rho_a \rho_b} \pi_{ab} \left(\boldsymbol{u}_b - \boldsymbol{u}_a\right) \cdot \nabla_a W_{ab} \tag{3.18}$$

where,

$$\pi_{ab} = 2\left(DIM + 2\right) \frac{\left(\boldsymbol{u}_b - \boldsymbol{u}_a\right) \cdot \left(\boldsymbol{r}_b - \boldsymbol{r}_a\right)}{\left|\left|\boldsymbol{r}_b - \boldsymbol{r}_a\right|\right|^2}.$$

Eq. 3.18 was found found by Collagrossi et al. to be locally inconsistent on the boundary but globally convergent. Due to its symmetry it exactly conserves momenta and energy[**?**]. Locally consistent formulations of the viscous term were reported by Collagrossi but they require computationally expensive matrix inversions to restore consistency and are only necessary when highly accurate shear formulations are desired.

Boundary Conditions Boundary conditions are implemented via ghost particles. A layer of three ghost particles were placed around the limits of the computational domain. The ghost particles take upon the pressure of the interacting fluid particles to prevent penetration. In addition they reflect the velocity of interacting fluid particles to induce a no slip boundary condition[12].

Solid-Liquid Interaction As mentioned above, solid material is treated as a fixed-rigid body. As such calculation of pressure with the WCSPH EOS is meaningless. In order to prevent flow penetration of the solid particles, the same pressure treatment applied to the ghost particles on the boundary was applied to solid SPH particles interacting with fluid particles. This methods prevent fluid solid particle penetration and separations except under extreme conditions.

Surface Tension Several SPH discretization of the Brackbill CSF method for modeling surface tension (Eqs.3.9-3.13) have been suggested in literature. All however were developed for multi-phase interfaces, and are for the most part free surface incompatible. The first implementation of CSF in SPH was preformed by Morris in 2002[54]. His method succinctly discretizes the CSF method using standard SPH formulations. However, as will be discussed shortly in more detail, his method requires a truncation of erroneous normalized normals that can appear in interior of the interface. Unless cut-off, these normals produce incorrect curvature values when calculated using Eq. 3.13. Adami et al.[2] claim to have developed an improved SPH formulation for the curvature calculation which doesn't require a normal truncation. Their method however is unclear about how they avoid this issue and there are several inconsistencies in the reported results of their paper[2]. Their method has been successfully implemented in following works([66]and [35, 36]) however its unclear to this author how. For these reasons, the Morris implementation, with modifications to allow it to be used on a free surface, was implemented in the AM-SPH methodology.

The standard Morris method is as follows:

1. Smooth the color function, to allow for a more accurate calculation of normals:

$$c_a = \sum \frac{m_b}{\rho_b} c_b W_{ab} \tag{3.19}$$

2. Calculate the normals as the gradient of the color function:

$$\mathbf{n} = \nabla c = \sum V_b c_{ba} \nabla W_{ab} \tag{3.20}$$

3. Truncate normal if not within a cutoff value to avoid the use of erroneous interior normals in the curvature calculation:

$$\hat{\boldsymbol{n}}_a = \begin{cases} \frac{\boldsymbol{n}_a}{|\boldsymbol{n}_a|} & \frac{\boldsymbol{n}_a}{|\boldsymbol{n}_a|} > 0.1 h_{sml} \\ 0 & otherwise \end{cases} \tag{3.21}$$

4. Calculate a new re-normalization factor, Γ_a^* using only particles with non-zero $\hat{\boldsymbol{n}}_a$:

$$\Gamma_a^* = \sum_b \frac{m_b}{\rho_b} W_{ab} \cdot ceil(\hat{\boldsymbol{n}}_a) \tag{3.22}$$

5. Calculate the curvature using a re-normalized, consistent formulation:

$$\langle \nabla \cdot \hat{\boldsymbol{n}}_a \rangle = \frac{1}{\Gamma_a^*} \sum V_b \hat{n}_{ba} \cdot \nabla W_{ab} \tag{3.23}$$

6. Calculate the normal surface tension force:

$$f_s = -\sigma_b \left(\nabla \cdot \hat{\mathbf{n}}\right)_a \mathbf{n}_a \tag{3.24}$$

Three flaws were found in this method and corrected:

1. The smoothing of the color functions assumes the existence of a second phase, if this is not the case, for example on a free surface, the smoothing function only serves to reduce the color function value towards the boundary and give erroneously depreciated values of $\boldsymbol{n}$ and hence lower values of surface tension. The smoothing of the color function is not preformed in this methodology. This was found to have a minimal effect on the correct calculation of the normals.

2. The SPH operator used to calculate the normal, ∇c, is inconsistent on the free surface. Following the work of Collagrossi [11] for a consistent form of the pressure gradient on the free surface, a free-surface compatible SPH discretization for ∇c was used in this work:

$$\langle \nabla c \rangle = \sum \frac{m_b}{\rho_b} \left(\frac{c_b}{\Gamma_a} + \frac{c_a}{\Gamma_b} \right) \nabla W_{ab} \tag{3.25}$$

3. The original Morris method was found to become unstable under deformation. Interior normalized interface normals at the edge of the cutoff values were found to switch on or off triggering unsmooth increases in the curvature of the region and hence jumps in the surface tension force This was noted to destabilize the system in several simulations. To prevent this, a free-surface consistent smoothing of the curvature is preformed to smooth the curvature into bordering regions on the edge of triggering and prevent jumps in the surface tension.

4. There was no means to prevent the calculation of erroneously high curvatures. For example if a small region of particles(2-3 particles in diameter) protrudes off the interface surface, extremely high levels of curvature can be estimated even though this region is finer then what should be resolved by the mesh. It is reasoned the maximum predictable curvature should be on the order of the radius of the smoothing region. For the Wendland Kernel used in this work, that radius is $2h_{sml}$. Therefore the maximum curvature should be: $\kappa_{max} = \frac{1}{2h_{sml}}$.

Therefore the final proposed modified SPH-CSF methodology is:

1. Calculate the normals as the gradient of the color function:

$$\mathbf{n}_a = \langle \nabla c \rangle_a = \sum \frac{m_b}{\rho_b} \left(\frac{c_b}{\Gamma_a} + \frac{c_a}{\Gamma_b} \right) \nabla W_{ab} \tag{3.26}$$

2. Truncate the normal if not within a cutoff value to avoid the use of erroneous interior normals in the curvature calculation:

$$\hat{\boldsymbol{n}}_a = \begin{cases} \frac{\boldsymbol{n}_a}{|\boldsymbol{n}_a|} & \frac{\boldsymbol{n}_a}{|\boldsymbol{n}_a|} > 0.1 h_{sml} \\ 0 & otherwise \end{cases} \tag{3.27}$$

3. Calculate the new normalization, value Γ_a^* using only particles with non-zero $\hat{\boldsymbol{n}}_a$:

$$\Gamma_a^* = \sum_b \frac{m_b}{\rho_b} W_{ab} \cdot ceil(\hat{\boldsymbol{n}}_a) \tag{3.28}$$

4. Calculate the curvature using a re-normalized, consistent formulation:

$$\langle \kappa_a \rangle = \langle \nabla \cdot \hat{\boldsymbol{n}}_a \rangle = \frac{1}{\Gamma_a^*} \sum V_b \hat{n}_{ba} \cdot \nabla W_{ab} \tag{3.29}$$

5. Ceiling curvature values that are higher then the method-discretization resolution:

$$\kappa_a = min\left(\kappa_{max}, \kappa_a\right) \quad ; \quad \kappa_{max} = \frac{1}{2h_{sml}}$$

6. Smooth the curvature:

$$\kappa_a = \frac{1}{\Gamma_a^*} \sum \frac{m_b}{\rho_b} \kappa_b W_{ab} \tag{3.30}$$

7. Calculate the normal surface tension force:

$$f_s = -\sigma_b\left(\kappa_a\right) \mathbf{n}_a \tag{3.31}$$

Simple validations of the modified CSF methodology were preformed by ensuring the correct pressure was calculated inside a droplet of fluid using the Young-Laplace Equation (Section 4.2). It was found that using a smoothing radius of 1.5 times larger then the standard smoothing radius, $h_{sml} = 1.5 * h_{sml0}$, is necessary to accurately calculate the curvature and hence the surface tension for the droplet. This significantly increases the computational cost of calculating the surface tension.

The Marangoni convection component was calculated using the formulation from Tong and Browne[66];

$$\nabla_s \sigma = \nabla\sigma - (\nabla\sigma \cdot \hat{n})\,\hat{n} \tag{3.32}$$

and if σ varies linearly with temperature, this becomes,

$$\mathbf{F}_{st}^{Marangoni} = \left.\frac{d\sigma}{dT}\right|_T \left(\nabla T - \left(\nabla T \cdot \frac{\nabla c}{|\nabla c|}\right)\frac{\nabla c}{|\nabla c|}\right)|\langle \nabla c \rangle_a|\,. \tag{3.33}$$

where the notation $|\cdot|$ indicates vector magnitude. Tong and Browne found this formulation to be accurate for two-phase boundaries however the formulation for ∇T was not free-surface compatible. The free surface, first order consistent Shepard Kernel was used in this work,

$$\langle \nabla T \rangle_S = -\frac{1}{\Gamma_A}\sum_b \frac{m_a}{\rho_a} T_A W_{ab}. \tag{3.34}$$

$$\mathbf{F}_{st}^{Marangoni} = \left.\frac{d\sigma}{dT}\right|_{T,a} \left(\langle \nabla T \rangle_a - (\langle \nabla T \rangle_a \cdot \hat{\mathbf{n}}_a)\,\hat{\mathbf{n}}_a\right)|\nabla c|\,. \tag{3.35}$$

Surface tension forces were solved throughout the domain and solid and fluid particles were considered to be of the same color function.

3.2 Thermal Field

3.2.1 Thermal Mathematical Model

The thermal field is governed by the local form of the internal energy balance equation (First Law of Thermodynamics), which equates the rate of internal energy change of the body, $\rho\dot{\varepsilon}$, to the applied external thermal power, $\mathcal{W}$, and mechanical power, $\mathcal{P}$;

$$\rho\dot{\varepsilon} = \mathcal{P} + \mathcal{W} \tag{3.36}$$

As the fluid is incompressible, the internal energy is assumed to be solely a linear function of temperature, $\rho\dot{\varepsilon} = \rho c\dot{T}$, where c is the specific heat capacity of the material. The mechanical power is given by the inner product of the stress and the velocity gradient, where for incompressible materials the spherical component of the stress power is zero, leaving only a viscous heating term. While liquid metals are considered inviscid, this term is still relevant due to the high velocity gradients that can occur in the SLM process:

$$\mathcal{P} = \boldsymbol{\sigma} : \nabla \boldsymbol{u} = \boldsymbol{\tau} : \nabla \boldsymbol{u} \tag{3.37}$$

The thermal power contribution is composed of a conductive term and volumetric source terms for the laser heating (s_{laser}), and radiation effects (s_{rad}):

$$\mathcal{W} = \mathcal{Q} + \mathcal{H} = \nabla\left(k \cdot \nabla T\right) + s_{laser} + s_{rad}, \tag{3.38}$$

where k is the isotropic thermal conductivity. Radiation, normally a surface boundary condition, is approximated as a volumetric source term to allow its implementation with the SPH method. The standard Stefan-Boltzmann law is given as:

$$s_{rad} = \sigma_B \varepsilon (T^4 - T_\infty^4)/\Delta z. \tag{3.39}$$

where σ_B is the Boltzmann Constant, ε the emissivity, T_∞ the background temperature(assumed to be $T_\infty = 293K$), and Δz the nodal spacing.

A Beer-Lambert laser absorption scheme is used to model the laser penetration into the body, where the laser intensity at some depth, z , positive into the body, is

$$I\left(z, r\right) = I_0\left(r\right) e^{-\int_0^z \alpha(z) dz} \tag{3.40}$$

where $I_0\left(r\right)$ is the initial intensity at the surface of the body and α the absorption coefficient. The power absorbed by a volume of the body, V, can be calculated as $P_{abs} = \alpha I V$. Therefore we can define the volumetric laser source term as

$$s_{laser} = \alpha I\left(r, z\right). \tag{3.41}$$

The laser beam is modeled with a Gaussian profile, where P_{laser} is the total laser power and r_l is the 2σ spot radius of the laser. The intensity as a function of radial distance from the laser center is therefore:

$$I_0\left(r\right) = \frac{2P_{laser}}{\pi r_l^2} e^{\left(-\frac{2r^2}{r_l^2}\right)}. \tag{3.42}$$

More complex options exists for modeling the laser penetration into the body including ray-tracing schemes. These schemes track individual rays of the laser as they move into the body, are absorbed/reflected, and emitted. While ray-tracing schemes model laser penetration with high fidelity they are significantly more computationally intensive then the Beer-Lambert scheme. In addition, the values of coefficients for absorption, reflection, and emission of metallic materials at high temperatures are hard to experimentally measure and are not well known. With such high-levels of uncertainty the use of a ray-tracing scheme would not even garantee correct modeling of the actual phenomena. For this work, a homogenized absorption coefficient that encompasses all these phenomena was considered accurate enough. For the particle bed, phenomenological and closed form analytical models for laser absorption have also been suggested and could be applied if applicable[30].

The final thermal PDE to be solved is :

$$\rho c \dot{T} = \boldsymbol{\tau} : \nabla \boldsymbol{u} + \nabla \left(k \cdot \nabla T\right) + s_{laser} + s_{rad}. \tag{3.43}$$

3.2.2 Thermal SPH Discretization

SPH formulations for the first two terms of the thermal equation, Eq. 3.43, have been proposed in previous works. An SPH formulation for the viscous heating of a multiphase material with varying conductivity was given by Marrone et al. [46],

$$\frac{1}{\rho}\boldsymbol{\tau}\colon\nabla\mathbf{v} = \sum\left(\frac{\mu_i\mu_j}{\mu_i+\mu_j}\right)\frac{m_i}{\rho_i\rho_j}\pi_{ij}\left(\mathbf{v}_j-\mathbf{v}_i\right)\cdot\nabla_i W_j \tag{3.44}$$

with,

$$\pi_{ij} = 2\left(n_{dim}+2\right)\frac{\left(\mathbf{v}_j-\mathbf{v}_i\right)\cdot\left(\mathbf{r}_j-\mathbf{r}_i\right)}{\left\|\mathbf{r}_j-\mathbf{r}_i\right\|^2}.$$

This formulation while not first order consistent on the free-surface is conservative guaranteeing global convergence[46].

Cleary and Monaghan [9] give a SPH formulation for thermal conduction in a multiphase material,

$$\frac{1}{\rho}\nabla\cdot\left(k\nabla T\right) = \sum_b \frac{4m_b}{\rho_a\rho_b}\frac{k_a k_b}{\left(k_a+k_b\right)}\left(T_{ab}\right)\frac{\mathbf{r}_{ab}\nabla W}{\mathbf{r}_{ab}\cdot\mathbf{r}_{ab}+\eta^2}. \tag{3.45}$$

It is unknown how accurate or conservative this formulation is on the free surface. The development of a free-surface compatible SPH discretization of the temperature Laplacian will be a goal of future works.

A novel scheme for applying the Beer-Lambert model for laser penetration to an SPH framework was developed in this work. The scheme uses a binning algorithm to partition the particle masses onto a grid framework that can be efficiently navigated. A 2-D version of the algorithm is as follows:

1. Overlay a grid onto the laser affected regions of the SPH domain.

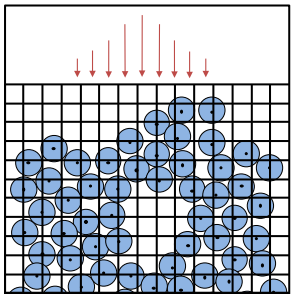

Figure 3.1

2. Loop over all effected SPH particles and calculate the weight fraction of the particle in each neighboring bin, w_p^{bin}, using a Particle-In-Cell weighting scheme, where (P_x, P_y) is the SPH particle center and (C_x, C_y)t he nearest bin grid point;

$$w_p^{bin} = (1 - |C_x - P_x|)\,(1 - |C_y - P_y|)$$

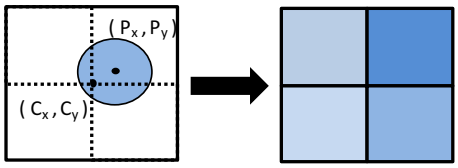

Figure 3.2

3. Sum all particle contributions to a given bin to calculate the total volume/weight fraction of particles in the bin:

$$w_{total}^{bin} = \sum_p w_p^{bin}$$

$$V_f^{bin} = \frac{\sum_p w_p^{bin} V_p}{V_{tot}^{bin}}$$

4. Loop over columns of bins, from top down, applying a discretized Beer-Lambert Scheme to calculate the laser power absorbed by a bin, where $\Delta z_i^{bin}$is the height of the ith bin and the volume fraction of the bin, is used to scale the thickness of the bin.

$$I\,(z_{col}) = I_0 e^{-\sum_i a_i \Delta z_i^{bin} V_{f,bin}}$$

$$P_{bin} = \alpha I\,(z_{bin}) \sum_p w_p^{bin} V_p$$

5. Transfer the power absorbed by a bin to its constituents particles in a weighted fashion:

$$P_p = \sum_{bins} P_{bin} \frac{w_p^{bin}}{\sum_p w_{bin}^p}$$

6. Calculate the volumetric power contribution to a particle.

$$s_{laser,p} = \frac{P_p}{V_p}$$

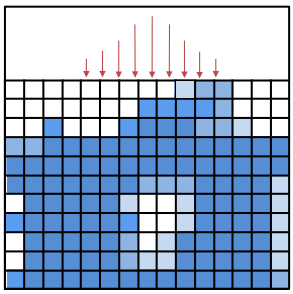

Figure 3.3

3.3 Material Field

The material field is dominated by the thermal-and-state variance of material properties. The Apparent Heat Capacity method, developed by Hashemi & Sliepcevich [31] , was implemented to model the significant latent-heat release and absorbtion during the melting and re-solidification processes respectively. The method accounts for this energy via a modification of the heat capacity during a phase change using the latent heat of melting, L,

$$c = \begin{cases} c_S & T < T_M - \frac{\delta T}{2} \\ \frac{c_s + c_L}{2} + \frac{L}{2\Delta T} & T_m - \frac{\delta T}{2} \leq T \leq T_m + \frac{\delta T}{2} \\ c_L & T_m + \frac{\delta T}{2} < T \end{cases} \tag{3.46}$$

where δT is the phase change temperature bandwidth and T_m the melting temperature. This method can be interpreted as introducing a barrier to the melting process requiring extra heat input to pass through the bandwidth region. The material state is determined by:

$$s = \begin{cases} 0 & T < T_M - \frac{\delta T}{2} \\ \frac{\left(T - \left(T_m - \frac{\delta T}{2}\right)\right)}{\delta T} & T_m - \frac{\delta T}{2} \leq T \leq T_m + \frac{\delta T}{2} \\ 1 & T_m + \frac{\delta T}{2} < T \end{cases} \tag{3.47}$$

where $s = 0$ indicates a liquid state, $s = 1$ a solid state, and $0 < s < 1$ the fraction of transition between a solid and liquid phase. As a section of material undergoes a phase change, its material properties are linearly varied from those of one state to the other. During the transition from solid to liquid phases the viscosity is lowered from a high viscosity to that of the fluid to simulate the mushy zone mechanics.

The Apparent Heat Capacity method can be trivially applied implemented in an SPH formulation on a SPH particle-SPH particle basis.

3.4 Novel Isothermal Incompressible WCSPH Formulation

In 3D printing type Additive Manufacturing process where rapid heating and cooling are ubiquitous(e.g. in the SLM of stainless steels density changes can be on the order of 25%, in a millisecond), the thermal expansion of the fluid can have a significant impact on material motion and therefore a general SPH framework for modeling it would be highly desired. While not necessary for the given process, modeling buoyancy forces accurately can be important for simulating other manufacturing processes and would be desired, albeit not necessary. In addition material flows in AM processes can often be violent and involve free surfaces, adding more difficulty to the model. Any method proposed must be cable of handling these two conditions. A modification to the $\delta - SPH$ framework, which is the state of the art for stable simulation of volatile-free surface flows, to implement these phenomena is proposed and investigated.

3.4.1 Theory

In order to begin an investigation of the simulation of these phenomena a basic understanding of the volumetric expansion of an incompressible flow and the resulting buoyancy driven effects is needed.

3.4.1.1 Isothermal-incompressibility

It is common in numerical simulation literature to define liquid metals as incompressible as their compressibility is an order of magnitude greater then that of water[63]. The definition of an incompressible material is one in which the Jacobian of the deformation gradient is 1, or in other words, $dv = dV$ for all motions. However liquid metals experience significant thermal expansion/contractions when undergoing heating/cooling. A plot of the density of stainless steel as a function of temperature is given in Figure 3.4. The density changes over 25% from the onset of the fluid state to the vaporization point. Therefore more care should be taken in describing liquid metals as in general incompressible. Instead they shcold be described as incompressible under isothermal conditions; i.e. incompressible only at a fixed temperature.

For isothermally incompressible fluids the common measure of incompressibility, $div\,(\mathbf{u}) = 0$, does not hold, instead a new measure needs to be derived. Continuity of mass for a Lagrangian discretization is given as

$$\frac{\partial \rho}{\partial t} = \rho div\,(\mathbf{u})$$

If it assumed that the density varies linearly with temperature via a volumetric expansion coefficient, α_V, then we can write the partial time derivative of the density as,

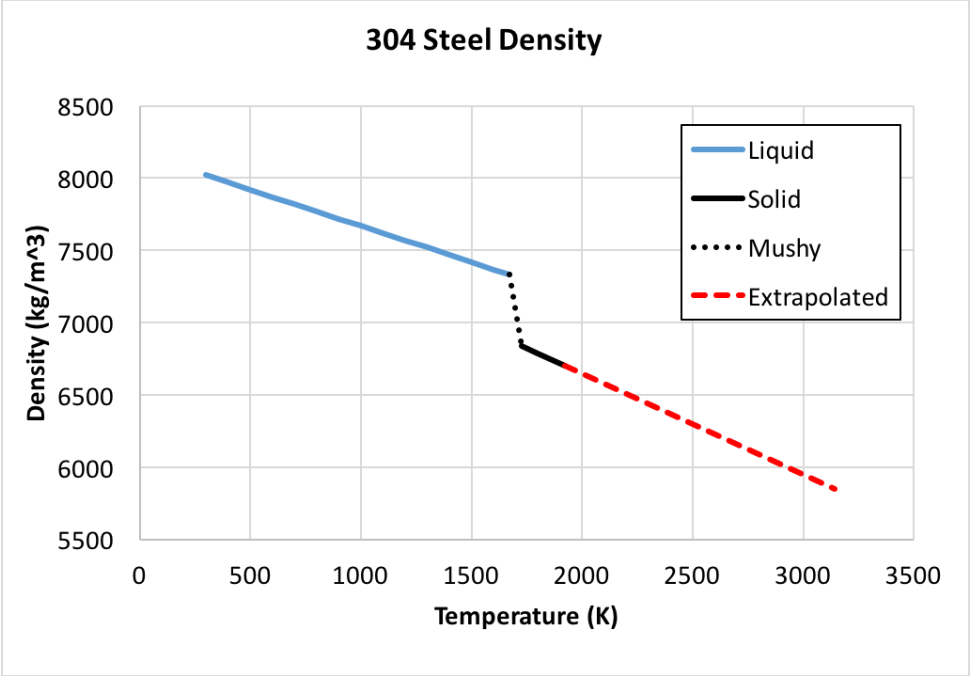

3.48

Figure 3.4: 304 steel density as a function of density for the solid and liquid phases. Data taken from Mills [48] (solid phase) , Dubberstein et al. [20](liquid phase), and extrapolated to the vaporization point.

$$\frac{\partial \rho}{\partial t} = \alpha_V \frac{\partial T}{\partial t}. \tag{3.48}$$

Inserting this into the material time derivative we can derive an equation for $div\,(\mathbf{u})$ for an isothermally incompressible fluid;

$$div\,(\mathbf{u})|_T = \frac{\alpha_V}{\rho(T)} \frac{\partial T}{\partial t}\bigg|_T. \tag{3.49}$$

This relation will be useful in confirming the ability of the proposed formulation to accurately enforce the isothermal incompressibility constraint.

3.4.1.2 Buoyancy

When density gradients exist in a fluid, buoyancy driven motion can occur. Buoyancy flows are commonly split into Boussinesq and Non-boussinesq flows. Boussinesq flows are one in which density changes have no effect on the flow fluid other then to give rise to buoyancy forces and are valid for $\Delta\rho(T) \ll \rho_0$. In these flows the buoyancy force can be explicitly included in the balance of linear momentum as $F_B = (\rho - \rho_0)\,\mathbf{g}$.

However for our problem $\Delta\rho \ll \rho_0$ is not satisfied and a Non-boussinesq flow is needed. In this model the buoyancy forces come into the balance of linear momentum through

the gradient of pressure via uneven hydrostatic pressure fields resulting from varying fluid densities. The correct implementation of this methodology therefore requires the correct calculation of the hydrostatic pressure fields. Ensuring this is the case in a weakly compressible SPH formulation in which the pressure fields are also used to maintain incompressibility will be difficult.

3.4.2 Isothermal WCSPH Methodology

3.4.2.1 Previous Related Works

To this author's knowledge no previous work has been undertaken to develop an SPH scheme cable of simulating volume expansion of incompressible fluids. A novel methodology will be presented and qualified in this work.

A few investigations have been preformed to model buoyancy forces with SPH in both Boussinesq [43, 67] and Non-Boussinesq flows [65, 28]. While these schemes produce accurate results they are not suitable for simulating AM processes. They were either developed for multiphase flows with distinct phases(i.e. not density gradients), use a summation methodology for the density(undesirable when simulating free surface flows), or if they were developed for single phase flow (with density gradients) require the use of a background mesh (undesirable for a mesh-free method such as SPH and difficult to implement for a free surface problem). Only one of these schemes , Szewc et al. [65] couples the density of the fluid to its temperature.

The goal of this work is to develop a method capable of simply and efficiently simulating the expansion/contraction of a volatile, free-surface isothermally incompressible fluid with varying density. In addition the correct evaluation of buoyancy effects is desirable. To do so I propose using a modified WCSPH equation of state in conjunction with a specific form the of the $\delta - SPH$ framework.

3.4.2.2 Isothermal-WCSPH Modified EOS

I propose a simple modification to the traditional WCSPH EOS to allow for thermal (or concentration) induced density changes while maintaining fluid incompressibility. Most WCSPSH EOS are either functions of density;

$$p = \hat{f}\left(\left(\rho - \rho_0\right)^{\gamma}, c\right) \tag{3.50}$$

or the spatial distribution of particles

$$p = \hat{f}\left(\left(\Omega - \Omega_0\right)^{\gamma}, c\right) \tag{3.51}$$

where ρ is the fluid density, ρ_0 the reference density, γ some constant, c the fluid sound speed, Ω the particle volume, and Ω_0 the reference particle volume. The difference of the fluid density from its reference value (or particle volume from its reference volume)

creates a restoring pressure field that maintains incompressibility and ensures that $\rho \approx \rho_0$ or $(\Omega = \Omega_0)$.

In most thermal-material numerical schemes the density field is directly coupled to the thermal field, i.e. $\rho = \hat{\rho}(T)$. Szewc et al. [65] proposed a WCSPH framework of this form where they compute the density of the fluid via a summation particle density scheme and then correct it for the thermal expansion of the material

$$\rho^{cor} = \rho(1 - \beta\delta T).$$

The EOS is a function of the particle volume and ensures constant SPH particle volume (general incompressability)

$$p = \frac{c_0^2 \rho_0}{\gamma}\left(\left(\frac{\Omega_0}{\Omega}\right)^{\gamma} - 1\right)$$

This numerical scheme however is undesirable for the simulation of AM processes. First, it is incompatible with free surface flows due to the use of a summation particle density scheme which suffers on the boundaries. In addition this scheme is incapable of inducing particle expansion as the EOS is a function only of particle spacing, not density, keeping the particle volumes constant. Finally the method is incompatible with the $\delta - SPH$ framework, due to the use of the summation density scheme, and thus could potentially suffer from localized pressure fluctuations.

Therefore, instead of modifying the density directly as Szewc et al. does, I propose instead to directly couple the reference density, as opposed to the density, to the temperature field; $\rho_0 = \hat{\rho_0}(T)$, and use the EOS to drive the density of the fluid to its thermal equilibrium state. The EOS for pressure therefore becomes;

$$p = c_0^2(\rho - \rho_0(T))$$

where

$$\rho_0 = \rho_{ref} - \alpha_T(T - T_{ref}) \tag{3.52}$$

The fluid density is then calculated using the mass continuity equation, a free surface compatible method, with the $\delta - SPH$ smoothing scheme, Eq. 3.14.

There are many benefits of the proposed scheme. First it is a more natural means for implementing the incompressibility constraint then correcting the calculated density field thermal variations as suggested by Szewc et al. The density calculated via the EOS and continuity equation is the correct density for the fluid and doesn't require post-processing. It can also be easily implemented within existing WCSPH frameworks with little work. Secondly, it allows for the volumetric expansion/contractions of the SPH particles and hence is able to create volumetric expansion/contraction driven fluid motion. Finally, it is viable for simulating violent free surface flows as it uses a continuity formulation to calculate the density and can be implemented within a $\delta - SPH$ framework. The $\delta - SPH$

framework smooths out oscillations in the density/pressure fields that are often apparent in these types of flows and can lead to inaccurate results. Unlike the previously mentioned schemes, it is therefore capable of accurately simulating the SLM additive manufacturing process.

Care is needed when selecting a form for the density diffusion term within the $\delta - SPH$ framework that is compatible with the simulation of density varying flows. Diffusion terms that are functions of density differences between neighboring particles, such as the Antuono scheme Eq. 3.15, can lead to a failure of the proposed methodology. Take for example the case of a high density fluid resting alongside a low density fluid. The $\delta - SPH$ scheme of Antuono is meant to smooth out fluctuations in the density field but in this case will lead to large density diffusion between the two fluids, lowering the density of the heavier fluid and raising the density of the lighter fluid. However the, reference densities of the values will remain the same resulting in large pressure values being calculated via the weakly compressible EOS. If one however uses a pressure based formulation, such as the Hashemi formulation Eq. 3.16, or a formula involving the difference of the density from its reference, $\rho - \rho_0$, the diffusion term will remain of an appropriate size resulting in a smoothing of the pressure field. A modification of the Antuono equation renders it compatible with the proposed methodology:

$$\mathbf{F}_{ij}^{Ma} = -2\delta h c_s \left(\left(\bar{\rho}_j - \bar{\rho}_i \right) \frac{\mathbf{r}_{ij}}{\left| \mathbf{r}_{ij} \right|^2} + f_l \left(\bar{\rho}_i, \bar{\rho}_j \right) \right) \tag{3.53}$$

where,

$$\bar{\rho}_i = \rho_i - \rho_{0i}$$

This was the chosen $\delta - SPH$ formulation used in this work. To account for large particle volume changes, the smoothing radius of the particles must also be altered to ensure full support is maintained. The updated smoothing length value can be calculated as

$$h_{sml} = h_{sml,0} \left(\frac{V}{V_0} \right)^{\frac{1}{DIM}} . \tag{3.54}$$

.In addition particle remeshing schemes can be used as well to ensure a regular distribution of SPH particles is maintained.

3.5 Numerical Methods

Time Integration Schemes A second order explicit leap-frog time integration scheme is used to solve the Navier Stokes equations. The method is conservative, in contrast to the RK4 method,and is therefore preferred for its stability. A separated form of the leap-frog scheme which allows for time step adaptation is used:

$$\begin{aligned} \boldsymbol{a}^t =& F\left(\boldsymbol{u}^t, \boldsymbol{x}^t\right) \\ \boldsymbol{u}^{t+\frac{1}{2}} =& \boldsymbol{u}^{t-\frac{1}{2}} + \Delta t \cdot \boldsymbol{a}^t \\ \boldsymbol{x}^{t+1} =& \boldsymbol{x}^t + \Delta t \cdot \boldsymbol{u}^{t+\frac{1}{2}} \\ \boldsymbol{u}^{t+1} =& \boldsymbol{u}^{t+\frac{1}{2}} + \frac{1}{2}\Delta t \cdot \boldsymbol{a}^t \end{aligned} \tag{3.55}$$

The thermal field PDE (Eq. 3.43) is solved using an fixed-point iterative solving of the implicit, midpoint scheme. The iterative solve allows for matrix free operations which are trivially parallelizable. This is a key necessity when working with low order particle methods. The scheme is as follows:

Algorithm 3.1 Fixed-Point Iterator Scheme

1: **while** $\left(\frac{\left(T(t+\Delta t)^{i+1} - T(t+\Delta t)^i\right)}{T(t)}\right) > tol$ **do**
2: $\quad T\left(t+\Delta t\right)^{i+1} = T(t) + \frac{\Delta t}{2}\left[\mathcal{G}\left(T\left(t+\Delta t\right)^i, t+\Delta t\right) + \mathcal{G}\left(T\left(t\right), t\right)\right]$
3: $\quad \mathcal{G}\left(T\left(t+\Delta t\right)^{i+1}, t+\Delta t\right) = \left[\frac{1}{\rho c}\left(\boldsymbol{\tau} : \nabla \boldsymbol{u} + \nabla\left(k \cdot \nabla T\right) + s_{laser} + s_{rad}.\right)\right]_{t+\Delta t}$
4: $\quad i = i + 1$
5: **end while**

This integration scheme for the thermal differential equation is used for convenience but is not ideal, as it doesn't garantee convergence and is only a fixed point iterator. As such it will be updated in future works.

Time Step Constraints The simulation time step size can be determined by the advective/diffusive CFL conditions. The standard advective CFL condition suggested by Monaghan et al. [51]for the leap-frog time integration scheme is used in this work:

$$\delta t_C \leq C_f \frac{h}{c_s} \; ; \; 0.05 < C_f < 0.5 \tag{3.56}$$

where c_s is the sound speed of the fluid and C_f the CFL factor. The condition ensures the numerical domain of dependence remains within the physical domain of dependence and the simulation remains stable. Additional constraints can be imposed by the physics of the problem. For stability of the viscous diffusion term, Morris et al. [55]suggests using the constraint from Finite Difference methods:

$$\delta t_{visc} \leq 0.125 \frac{h^2}{\nu} \tag{3.57}$$

where $\nu$is the kinematic viscosity.

For the surface tension force, Brackbill [6]suggests a time step constraint formulated using the estimated max capillary wave speed:

$$\Delta t_{surf} \leq 0.25 min(\frac{\rho_{min} h^3}{2\pi\sigma})^2 \tag{3.58}$$

Additionally, body force time step constraints can be imposed by estimating the max velocity from a body force as the acceleration from the body force multiplied by time length obtained from the CFL condition,

$$u_{max} = a_b \cdot \Delta t \approx a_b \cdot C_f \frac{h}{c_s}.$$

This velocity can be reapplied to the CFL condition resulting in body force time step restriction of,

$$\Delta t_{body} \leq \frac{c_S}{a_b}. \tag{3.59}$$

Finally a time step constraint on the the thermal field is imposed by the thermal diffusion CFL condition:

$$\Delta t_{tdiff} \leq 0.125 * \frac{\rho c h^2}{k} \tag{3.60}$$

The minimum of the above time steps is used in the simulation,

$$\Delta t = min\left(\Delta t_C, \Delta t_{visc}, \Delta t_{surf}, \Delta t_{body}, \Delta t_{tdiff}\right) \tag{3.61}$$

The velocity CFL is usually the most restrictive in SPH schemes, with the surface tension a close second. To improve the simulation times, it is desirable to implement an adaptive time stepping scheme were the sound speed of the fluid, a function of the and fluid velocity, is adjusted based off the measured max velocity in the simulation at a previous time step. In this way, when a system is moving slowly, a less restrictive time step can be used while still meeting the CFL condition. Obviously the time step would still need to meet the requirements of Eq. 3.61. Finally, it should be noted that no CFL condition imposed by Marangoni convection was found in literature. As will be discussed later, it is hypothesized that this condition could be more restrictive then the advection CFL condtion and should be derived and used in future works.

Neighbor Searches Core to the SPH method is the detection of neighboring particles. Unlike with meshed methods, meshless methods must preform these connectivity searches repeatedly throughout the course of the simulation. As such, its highly desirable to implement an efficient search algorithm. In this work an $\mathcal{O}(N)$ binning algorithm [56] is used in conjunction with a verlet list update scheme. A description of the binning algorithm can bound in appendix A.

Code Structure A schematic of the code structure for implementing the AM-SPH method is shown in Figure A.1 in Appendix A. The mechanical and thermal fields are solved separately to modularize the code. The method was implemented in C++ in an object-oriented manner. This was chosen to allow for easy code development however the use of classes prevents easily parallelization of the code and should be avoided once experimental work needs to be preformed.

Chapter 4

Model Verification and Validation

4.1 Fundamental SPH Formulations Validation

Validation of the fundamental SPH formulations given above (heat conduction, fluid flow phase change, etc.) was preformed. This was necessary both to ensure the correct implementation of the methodologies but also to ascertain the effect of the free surface on the formulations.

Thermal validation was preformed for various fundamental heat flow problems (2D heat conduction on a square domain with varying material properties and boundary conditions as well as Poisuelle and Couette flows) following the work of Cleary & Monaghan [9]. It was found that the methodology while valid for closed domain problems, suffered near the interface for free surface problems. Free surface compatible formulations of the heat conduction Laplacian will be needed in future works. One means of doing so could be using MLS formulations of the smoothing function and its derivatives near the free surface [18, 19].

Validity of the application of the Apparent Heat Capacity method to SPH was confirmed using the classical 1-D Stefan problem for solidification of single phase fluid as described by Davis [15]. The method was found to be sufficiently accurate.

4.2 Verification of Free Surface Adaptation of Morris SPH-CSF Formulation

As covered in Section 3.1.2, an adaptation of the Morris SPH-CSF methodology for simulating surface tension on a free surface was used in this work. As all the validation studies preformed by Morris [54] were for cases involving surface tension on an interface between two-phases, and not a free surface, the method had to be re-validated. A simple method for validating surface tension is to simulate a 2D circle of fluid only under surface tension forces and confirming the correct pressure value predicted by Young-Laplace's equation, which relates the pressure in a fluid bubble to the surface tension on its boundary, is measured. For a 2D circle of fluid with a free surface, Laplace's equation gives:

$$p = \frac{\sigma}{2R} \tag{4.1}$$

A circle of fluid, $R = 1$, under no-external forces other then surface tension, with $\sigma = 10$, was simulated and the pressure value in the interior measured after a period of time. The mesh resolution was $dx = 0.05$. The measured EOS pressure as a function of radial distance is plotted in Figure 4.1. Young-Laplace's equation predicts a pressure value of $p_{r=1} = 5$. The measured value, $p_{meas} = 6$, is higher then the predicted value. The pressure values are scattered along the interface region as particle movement in this region, due to the vibration of the interface, requires fluctuating EOS pressures to ensure incompressibility is maintained. The higher then expected interior EOS pressure value results form a discrepancy in the ideal radius of curvature of the problem and the actual radius of

curvature in the numerical model. The ideal radius of curvature, $R = 1$, assumed the interface to have infinitesimal thickness. Because the CSF formulation transforms the surface tension traction into a volumetric force, the numerical interface region has finite thickness. As seen in Figure 4.2, which shows the surface tension acceleration, the interface region has about a 2 particle thickness meaning the numerical radius of curvature is closer to $r = 0.9$ which results in a predicted pressure of $p_{r=0.9} = 0.55$, closer to the measured value. While not perfect, it is believed that the method is sufficient enough.

From this validation study, it was also found that a smoothing radius of $h_{sml} \approx 1.8{*}dx$, where $h_0 = 1.2 * dx$ is the standard smoothing radius, was necessary to obtain stable surface tension forces for a two-phase fluid. Morris used as smoothing length value of $h_{sml} = 1.5 * dx$ in their work. It was found that this value was insufficient and would to lead to the calculation of erroneously high surface tension forces resulting in a break-up of the fluid. Unfortunately, the need for such a large smoothing length, $h_{sml} = 1.8 * dx$, leads to increased neighbor pairings growing the computational burden of the CSF-SPH scheme. The development of a more accurate and efficient free surface, SPH formulation for surface tension would be highly desirable but is outside of the scope of this work.

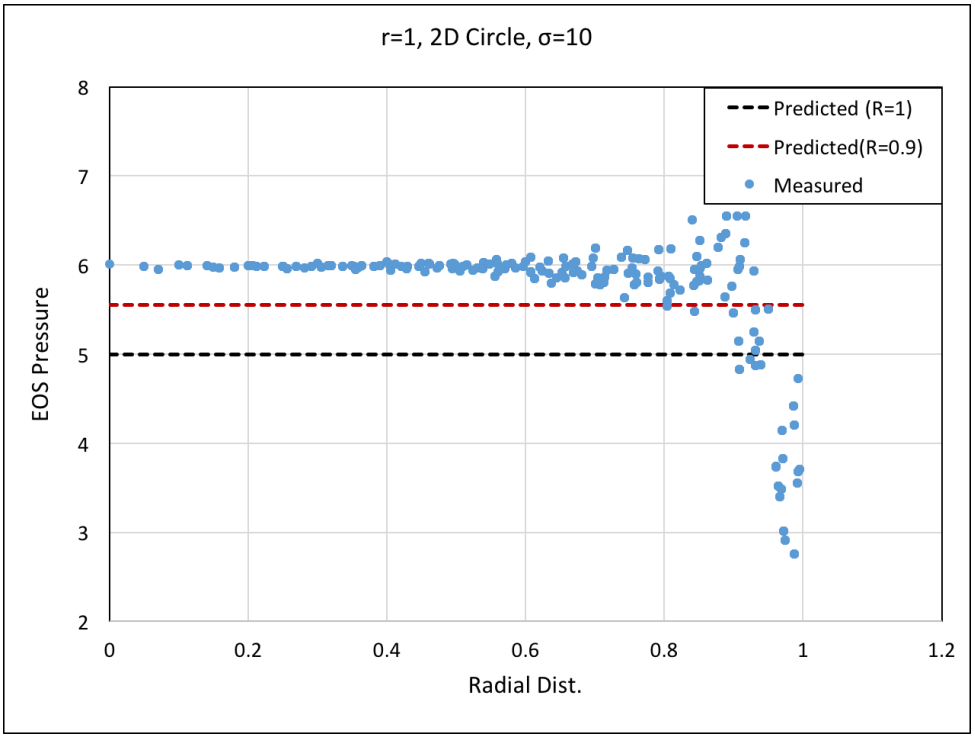

Figure 4.1: Plot of EOS pressure vs radial distance for a Young-Laplace equation validation test.

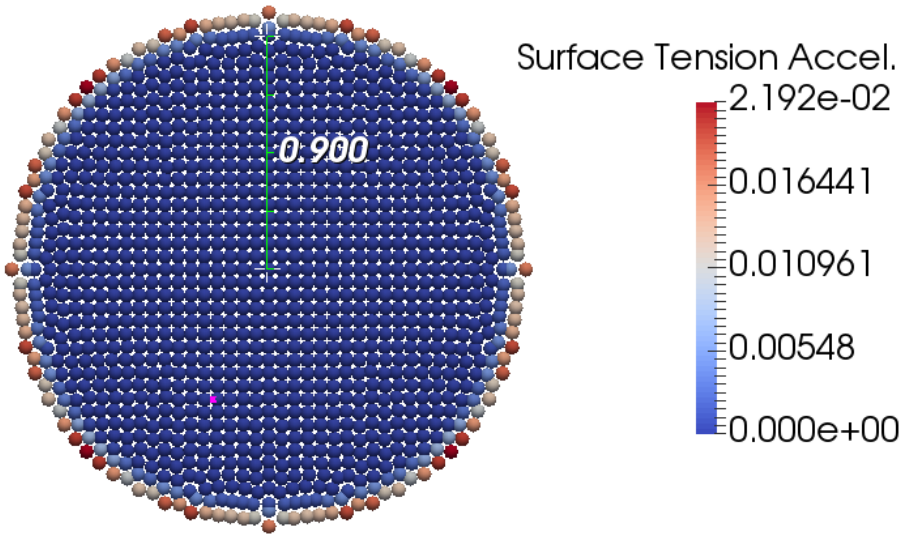

Figure 4.2: The surface tension acceleration contribution for a 2D circle of fluid under surface tension forces.

4.3 Isothermal WCSPH Formulation Verification

A variety of validation simulations were preformed to ascertain the viability of the proposed Isothermal WCSPH formulation in simulating an isothermally-incompressible fluid. The primary goal for developing the methodology was to allow for the modeling of thermally driven expansion/contraction with a second desired outcome being to adequately capture buoyancy forces from the resulting density field gradients. Isothermally incompressible fluids are not a well studied field and as such, no standard validation problems were found by the author in the literature with which to verify the method. Instead novel validation problems to confirm the accuracy and stability of the method in both idealistic and realistic (free surface) environments needed to be developed. Buoyancy on the the other hand is a well studied problem and several standard validation problems were found in literature and implemented.

4.3.1 Isothermal Incompressible Fluid Contraction/Expansion Verification

Test 1: Load-Free Expansion and Contraction of a Circle of Fluid The first verification problem was designed to ascertain the accuracy of the isothermal-WCSPH model in absence of all external forces or constraints. The proposed problem is as follows. A droplet of fluid, with a temperature-dependent reference density, is thermally cycled in open-space(gravity is removed). It is expected that the density of fluid will track the cycled reference density via expansions/contractions of the fluid volume. The fluid

density is guaranteed to track the reference density via the EOS and momentum-balance equation. However, volume in an SPH discretization is a free-variable, determined through particle motion and spacing, and the correct degree of expansion/contraction to satisfy isothermal-incompressibility is not guaranteed. Therefore, by measuring the volume of the simulated fluid and comparing with expected values, a verification of the accuracy of the isothermal-WCSPH model, in absence of all-other phenomena, can be made.

The measurment of volume is troublesome within the SPH formulation. While each particle has a specific mass and density, one cannot just directly divide the two to determine the actual volume of a particle. Because of the use of a Weakly Compressible formulation, numerical errors in the solution of continuity equation, usually from a poor particle approximations resulting from poor particle distributions, can produce slight differences between the volume change of a particle and its corresponding change of density. This can be compounded over time by the use of a pressure diffusion scheme such as $\delta - SPH$. Under large, directional forces its been observed that over time the "true volume" of a particle may not be equal to its mass over density. Therefore, in this experiment, the volume of the fluid was measured by preforming a Voronoi tessellation of the particle positions, and calculating the average volume of the Voronoi cells in a region. Voronoi tessellations provide an easy means for calculating the volume occupied by a particle distribution.

For the test case shown is this work, a sinusoidal temperature field was imposed homogeneously on the fluid droplet, $T(t) = T_{ref} + 50 * sin(2\pi t)$. The density was updated through Eq.(3.48) with $\alpha_T = 1$, resulting in density fluctuations of $\pm 5\%$. An inter-particle spacing of $dx/R = 0.05$, where R is the droplet radius, was used. The droplet motion was simulated for 10 cycles at which point no further changes were noted in the system.

The average volume of the simulated fluid, V, was calculated using a Voronoi tessellation of the particle positions at a given time[24]. The volume percent error is calculated as,

$$Error = 100 * \left| \frac{(V^{true} - V)}{V^{true}} \right|$$

where $V^{true} = \frac{m}{\rho_0(T)}$ is the expected volume. Figure 4.3 shows a plot of the volume error values over time for both a region of interior particles($r_i < 0.5R$) and a region of particles near the surface ($0.8R < r_i < 0.9R$). Free-surface regions are a known source of error in the SPH method so the use of both regions is necessary to fully verify the method. Voronoi tessellation is not unique on a free-surface requiring the use of a restricted subregion which does not include the fluid boundary. Figure 4.4, shows the Voronoi cells selected for the two regions. The results are very positive. The measured average volume of the SPH particles closely matched the expected volume (less than 0.4% error in the interior and 0.8% on the surface) throughout the length of the simulation indicating the methodology is accurately simulating isothermal incompressibility. In addition, the error didn't grow over the length of several cycles proving the method to be stable as well. A comparison of the boundary and interior plots reveal the error to be only minimally

higher on the boundaries. This is promising and points to the free surface having minimal impact on the scheme.

The regularized fluctuations of the volume error can be interpreted as a lag time in the fluid's tracking of the reference density values. This lag results from using a weakly compressible formulation. Recall that change of reference density produces a pressure increase in the fluid which drives fluid motion(expansion/contraction) and hence a density change. The speed at which this occurs determines how fast the fluid can track the correct density field value and is directly related to the stiffness of the fluid. Much like a spring-damper system where in this case the spring is the fluid stiffness and the dampener the fluid viscosity/delta-sph term. Low stiffness values will result in a slow tracking of the fluid reference density while higher stiffness values can overshoot the desired pressure value. A means of predicting the necessary fluid stiffness for given fluid viscosity/$\delta - term$ values to accurately track the density would be ideal but would require significant additional investigation which is outside the current scope of this wok.

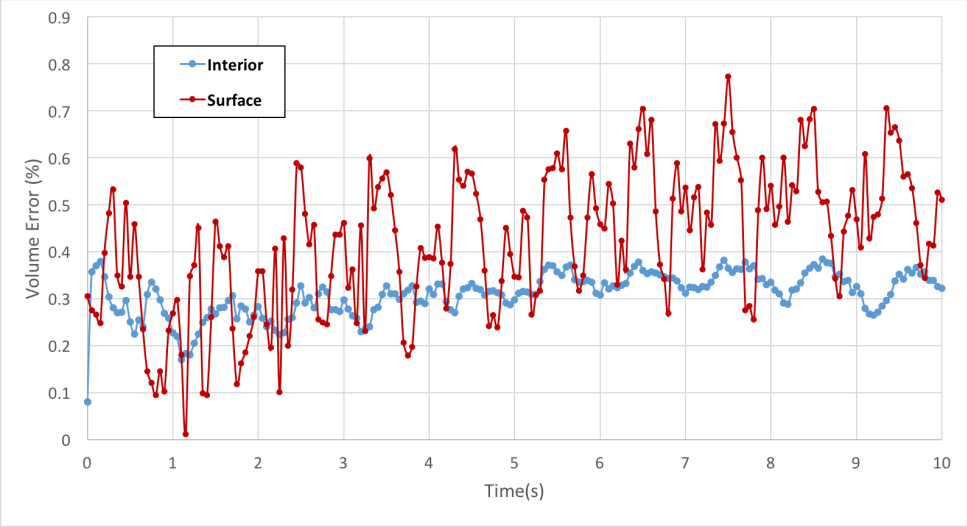

Figure 4.3: Volume error over time for an interior and surface region of the fluid for the validation test of cyclically expanding fluid under no external loading.

As noted in Sub-Section 3.4.1.1 the standard check of incompressibility, $\nabla \cdot \boldsymbol{u} = 0$, is no longer valid in the case of isothermal incompressibility, and a new standard relation was derived, Eq. 3.49. To confirm the accuracy of this derivation, measured velocity divergence values were compared against values predicted by Eq. 3.49. The results of this comparison are presented in Figure 4.5, which contains plots of the percent error of the velocity divergence over the length of the simulation for a region of interior particles and a region of boundary particles. The results are very promising and while the velocity divergence error values are larger than the volume error values, probably due to discretization error in the SPH discretization used to calculate the velocity divergence term, they are small enough confirm that the derivation of Eq. 3.49 is valid. Eq. 3.49 can therefore be

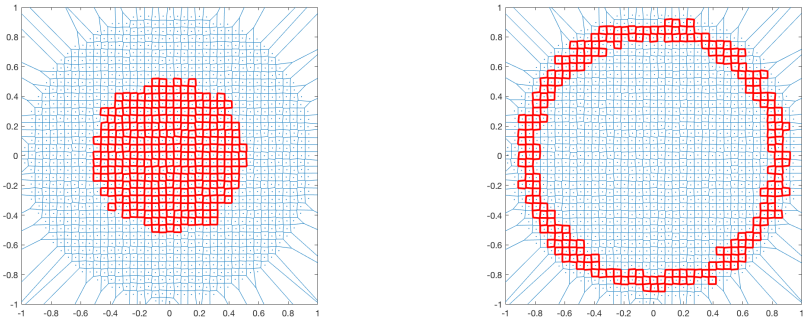

Figure 4.4: Interior and surface regions used for Voronoi area calculations.

used as a new metric for checking the correct enforcement of the isothermal incompressibility constraint. Initial, large inaccuracies in the simulated volume, at $t < 0.4sec$, are mostly like the result of a poor initial SPH particle configuration. After $t = 0.4sec$ the SPH particles have settled into a optimal configuration lowering the discretization error.

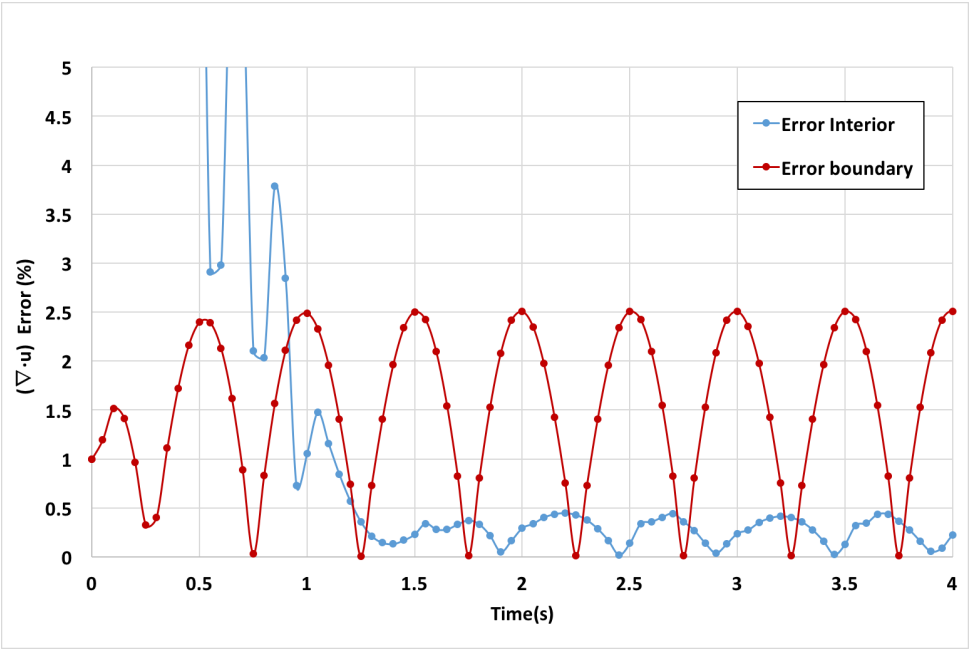

Figure 4.5: Volume divergence error over time for an interior and surface region of the fluid for the validation test of cyclically expanding fluid under no external loading.

Test 2: Cyclic Expansion of a Fluid with Increasing Amplitude After confirming the accuracy and stability of the Isothermal WCSPH framework under simplistic conditions, it was next desired to identify the max allowable compression/expansion range

of the formulation. To do this a variation of the cyclic loading test with increasing amplitude was preformed. The same sinusoidal temperature field as Test 1 was imposed but the density temperature coefficient was linearly increased in time

$$\alpha_T = 10\frac{t}{T_{tot}}.$$

As significant volume change was expected, it was necessary to evolve the smoothing length to ensure correct support was maintained,

$$h_{sml} = h_{sml,ref}\left(\frac{\rho_{ref}}{\rho_0}\right)^{\frac{1}{DIM}}.$$

A plot of the average density and reference density values for a section of interior fluid over time are shown in Figure 4.6. At low amplitudes the fluids density matched the reference value quite well. The fluid was able to simulate up to approximately a 140% increase in density before failing, through a splitting apart of neighboring SPH particles. This density increase is well within range necessary for the simulation of most physical processes including SLM. However if necessary, its believed greater expansion can be achieved by using particle remeshing schemes to preserve the mesh quality after a given amount of expansion. This would also preserve the discretization accuracy of the simulation.

In this simulation, an interesting failure mode was observed at higher fluid stiffnesses. A checker-boarding of density field appeared at high amplitudes, Figure 4.8. The checker-boarding was an unstable state and eventually the fluid density leveled out. At high rates of expansion however, failure of the fluid from large EOS pressures in the checker boarding would occur. This indicates that further investigation of the links between the fluid stiffness, the $\delta - SPH$ term, and the allowable rate/amounts of fluid expansion needs to be preformed.

Test 3: Expansion of an Isothermally Incompressible Fluid Underneath a Constant Density Fluid: Accuracy of isothermal-incompressible constraint under external forces and in a multi-phase fluid Gravity, solid boundaries, and a two-fluid system are introduced in a second verification problem to confirm the correct working of the isothermal-WCSPH model under practical (real-world) conditions. The second verification problem is as follows. An open topped column of fluid, consisting of two vertically-stacked fluids with identical properties, is initially at rest, Figure 4.9. At $t = 0$, the reference density of the lower fluid in the column, Fluid 1, is decreased at constant rate, $\dot{\rho}_0$, until $t/t_0 = 0.5$ at which point it is held constant. The reference density of the upper fluid of the column, Fluid 2, is held constant throughout the simulation. It is expected that Fluid 1 will expand, pushing up the entire column of fluid, while the volume of Fluid 2 will remain constant. The presence of gravity and boundaries will introduce forces in addition to those from the isothermal-WCSPH EOS. The presence of two fluids

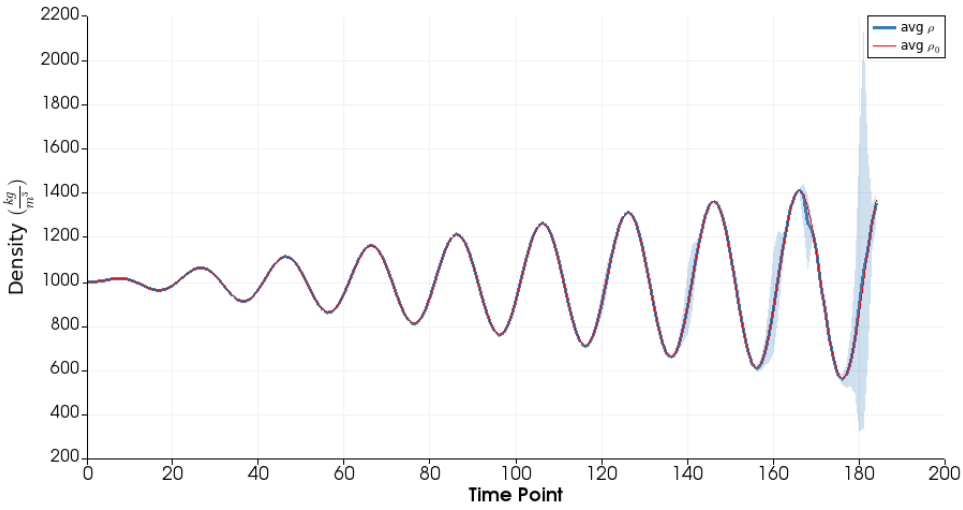

Figure 4.6: Plot of density and reference density over time for a cyclically expanding fluid with increasing amplitude.

with varying densities will evaluate the viability of the method in the presence of a density discontinuity.

For the case chosen in this work, a 10% reduction in density is achieved in Fluid 1 through the application of a non-dimensionalized reference density rate of $\dot{\rho_0} = -0.4$. Each fluid is of size $L_0 \times 2L_0$ and an initial discretization spacing of $dx/L_0 = 0.05$ is used. A constant gravity force of $g = 10m/s^2$ is applied.

The measured average density of Fluid 1 and Fluid 2 over time are compared to their expected values in Figure 4.10 The volume error over time for Fluid 1 and Fluid 2 is given in Figure 4.11. The fluid density neatly tracks the reference density value for both the expanding fluid and constant density fluid. As with Test 1, the volume error remains low ($Error < 1\%$) indicating correct enforcement of the isothermal-incompressibility constraint. The addition of external loadings, gravity and boundary forces, from the first validation experiment resulted in the appearance of oscillations in the density field and a spike in the volume error at the beginning ($t/t_0 = 0$) and end ($t/t_0 = 0.5$) of the density shift. The sudden changes in the reference density rate at these times requires a period equilibration of the density field to the reference value. The length of time for this equilibration is minimal and can be reduced through increased fluid stiffness or shortening of the numerical time step. No measurable density diffusion was observed across the interface between the upper and lower fluids and the interface remained stable. This indicates the robustness of the methodology in being able to capture volume changes of isothermally-incompressible,variable density flows in practical conditions.

Test 4: Sinking Fluid, $\delta - SPH$ vs $Standard\ SPH$ Finally, a simple problem of a heavy fluid settling inside a lighter fluid is chosen to demonstrate the usefulness of

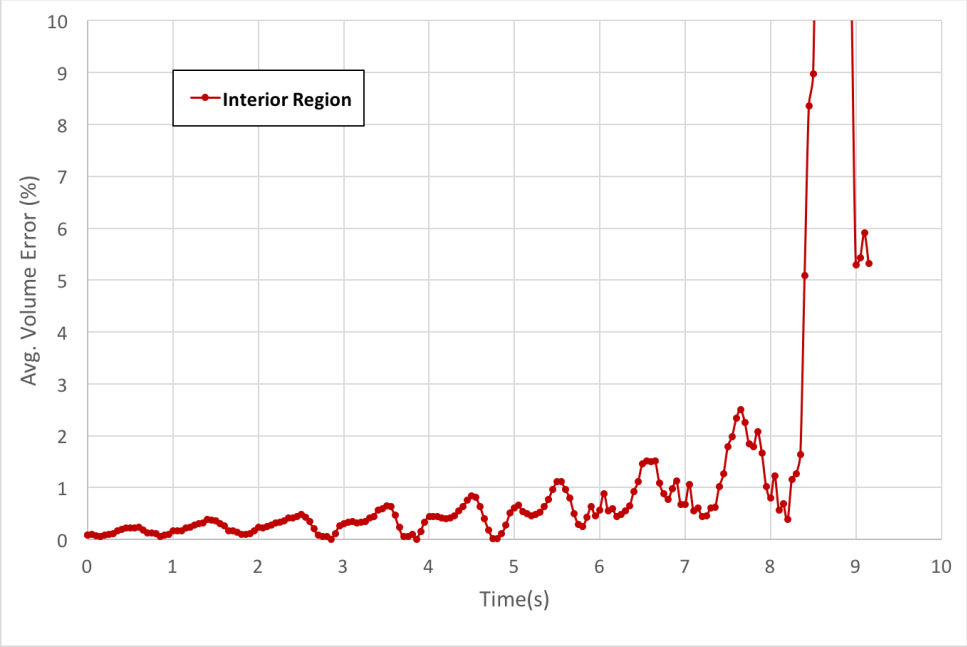

Figure 4.7: Plot of volume error from ideal for the increasing amplitude fluid expansion test.

having a methodology that is $\delta - SPH$ compatible. A $2000\frac{kg}{m^3}$ fluid, initially at rest, is placed inside a $1000\frac{kg}{m^3}$ fluid near the free surface. Over time the heavier fluid sinks into the lighter fuid. Figure 4.12 shows snapshots of the pressure field, generated using a Dealauny Triangulation, for the case using the standard WCSPH formulation and the case of using the modified $\delta - SPH$ scheme. The white line highlights the boundary between the two schemes. The case of no $\delta - SPH$ works well enough but has oscillations in the pressure/density field as expected. The case of the modified $\delta - SPH$ scheme shows smooth pressure fields and density fields(not shown). Also not shown here is case of using an incompatible $\delta - SPH$ scheme, which leads to large pressure fluctuations and a failure of the simulation for reasons discussed in the prior section. This simple test validates the need for utilizing a (compatible) $\delta - SPH$ scheme when simulating isothermally-incompressible fluids with varying densities.

4.3.2 Buoyancy Driven Flows Validation

Two test problems were used to ascertain the viability of the proposed methodology to simulate density buoyancy driven flows, a Rayleigh-Taylor Instability and a Differentially Heated Square Cavity.

Test 1: Rayleigh-Taylor Instability A Rayleigh-Taylor instability is created by placing a higher density fluid above a lower-density fluid in a column. In the absence of surface

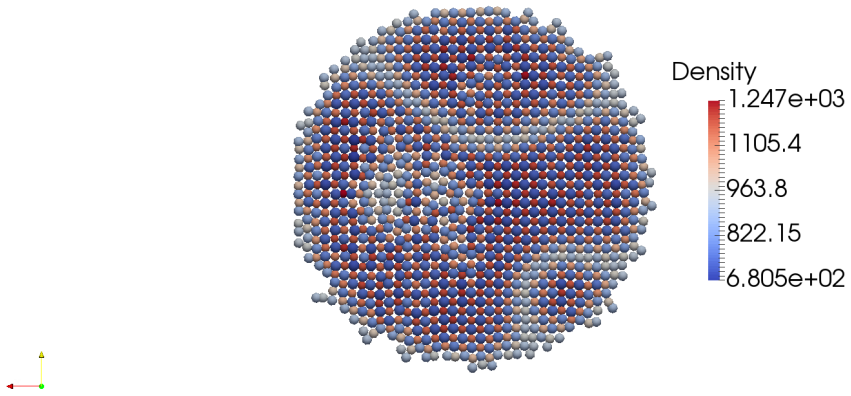

Figure 4.8: Checker-boarding of the pressure field at high rates of fluid expansion with a stiff fluid EOS.

tension, mixing will occur. Details of the reference problem are given by Szewc et al. [65]. Snapshots of the simulated fluid profile at several instances of time are given in Figure 4.13and compared against the results presented by Szewc et al.. As it can be seen, the flow simulated with the given methodology has a retarded motion compared to Swexce et al's results. While the fluid profile is qualitatively close to what is expected for the simulations it is about $1s$ behind the Szewc. results. This implies that the magnitude of the buoyancy force is lower then expected. Since the buoyancy force is not explicitly solved with this methodology this really is implying that the pressure force was lower then expected.

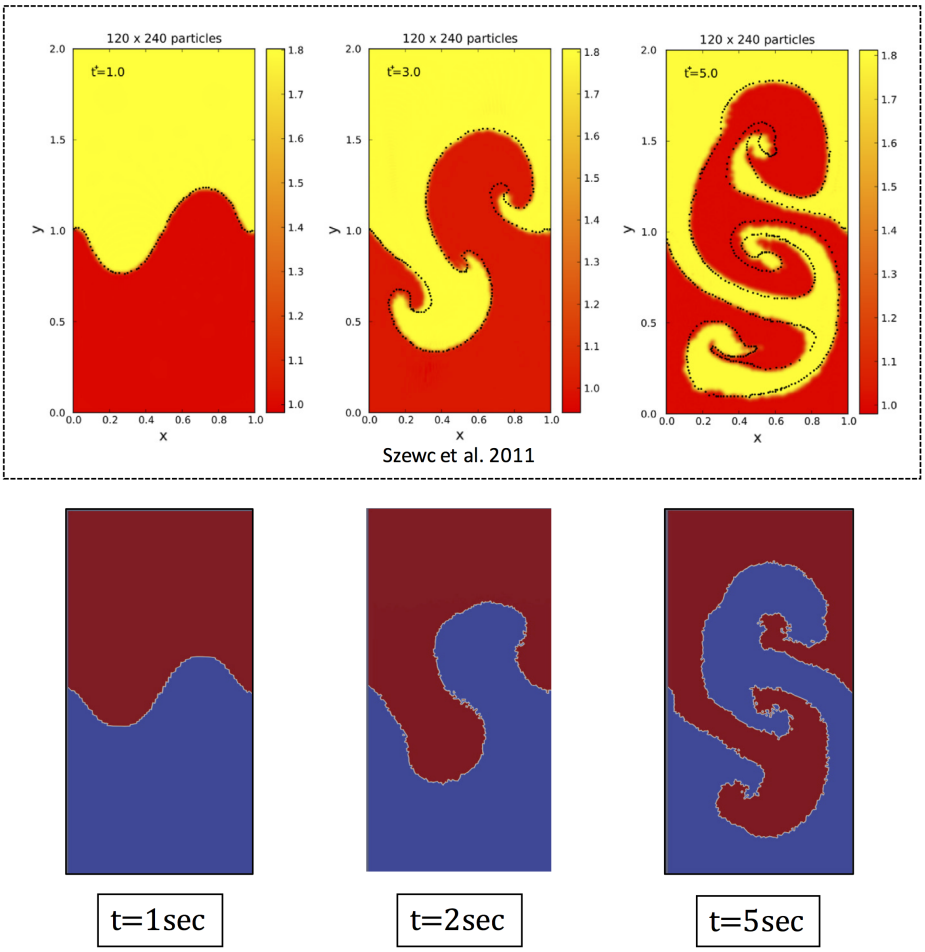

Figure 4.13: Comparison of fluid profile snapshots for Rayliegh-Taylor instability test with results from Szewc et al.[65]

It was initially believed this was due to the incorrect calculation of the EOS pressure leading to lower pressure gradients in the fluid. The EOS pressure field was verified for a hydrostatic test of a heavier fluid resting on top of a lighter fluid. The EOS profile as a function of depth is shown in Figure 4.14. It matches the predicted hydrostatic field quite well.

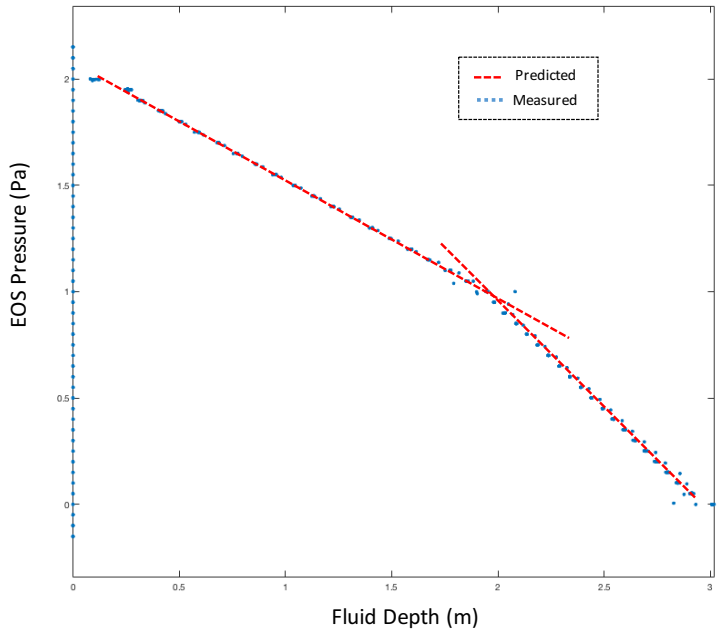

Figure 4.14: Comparison of the measured hydrostatic fluid profile to the expected value.

An examination of the pressure force profile for the fluid in motion however reveals the source of the sluggish motion of the fluid. As seen in Figure 4.15, striations occur in the EOS pressure field along the boundary between the two fluids. This leads to oscillations in the direction of the pressure force leading to a decreased overall buoyancy force at the boundary and a retarding of the motion. Its unclear what is causing the occurrence of these striations but one possibility is the use of the continuity equation to calculate the density field. These striations could possibly be the result of a lower potential fluid state that satisfies the continuity equations but leads to incorrect pressure calculations.

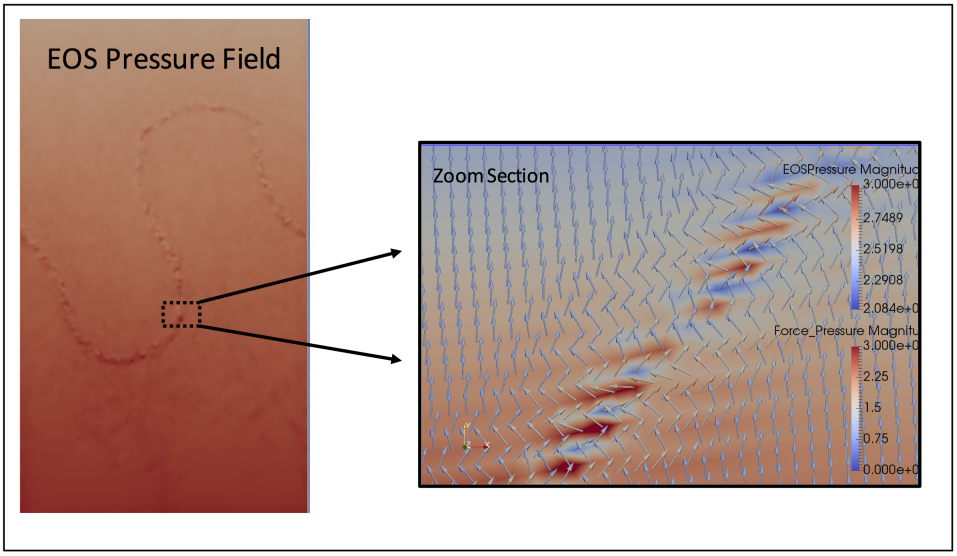

Figure 4.15: Pressure field striations visible at boundary between the two fluids.

Test 2: Differentially Heated Square Cavity It was initially believed that the pressure striations and retarded buoyancy motion were the result of having a sharp density discontinuity in the fluid and the method would be capable of simulating a problem in which the density variations were smoothed. Therefore it was attempted to simulate the flow in a differentially heated square cavity. A description of the problem formulations is again given by Szewc. et al.[65] Unfortunately a similar retardation of the flow is apparent in this simulation as well, Figure 4.16 . An inspection of the pressure force field, Figure4.17, reveals the same striations apparent in the the Rayleigh-Taylor instability.

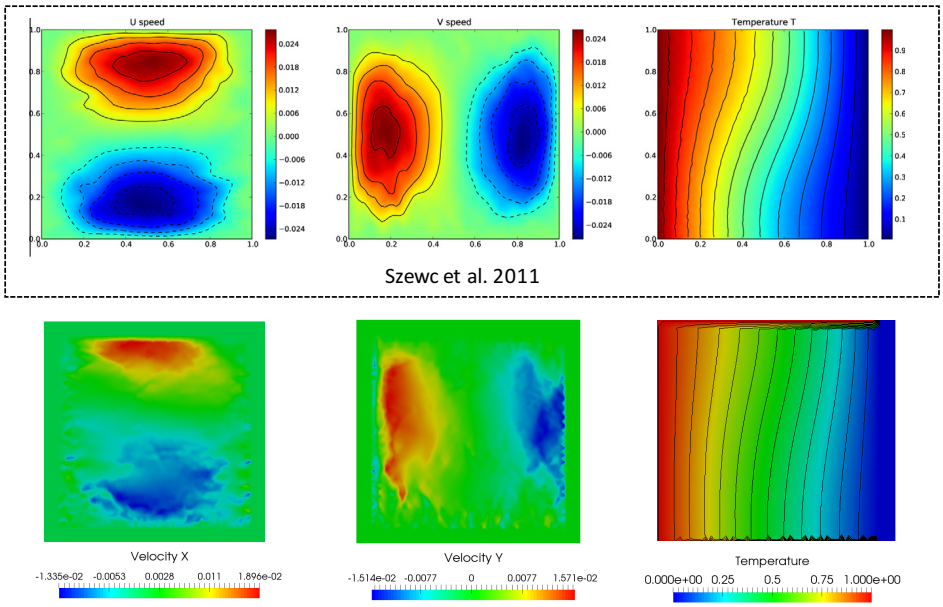

Figure 4.16: Comparisons of velocity and temperature fields for differentially heated cavity problem.

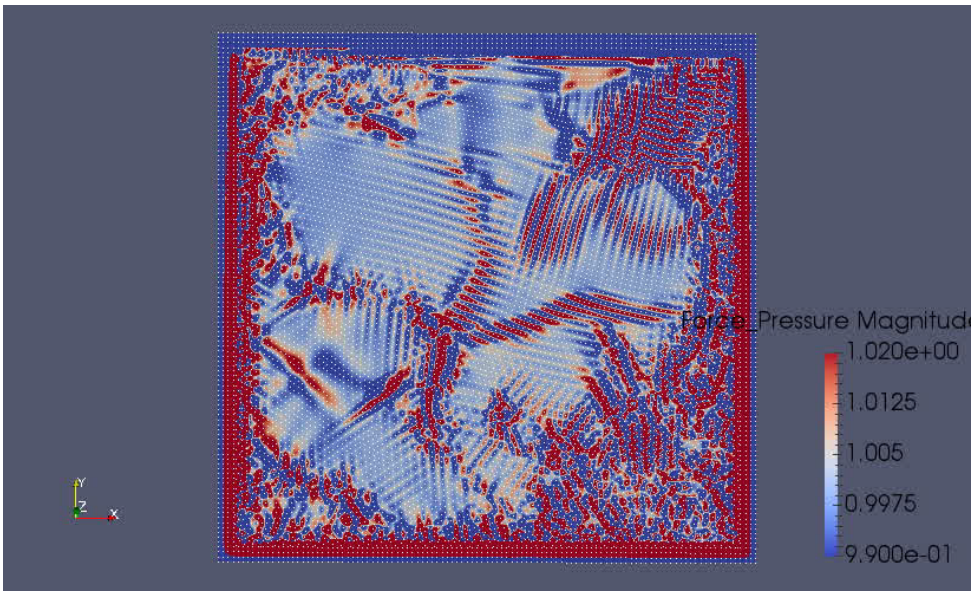

Figure 4.17: Pressure force field striations.

4.3.3 Conclusion

The proposed methodology works well for simulating the expansion/contractions of isothermally incompressible fluids but is incapable of accurately resolving buoyancy driven flows. It maintains incompressibility in the presence of sharp density discontinuities, when exposed to external forces(e.g. another expanding fluid), and over time as well. However it under predicts the expected buoyancy forces in buoyancy driven flows due to the presence of spatial oscillations in the pressure field(temporal oscillations are muted by the $\delta - SPH$ method). It is therefore suitable for simulating AM processes that involve rapid volume changes driven by thermal transitions but which do not require accurate simulation of buoyancy driven flows.

4.4 Spot Laser Weld Pool Validation Study

A validation case incorporating most of the physics considered in this research is set up by taking as reference the laser-welding experiments conducted by He et al. [32]. They made millisecond (3ms, 4ms), milimeter diameter pulsed laser spot welds on 304 stainless steel plates. By comparing the final weld pool dimensions from the He et al. experiment with those predicted by this numerical model, a check on the proposed AM-SPH methodology can be performed. Ideally, a track-weld experiment would be used to validate the methodology, as was preformed by Khariallah et al. [37], as it most similarly matches the motion of the SLM process, however the computational expense of such a simulation is outside of the capability of the currently implemented numerical code. Optimization of the code through more efficient function implementation and data structures combined with parallelization will make such a validation possible in the future.

Thermo-Mechanical Properties of 304 Stainless Steel Values for the thermally variable material properties of 304 steel used in this simulation were obtained from K. Mills [48] , Dubberstein et al. [20], and Valencia et al. [68]. The melting temperature is $T_{melt} = 1723K$ with a melting bandwidth of $\delta T = 100K$ (Eq. 3.47). While all material properties are functions of temperature, and not just material phase, for simplicity only the density, the surface tension, and $\frac{\partial \sigma}{\partial T}$ are fully functions of temperature in this work. All other material properties are linearly interpolated between their solid and liquid phase values by the following equations;

$$\theta = \begin{cases} \theta_{solid} & s = 0 \\ (\theta_{solid} - \theta_{liquid})\, s + \theta_{solid} & 0 < s < 1 \\ \theta_{liquid} & s = 1 \end{cases}$$

where θ is a representative material property and s the state variable. The solid and liquid values of all relevant material properties are given in Table 4.1. The liquid thermal

Material Property	Solid Value	Liquid Value	Units
μ	1.0	0.01	$\frac{kg}{m \cdot s}$
c_p	711.17	937.35	$\frac{J}{kg \cdot K}$
$k_{thermal}$	20	209.3	$\frac{J}{m \cdot s \cdot K}$
$Surface\ Absorbtion\ Coefficient$[32]	0.27	0.27	-

Table 4.1: Material property values for 304 Steel

conductivity is scaled by a factor of 10. This is a common practice in welding simulations and takes into account additional heat transfer due to turbulence in the flow[57, 32].

The material absorptivity was set so that all non-refelcted laser power was abosrbed by the SPH particles on the surface of the weld.

The density is a function of temperature and is given by:

$$\rho = \begin{cases} 8020\frac{kg}{m^3} - 0.501\frac{kg}{m^3 K}\left(T - 298K\right) & s = 0\ \ (solid) \\ 7443\frac{kg}{m^3} - 6.03\frac{kg}{m^3 K}\left(T - 1673K\right) & 0 < s < 1\ \ (transition) \\ 6840\frac{kg}{m^3} - 0.70\frac{kg}{m^3 K}\left(T - 1773K\right) & s = 1\ \ (liquid) \end{cases}$$

The solid density equation is obtained from the experimental work of Mills [48], the liquid density equation from Dubberstein et al. [20], and because of a lack of experimental data the mushy zone is a linear fit between the two. The density of liquid steel is only experimentally measured by Dubberstein et al. up to $1923K$. In this model, a linear extrapolation is made for temperatures above this. The surface tension of 304 steel is both a function of temperature and the concentration of alloying Sulfur. In this work that concentration is assumed to be constant, $a_s = 0.0022wt\%$. The surface tension as a function of temperature is given by Sahoo et al.[60] as;

$$\sigma\left(T\right) = \sigma_0 - A\left(T - T_m\right) - R \cdot T \cdot \Gamma_s log\left(1 + k_l \cdot a_s \cdot e^{\left(\frac{-\Delta H_0}{R \cdot T}\right)}\right)\frac{N}{m} \tag{4.2}$$

where $\sigma_0 = 1.943\frac{N}{m}$, $A = 0.5 * 10^{-3}\frac{N}{mK}$, $R = 8.3145$, $\Gamma_s = 1.3 * 10^{-8}$, $k_l = 0.0032$, and $\Delta H_0 = -166 * 10^3$. An equation for $\frac{\partial \sigma}{\partial T}$ as a function of temperature is obtained by taking the derivative of Eq. 4.2 with respect to temperature. A unique property of the Marangoni forces in stainless steels is the direction of the force switches from opposite of ∇T at low temperatures, to parrallel to ∇T at high temperatures. Numerous numerical works ignore this phenomena and assume a constant $\frac{\partial \sigma}{\partial T}$ coefficient as this increases model stability. This is not done in this work in order to fully capture the physics of the process.

The viscosity of the fluid was linearly ramped in the transition between liquid and solid state, and ramped down in the vice versa, to simulate the mushy region melt dynamics. While ideally, the viscosity would be ramped to infinity as the mushy region became solid, this is numerically impossible. It was discovered that a viscosity of 100 times the fluid viscosity was the max allowable for the solidified mushy region while still maintaining

Property	Value
c_0	$50\frac{m}{s}$
$Kernel$	$Wedland\ C2$
$h/dxreg$,	1.2
$h/dx(surf.ten.)$,	1.8
dim	3
dx	$0.05mm$
$total\ particles$	19000
dt	$6E-08s$
$sim.\ time$	$\approx 200hrs$

Table 4.2: Simulation parameters for laser weld validation test.

model stability. Its unclear why this was the maxed allowed value as the viscosity CFL condition was still lower then the simulation time step. Why stable simulation of larger viscosity ramps was unobtainable will be investigated in future works.

Model Parameters and Assumptions The SPH parameters used in the simulation are given in Table 4.2.

It was assumed that no surface tension existed between the solid and liquid phases of the material. It is believed that the contact interface between the two would have a smooth transition between states and thus no surface tension would result. In addition, thin layers of fluid (1-2 particles in thickness) were prevented from developing surface tension forces. The CSF-SPH formulation requires significant support to operate correctly and thin fluid layers were found to have erroneously high surface tension values. A third assumption in the model is that the sound speed of a particle was lowered by a factor of 5 when melting. This was done to prevent rapid expansion forces from ejecting the particles off the solidified body it was attached too. The solid-liquid pressure relation used in this methodology is unable to prevent seperation if the volumetric expansion is rapid enough. By lowering the stiffness, the rate of expansion is also lowered. This was necessary for model stability and its effects on the simulation outcome are thought to be minimal.

When a perfect grid-lattice was used as initial placements for the SPH particles in the simulation, un-natural motion of the SPH particles due to symmetrically opposed forces was observed. For example, a particle placed on the surface in the center of the laser profile would experience equally opposed surface tesnion forces and be prevented from moving. In order to avoid any influence from the initial placement of the SPH particles, the z-height of vertical columns of particles was randomized and the entire mesh was offset from center in the x-y plane by $\Delta x = 0.33h_{sml}$ and $\Delta y = 0.33h_{sml}$. This offsetting and randomization of the height prevented any unphysical motion of the particles and the z-height randomness can be further reasoned as a roughening of the surface.

It should be noted that typically when a laser welding experiment is numerically

simulated (e.g. [57, 32]), an assumption of a flat weld-pool surface is enforced (i.e. $u_y = 0$). It is claimed that this assumption comes from an observation that the final weld-pool surface is relatively flat, however its use is more than likely due to the use of fixed-grid numerical methods (FVM) where a deformable free surface is difficult to model. In the above experiment, it was noted that significant weld pool surface deformation occurred during the melt phase, and it is believed that neglecting this deformation and the mechanism that keeps the weld pool surface from spilling over (the normal surface tension on the edge of the weld pool) is necessary to accurately model this type of problem.

A Dirchlet temperature boundary condition of $T = 293K$ was enforced on the bottom of the weld-substrate using a layer of three boundary particles. A zero conduction boundary flux condition was imposed on the surface. This is easily accomplished in SPH by leaving the boundary on the surface as free(no boundary particles). A radiative flux and convective flux was imposed on the surface SPH particles. The substrate layer was chosen to be thick-enough such that the effect of the boundary condition on temperature field in the field was minimized.

4.4.1 Results

A simulation of the 3ms-microsale laser weld pulse experiment preformed in He et al. [32] was carried out. The simulation was run until the weld-pool fully solidified. The experiment parameters are listed in Table 4.3. A side-by-side comparison of the simulated weld pool at max dimensions is compared against the melted region micrograph given in the work of He et al. in Figure 4.18. The numerical weld-pool dimensions and those of the physical experiment along with the precent error are given in Table 4.3. As one can see the measured values are roughly close to those of the physical experiment($Error < 0.4\%$), however the shape of the weld pool is different then that of the micrograph. The weld pool in the numerical simulation is more rounded. A perfect hemisphere is expected if no fluid convection occurs and the laser heat is only dispersed via conduction. This implies that the model is not accurately capturing the re-circulative weld pool motion.

Property	SPH Exp	He et al.	Percent Error
radius	$0.46mm$	$0.48mm$	4.3%
depth	$0.25mm$	$0.26mm$	3.8%

Table 4.3: Laser welding validation test results. A comparison of the simulated weld pool dimensions with that of the work of He et al.

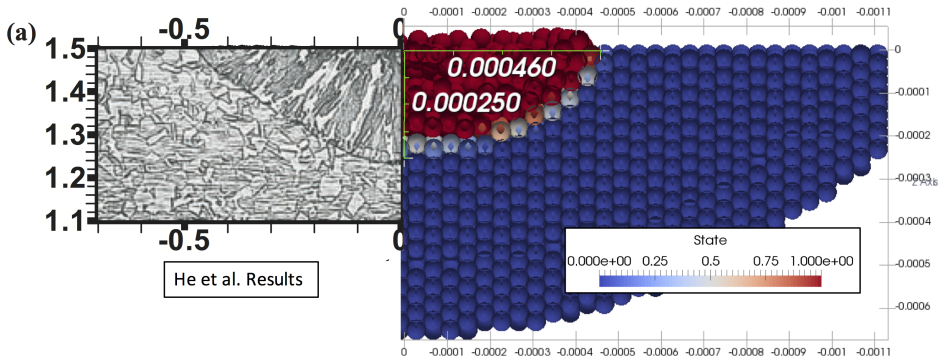

Figure 4.18: Maximum dimensions of the simulated weld pool as compared to micrograph from He et al. experiments.

Discrepancy between the two weld pools can be the result of numerous factors. (1) The material properties used in the simulation do not match those of the 304 Steel used in the experiment. A noted above, the surface tension is a function of alloying Sulfur concentration. It is unknown at what purity the tested 304 steel sample is. In addition, a constant surface laser absorbtion coefficient of 0.33 was used. However this value is only just the known value of surface absorption for the solid phase at lower temperatures. The surface absorptivity of liquid or elevated temperature solid 304 steel is not well known due to the difficulty in measuring it. Having a higher or lower surface absorbtion coefficient would significant influence the amount of thermal energy transmitted into the weld pool and hence its size. (2) A second source of error is insufficient mesh resolution. A higher mesh resolution is most likely necessary to fully capture the re-circulating flow of the weld pool. This recirculation would influence the shape of the weld pool by redistributing the heat flow in the weld pool. However, this simulation alone took approximately 300hrs of simulation time. Higher-resolution simulations can only be carried out once optimization of the code has been performed. (3) A third source of inaccuracy could be having too insufficient of a sound speed for the fluid phase. The predicted max fluid velocity speed for the weld pool was given by He et al. as $1m/s$. The standard sound speed for the WC-SPH method would therefore be $c_0 = 10 \times 1m/s$ [52]. However, even when using a sound speed of $c_0 = 50m/s$ fluid splitting was observed and incompressibility was not maintained. Using a higher sound-speed is impossible as the simulation time would become

un-attainable. A better means for predicting the maximum required sound speed needs to be formulated. It is believe it needs to be linked to the dominate force in the model, that of the Marangoni surface tension. However no CFL conditions for Marangoni forces were found in literature. (4) A fourth source error, could be the observed separation of neighboring solid and liquid SPH particles. The method for simulating the pressure force between solid and liquid particles was found to be insufficient to prevent lift-off of SPH liquid particles from their solid neighbors. This is completely unphysical and occurred at lower force values then the splitting noted in point (3) indicating its not entirely resulting from the choice of material stiffness. It is believed that a better formulation for the interaction between solid and liquid SPH particles is necessary for future works.

Overall, the results of this laser spot welding validation test are promising but are insufficient to declare the method fully validated. It is recommend that future validation attempts should use a different validation problem then that of the He et al. laser spot welding experiments. It was noted that the time and length scale of the problem was insufficient to establish a steady state re-circulation of the weld pool. A steady-state laser spot welding experiment like that given by Pitschender et al [57] where the lasering times are in seconds, not milliseconds, would provide a better verification of the AM-SPH model. However again, simulating a seconds long, millimeter scale lasering pulse is outside the computational capabilities of the current implementation of the method.

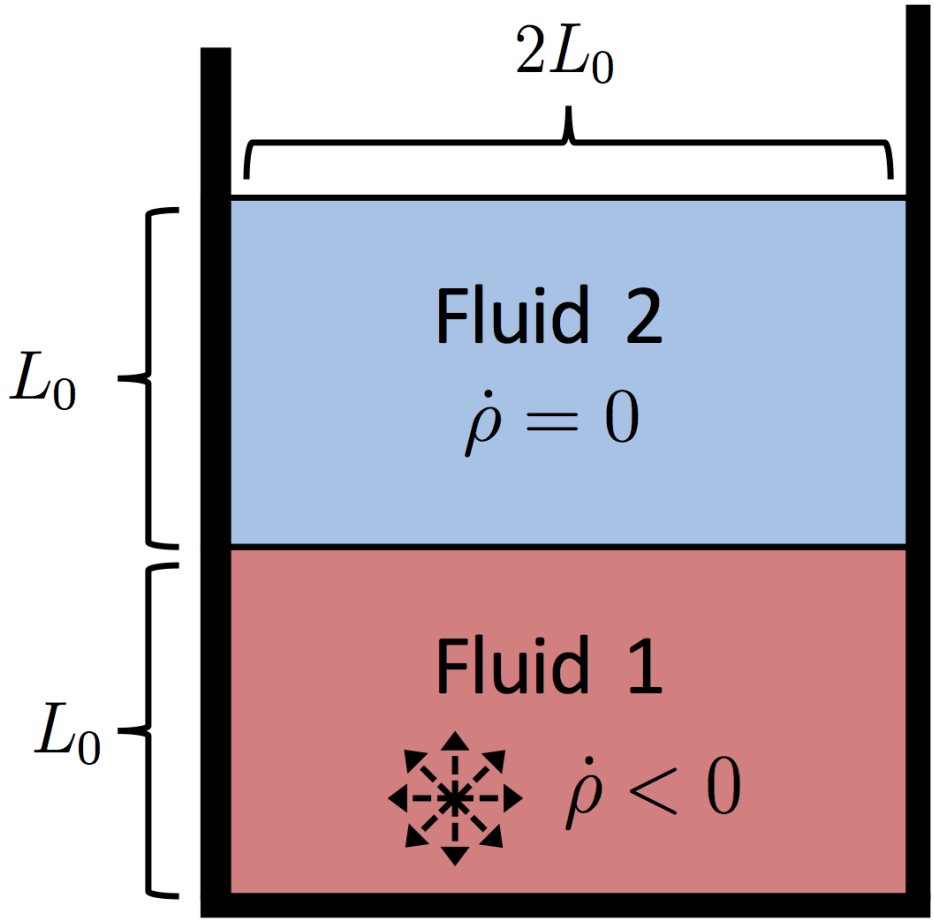

Figure 4.9: Schematic of the bi-fluid column simulated in isothermal-WCSPH verification Test 2.

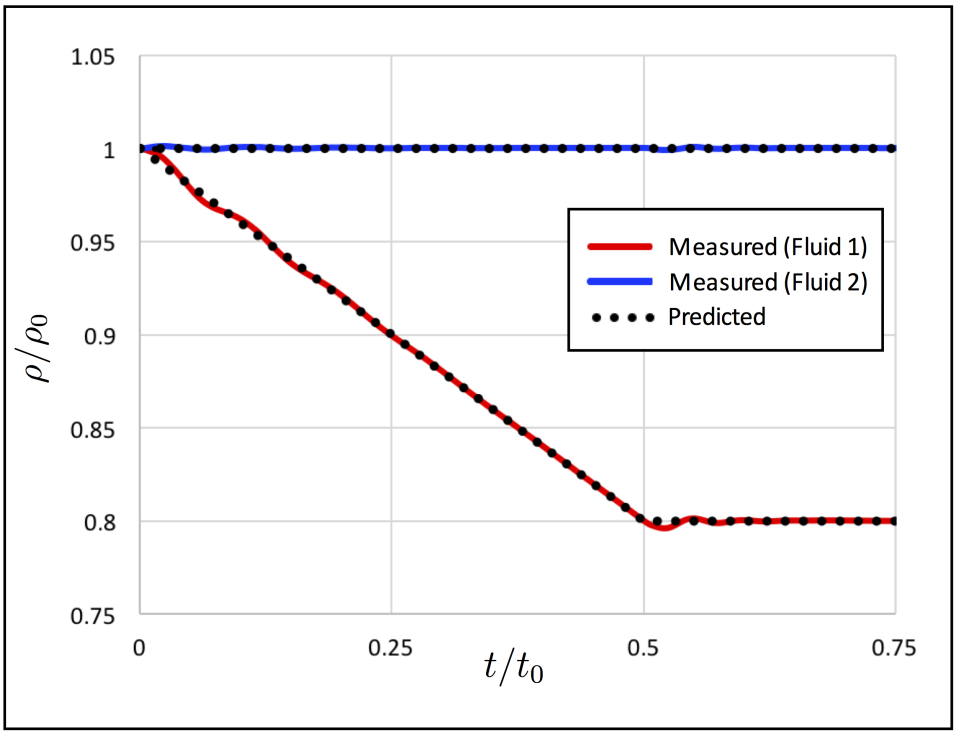

Figure 4.10: Non-dimensionalized density vs time of Fluid 1 and Fluid 2 for isothermal-WCSPH verification Test 2. Dotted lines give the value of the reference density for the fluid.

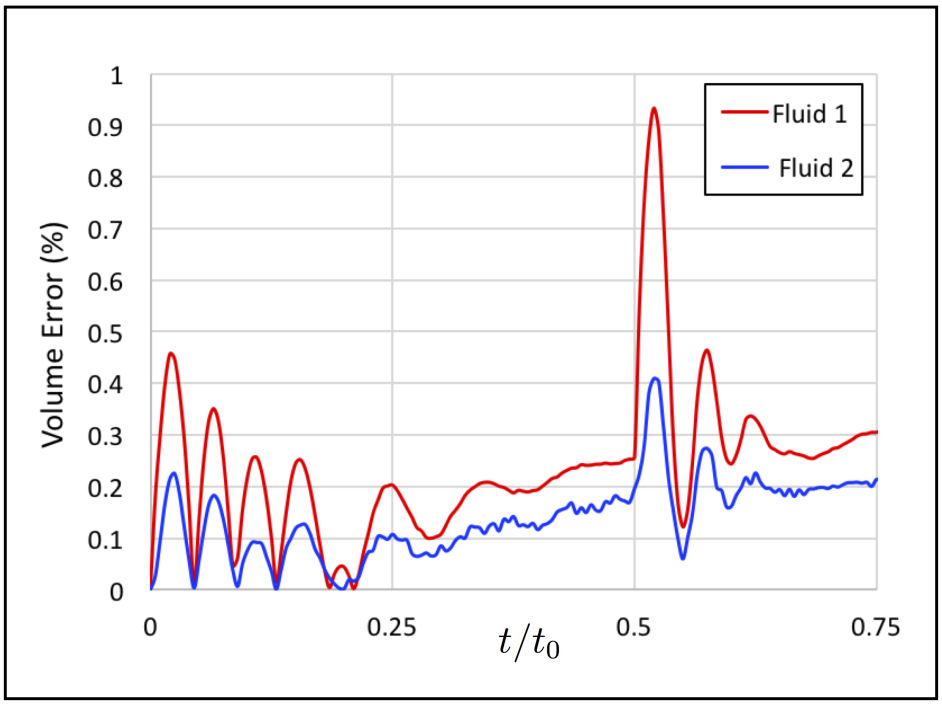

Figure 4.11: Volume Percent Error vs time for Fluid 1 and Fluid 2 for isothermal-WCSPH verification Test 2.

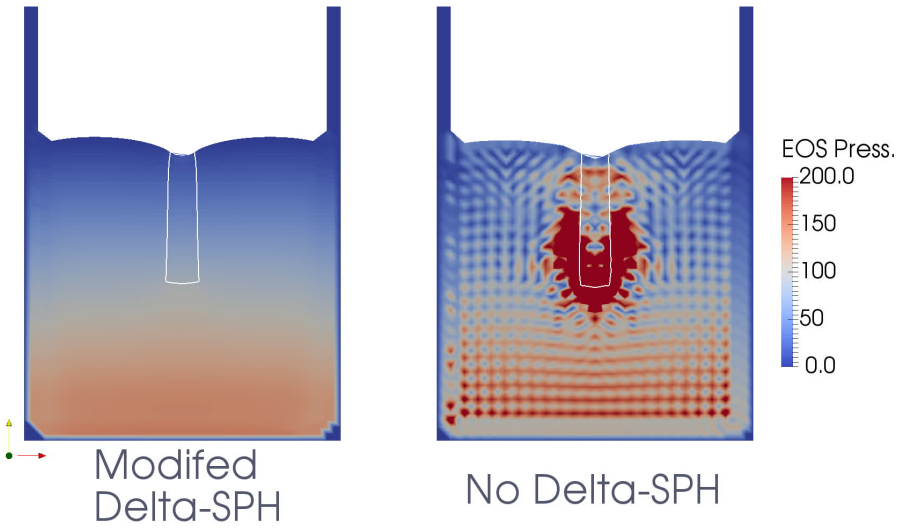

Figure 4.12: Pressure fields for the simulation of a heavier fluid, outlined in white, sinking in a lighter fluid using the modified $\delta - SPH$ formulation and the standard WCSPH formulation (no $\delta - SPH$).

Chapter 5

Numerical Experiments

5.1 Laser Melting of a Particle Bed

The Particle Bed Selective Laser Melting process, described in detail in Section 2.2, was chosen as the first application of interest to apply the AM-SPH methodology developed in this work too. The goals of developing the AM-SPH methodology were to be able to provide insight into the physical processes occurring during the laser melting of a single-track along the particle bed as well as to offer process improvements through parameters studies of varying processing parameters(laser power, laser width, particle diameter, etc.). While this work is merely an initial effort into developing an industry/research viable AM-SPH methodology, with improvements of various SPH discretizations(surface tension for example) as well the inclusion of additional physics(e.g. vaporization and recoil pressure) still necessary, an attempt at satisfying these two goals will still be made in this work. However given, the relatively large computational burden of the current implementation of this methodology, a tradeoff must be made between the dimensionality of the simulation and the resolution/scale of the simulated problem. To balance these competing factors both high-resolution, full-track scale 2D simulations as well as a lower resolution, smaller scale 3D simulations were preformed. 2D simulations significantly reduce the computational burden allowing for larger domain and higher resolution simulations. In the future it will be desirable to conduct high-resolution full scale 3D simulations, but this is outside the scope of the current effort. 2D simulations will be used to preform parameter studies of the methodology while the 3D studies will shows its extension to the dimensions of the real world.

5.1.1 Laser Melting of a 2D Particle Bed

A 2D simulation of the laser melting of a real-scale particle bed track was preformed. The material properties and model assumptions were the same as the spot laser validation test, Section 4.4. A regular distribution of powder particles was used as the problem geometry. In actuality, the spacing between particles would be more irregular due to the randomized nature of a real world particle bed. The simulation parameters used are given in Table 5.2. To prevent overheating of ejected SPH particles if an ejected SPH particle's temperature reached $6000K$ it was removed from the simulation. A no-conduction/no-convection flux boundary condition was imposed on the top surface. The bottom surface of the substrate had a Dirchlet temperature condition of $T = 293K$ that was implemented using a layer of boundary particles. The substrate layer was chosen to be thick-enough such that the effect of the Dirchlet boundary condition on the temperature field was minimized.

As a starting point, the process parameters and physical dimensions were taken from the 3D-FEM simulation work of Khariallah et al. [37]. The laser power and scan speed where the same as Khariallah et al. but a constant particle radius of $r_p = 25\mu m$, rather then the radii range of $r_p = 27\pm5\mu m$ used by Khariallah et al, was used in this experiment. The experiment parameters are listed below in Table 5.1. The simulation was carried out

Property	Value
$Laser\ 2\sigma\ Wdith$	$54\mu m$
$Laser\ Power$	$150W$
$Scan\ Velocity$	$2m/s$
$Laser\ Profile$	$Gaussian$
$Particle\ Radius$	$25\mu m$
$Track\ Length$	$1.2mm$
$Track\ Depth$	$0.33mm$

Table 5.1: Process parameters for 2D laser melting of a powder bed track.

until the track had fully solidified, around $t_{final} = 1.125ms$.

Snapshots of the state-field with temperature contours overlaid at several time points over the course of the simulation are shown below in Figure 5.1. The particle bed is completely solidified($T = 293K$) at $t = 0ms$ when the laser is turned on. The Gaussian-laser power distribution and penetration into the particle-bed are shown in Figure 5.1-A. The initial melt pool shape is highly volatile upon formation (Figure 5.1-B). The high laser-heating rate places heat into the body at a faster rate then it can diffuse into the substrate leading to high-thermal gradients. These thermal gradients result in strong Marangoni convection in both the $+x$ and $-x$ directions and to a deepening of the melt pool as particles under the laser are wicked away. Midway through the lasering process, the melt pool has reached a more-steady state(Figure 5.1-C). Mid-lasering a semi-steady state occurs where three zones can be visibly demarcated; a highly dynamic melt pool directly under the laser region, a slower moving melt-pool tail, and the solidified newly deposited track. These same zones and the occurrence of a "steady-state" are also noted by Khariallah et al. in their work. The melt pool penetrates into the substrate layer, completely melting the deposited particles, and providing a solid connection between the two. Interestingly, the melt pool extends in front of the moving laser heat source, propelled by the Marangoni convection in the $+x$ direction. The melt pool surface is relatively flat as the strong Marangoni convection away from the melt region smooths out any balling of the surface from normal surface tension forces. However, at certain locations necking of the melt-tail can occur, indicated by the arrow in Figure 5.1-D leading to the so called "balling-effect". This effect is reasoned to be the result of Rayliegh-taylor instabilities which would be much less pronounced in a 2D model. The strength of the Marangoni convection is apparent in the melt fluid ejected off the end of the substrate in the $-x$ direction. The melt pool remains liquid after the passing of the laser-beam with a long melt pool tail, around $400\mu m$ in length. The material remains in a mushy-state even long after the laser has passed. This is due to lower-thermal gradients, the energy released in the solid-liquid phase change, as well as the lower thermal conductivity of the solid phase. The final profile of the melt-track is relatively flat (Figure 5.1-F) although a pinching of the melt pool results in the solidification front separating two melt sections leading to the

Property	Value
c_0	$20\frac{m}{s}$
$Kernel$	$Wedland\ C2$
$h/dxreg$,	1.2
$h/dx(surf.ten.)$,	1.8
dim	2
dx	$4\mu m$
$total\ particles$	13000
dt	$1.2E-08s$
$sim.\ time$	$\approx 36hrs$

Table 5.2: Simulation parameters for 2D laser melting of particle track.

formation of humps(the 2D version of balling).

A closer look at the steady-state melt-pool (Figure 5.1-C) provides insight into the complex interactions between vying physical phenomena at the microscale during the SLM process. Focused views of the temperature , velocity, and surface tension fields are provided in Figure 5.2. As seen in Figure 5.2-A the highest temperatures occur directly beneath the laser beam although the melt-region extends out in front of the moving source(i.e. particles are being melted in front of the moving beam). The source of this is the strong Marangoni convection currents pushing fluid out in front of the moving laser source as well as back behind it. As seen in Figure 5.2-B&C the highest Marangoni forces and highest velocities in the melt pool are actually in the positive x direction moving out in front of the beam. The thermal gradients are highest here propelling the fluid forward. The fluid moving forward rapidly heats the oncoming powders, melting them before they come in contact with the laser beam. Its is believed that pre-heating/melting of the oncoming fluid allows for a smoother melt flow as the rate of thermal expansion is minimized. In addition, at high enough laser powers/slow enough scan speeds, this effect can leads to the ejection of some fluid off the front of the melt pool, referred to in the field as spattering. This same "bow-wave" effect was noted by Khariallah et al. [38]in their FEM simulation however they concluded it was the result of recoil vapor pressure in the melt(a phenomena not models in this work). Inertia from the initial high Marangoni forces propel the fluid the laser source backwards along the track. Close to the melt-pool these surface flows lead to re-circulation vortices as seen in Figure 5.2-C. Re-circulation is known to extend the depth of melt pools and is desirable for penetrating into the substrate layer. Khariallah et al. also reasoned that re-circulation can result in trapped voids however this effect was not seen in this work The effect of the volumetric expansion is not as visible in these simulations. It could be contributing to the flow outward under the laser beam however a direct measurment of its value is difficult to obtain as its impossible to separate the pressure from volumetric expansion and that required to maintain incompressibility. It is apparent from these simulations that the

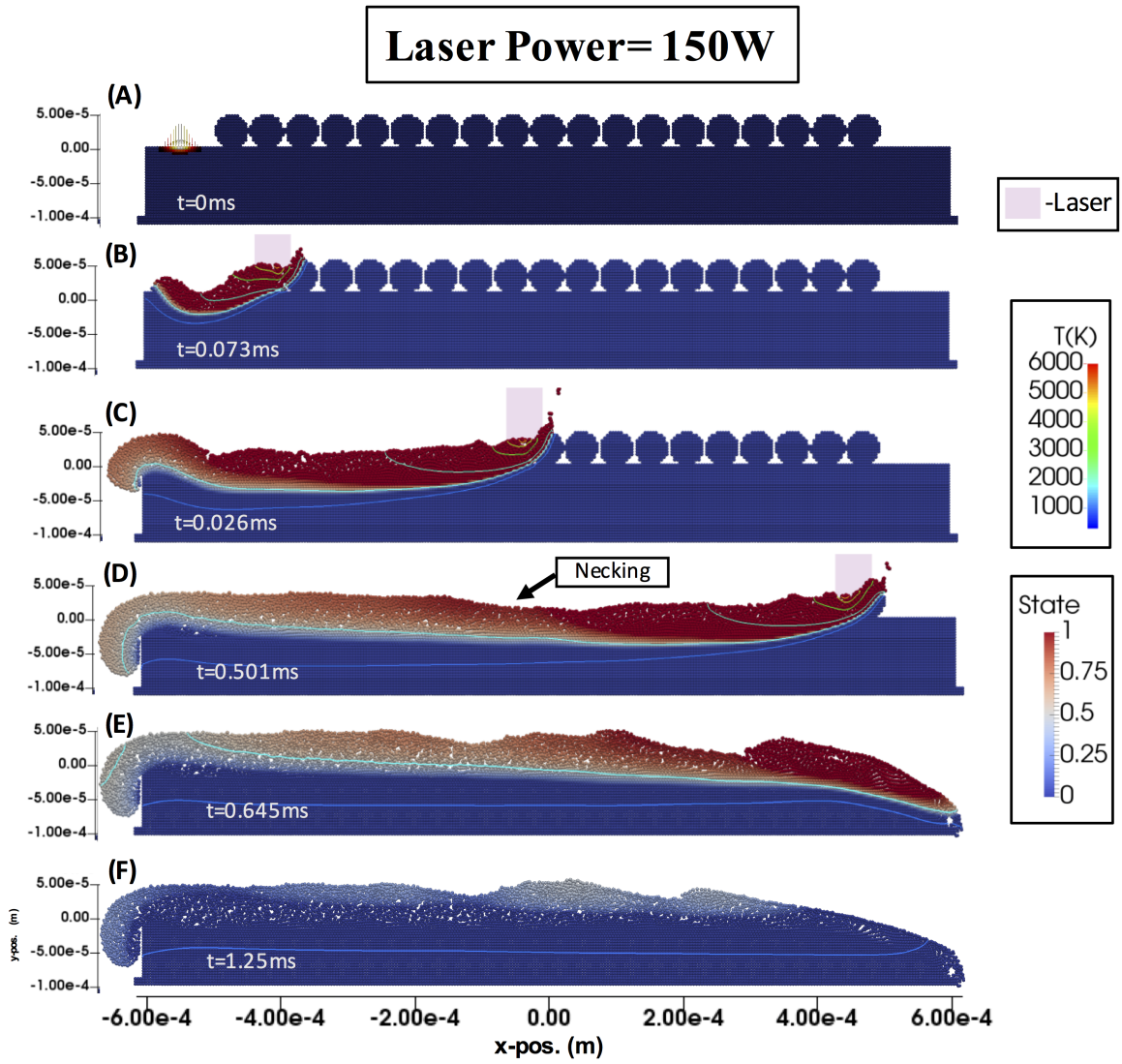

Figure 5.1: Snapshots of the material state and temperature contours at very times for the laser melting of a 2D particle bed with the experimental parameters described in Table 5.1.

driving motion for the growth and propagation of the melt pool is Marangoni forces emanating out under the translating laser beam sources. The competing effects of the rate of melt-pool solidification, surface melt inertia, minor marangoni convection, and normal surface tension determine the resulting roughness of the track surface.

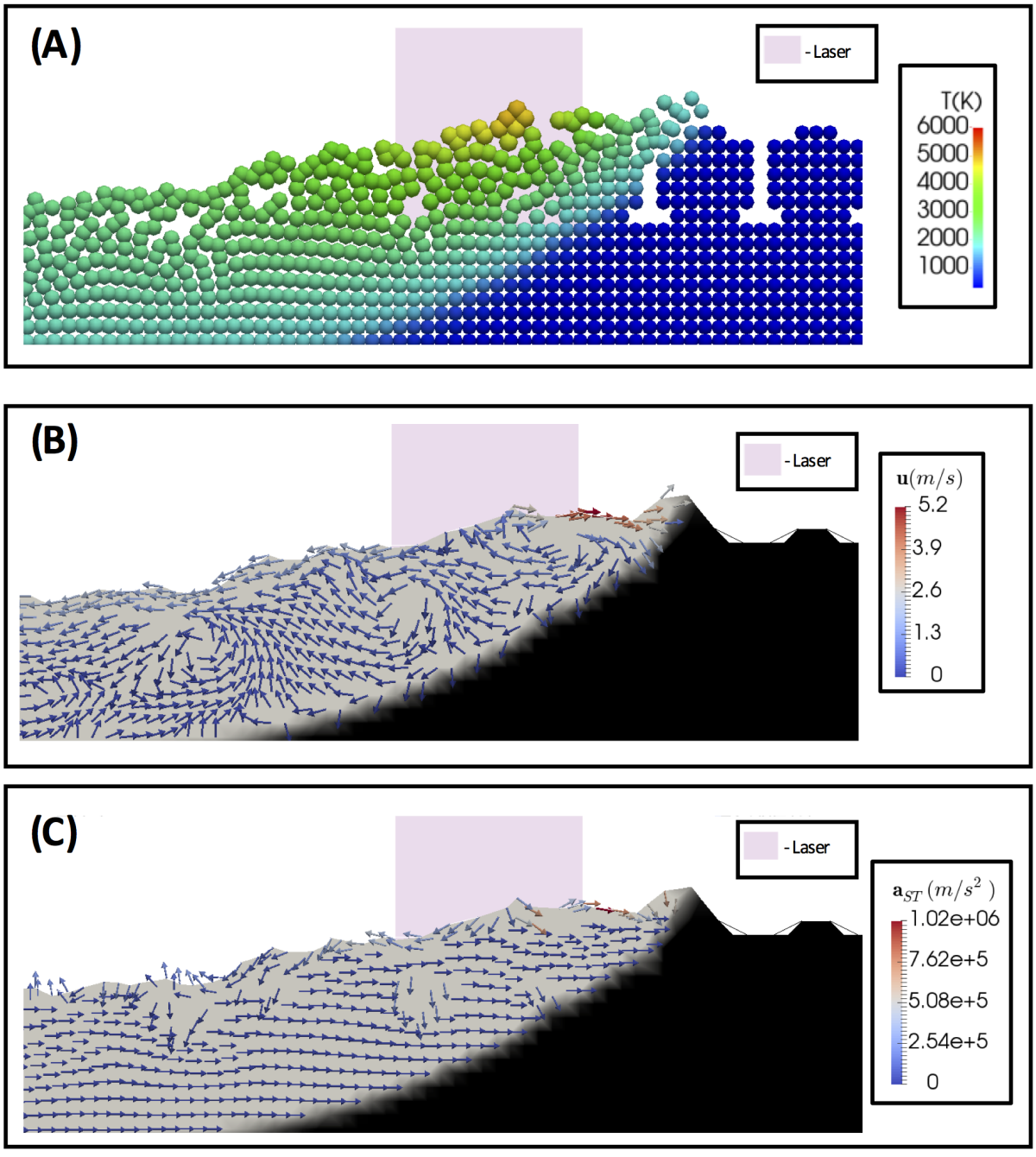

Figure 5.2: Snapshots temperature, velocity, and surface tension acceleration field at $t = 0.24ms$.

Due to the Lagrangian nature of the SPH method its possible to track the motion of specific sections of the particle bed over the process. The motion of a few powder particles was tracked during the lasering process. The results are shown below in Figure 5.3. The

tracked particles are colored red. As it can be seen the powder mass is sheared over the newly formed tracked. The shearing results from the strong Marangoni convection force being a surface phenomena. The top fluid layer is strongly accelerated while the low viscosity of the melt fails to accelerate the lower levels of fluid. Some of the powder mass is mixed into the substrate layer with the majority remaining in the new track layer. Most of the mass form a powder particles remains close together although some is ejected further in front of the bulk of particle mass. This information is useful in determining how 2-component powder mixture might mix and distribute during a lasering process. It indicated that strong mixing is not achieved and striated material microstructures are likely to appear.

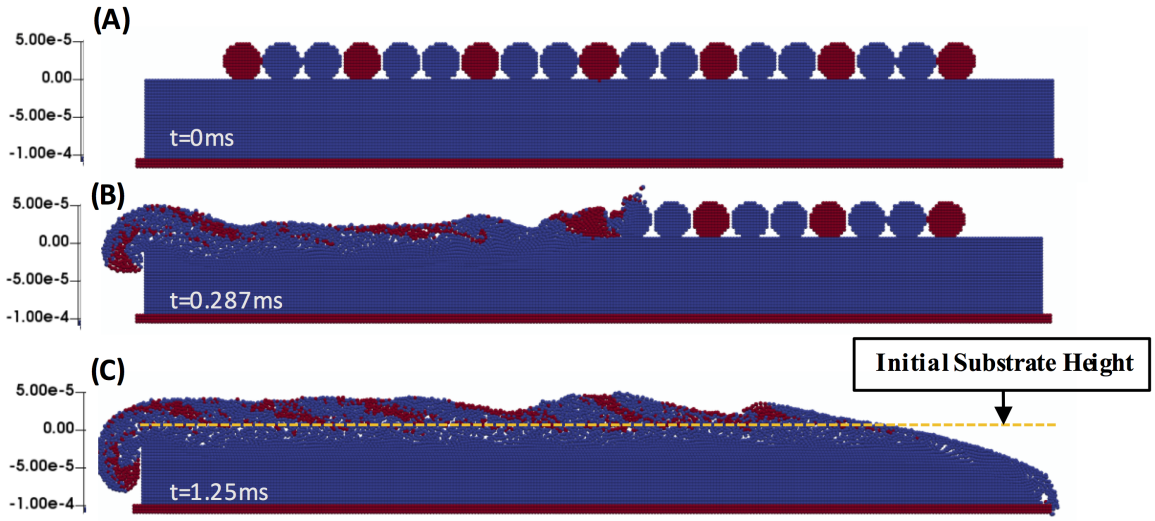

Figure 5.3: Motion of tracer powder particles over the course of a track deposition process.

5.1.1.1 Parameter Studies

Several parameter studies were preformed to show the applicability of the AM-SPH methodology to SLM process optimization. The results from these simulations should be understand to only be valid in the 2D sense. Any extension to real-world 3D simulations is not absolute.

Laser Power Variation A initial parameter study was preformed the effects of varying the laser power. A laser with a beam width of $54\mu m$ laser was scanned over a particle bed composed of $25\mu m$ radius powder particles. Scans with laser powers of $50W$, $100W$, $150W$, *and* $200W$ were preformed. The powder bed geometry was the same as the previous experiment. Snapshots of the particle bed state over the course of the

scan for every power level are given in Appendix B.0.1. For succinctness only the particle bed state at $t = 0.26ms$, mid-lasering , and $t = 1.25ms$, fully resolidified bed, for all the laser powers are presented below in Figure 5.4 and Figure 5.5respectively.

The qualitative effects of the varying laser power on the melt pool state mid-lasering, Figure5.4, are quite pronounced. At $50W$, the laser is incapable of fully melting the powder bed and penetrating into the substrate layer. The melt pool is driven by direct heating under the laser beam and is minimal in size. At $100W$, the laser is capable of fully melting the deposited particles as well as penetrating into the previous substrate layer. The Marangoni convection is significant enough to propagate the melt pool in advance of the laser beam melting oncoming particles. The melt pool motion is relatively calm and smooth. At $150W$, significant penetration into the previous substrate region is achieved. The melt pool is larger in size and protrudes well in advance of the oncoming laser beam. The higher laser powers, result in higher melt-surface temperatures and greater Marangoni-forces. These forces manifest themselves in a more volatile melt surface profile then the $100W$case and significant material ejection out of the front and rear of the melt pool. Finally at $200W$, extreme laser heating results in extreme temperature gradients and a highly volatile melt motion. The extreme Marangoni convection ejects fluid out of the front of the advancing lasers and leads to a highly unstable melt surface.

Qualitatively its clear that using a lower laser power results in a smoother melt-profile. Its rationalized that higher laser powers, the melt pool is both larger and more volatile. The volatility increases the chance of melt-trail break up and the formation of humps. The melt-pool size determines the rate of cooling of the melt-surface. Smaller melt-pools cool much quicker, as they have significantly less thermal mass, reducing the amount of time available for surface tension forces to neck the melt tail forming humps. Khariallah et al. came to the same conclusion in their work noting that “less heat content” gave the surface tension forces less time to break up the flow because solidification occurred faster[38]. Its argued that using the lowest laser power cable of producing an acceptable depth of penetration is preferred.

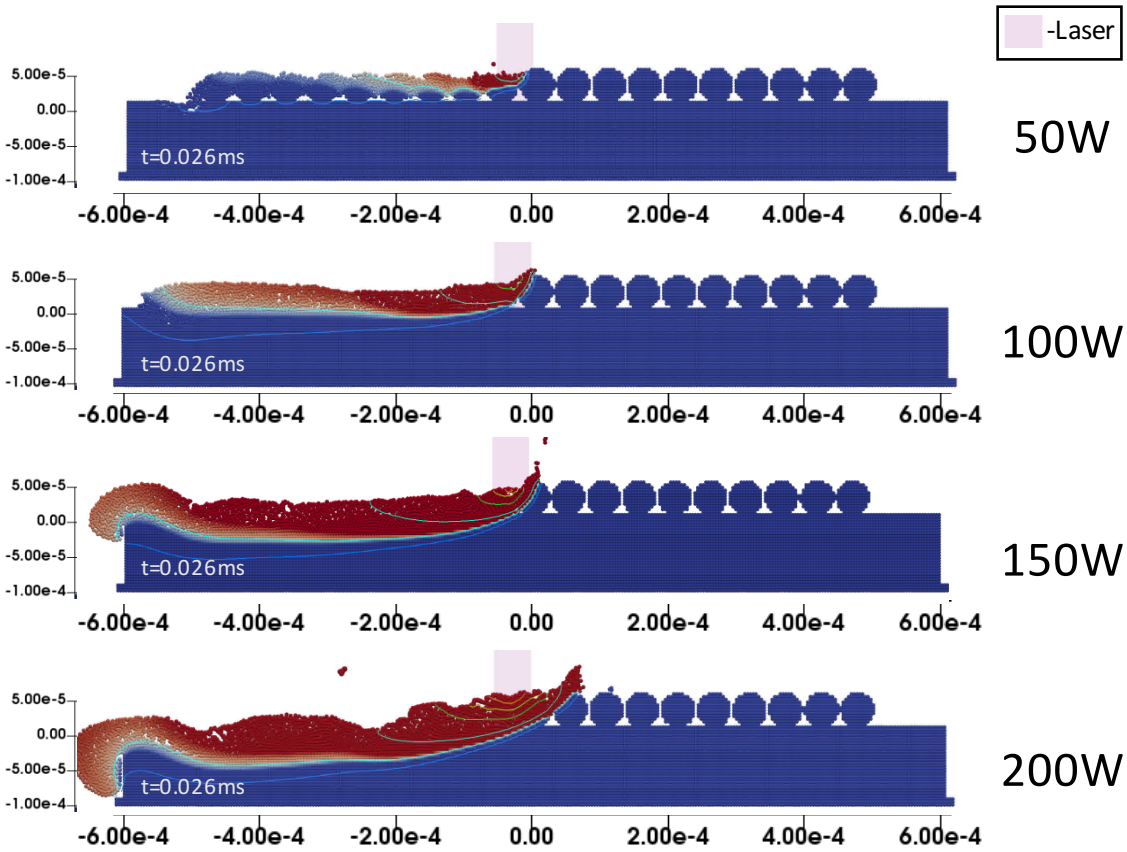

Figure 5.4: Snapshots of the material state and temperature contours for varying laser powers at $t = 0.26ms$.

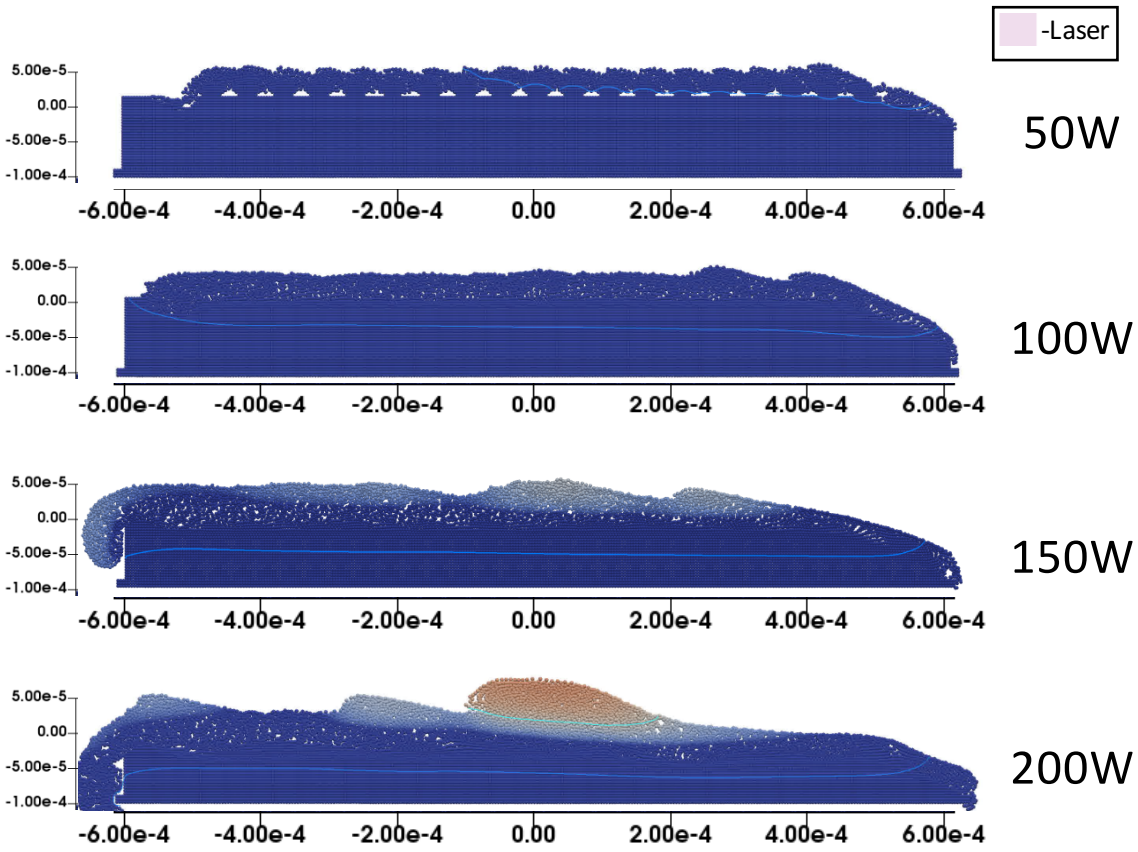

Figure 5.5: Snapshots of the material state and temperature contours for varying laser powers at $t = 1.25ms$.

Quantitatively the varying laser powers can be compared on a number of performance metrics specific to the SLM process: (1) penetration into the substrate layer, (2) max-height variation of the deposited track profile, (3) rate of solidification of the top layer of the melt pool, (4) maximum temperature of the melt pool, (5) maximum velocity of the melt pool. Penetration is important to ensure sufficient bonding of the newly deposited track with the substrate layer. Smoothness is desired to keep track deposition even and ensure z-height variation across the part is minimized. High-rates of cooling as well as steep temperature gradients are sources of thermally induced residual stresses and micro-cracking and should be minimized. The maximum temperature of the melt pool should be kept below the vaporization of the material. These metrics were calculated for the varying laser power and are tabulated below in Table .5.3 Metrics (1) and (3-5) were calculated at $t = 0.26ms$, mid-lasering. Penetration was measured from the initial surface of the substrate layer. The max-height variation was taken along the interior of the sample,

from $x = -0.3mm$ to $x = +0.33mm$ to minimize edge effects.

Metric	50W	100W	150W	200W
Subtrate Penetration	$0\mu m$	$6\mu m$	$30\mu m$	$42\mu m$
Track Max-Height Variaton		$15\mu m$	$25\mu m$	$72\mu m$
Rate of Solidificaton		$0.09ms$	$0.153ms$	$0.18ms$
Max Temperature	$2700K$	$3833K$	$4600K$	$6100K$
Max Velocity	$1.2\frac{m}{s}$	$2.8\frac{m}{s}$	$3.5\frac{m}{s}$	$6.0\frac{m}{s}$

Table 5.3: Results for laser power parameter study.

As expected the maximum fluid velocity corresponds with the maximum fluid temperature(greater temperature gradients results in larger Marangoni forces) and the melt penetration with inverse of the rate of solidification(the larger the melt pool, the longer it takes to cool). Interestingly however, the four do not correspond together. The maximum temp of the $150W$ case is much closer to the maximum temperature of the $100W$case then that of the$200W$ case, however the penetration of the $150W$case is closer to the penetration of the $200W$ case then the $100W$ case. Counter intuitively, this implies that higher maximum melt fluid surface temperatures don't necessarily correspond to greater melt penetration. These results indicate a that melt phenomena can't be easily predicted and need to be further investigated in-detail using a 3D code.

Finally, the maximum melt temperatures for the $150W$ and $200W$ case exceed the vaporization temperature of steel and indicate the need for a vaporiation framework within the AM-SPH method. In addition, the rate of solidification of the melt surface in the $100W$ laser is significantly lower then the $150 - 200W$ cases. This was qualitatively mentioned above but is confirmed by the data here.

Particle Radius Variation A second parameter study was preformed varying the particle diameters. A $150W$ laser with a 2-σ width of $54\mu m$ was scanned across a 2D particle bed. Scans with particle radius of $25\mu m$, $15\mu m$, $30\mu m$, and a mix of $30\mu m$ and $15\mu m$ were preformed. Mixed particle radii powder beds are commonly used in industry to obtain high packing ratios. Snapshots of the particle bed state over the course of the scan for every power level are given in Appendix B.0.2. For succinctness only the particle bed state at $t = 0.26ms$, mid-lasering, and $t = 1.25ms$, fully resolidified bed, are presented below in Figure 5.6 and Figure 5.7respectively.

Qualitatively, several conclusions can be drawn. First, the smaller the powder particles, the less influence they have on the melt pool motion. The small mass of the $r_p = 15\mu m$ particles allows them to be fully melted well in advance of the oncoming laser beam. This results in a smoother melt pool motion that is less disrupted by the particles masses. However this does not necessarily translate into a smoother track profile. The smoothest profile corresponds to the largest powder radius. Its not clear to the author why this is the case.

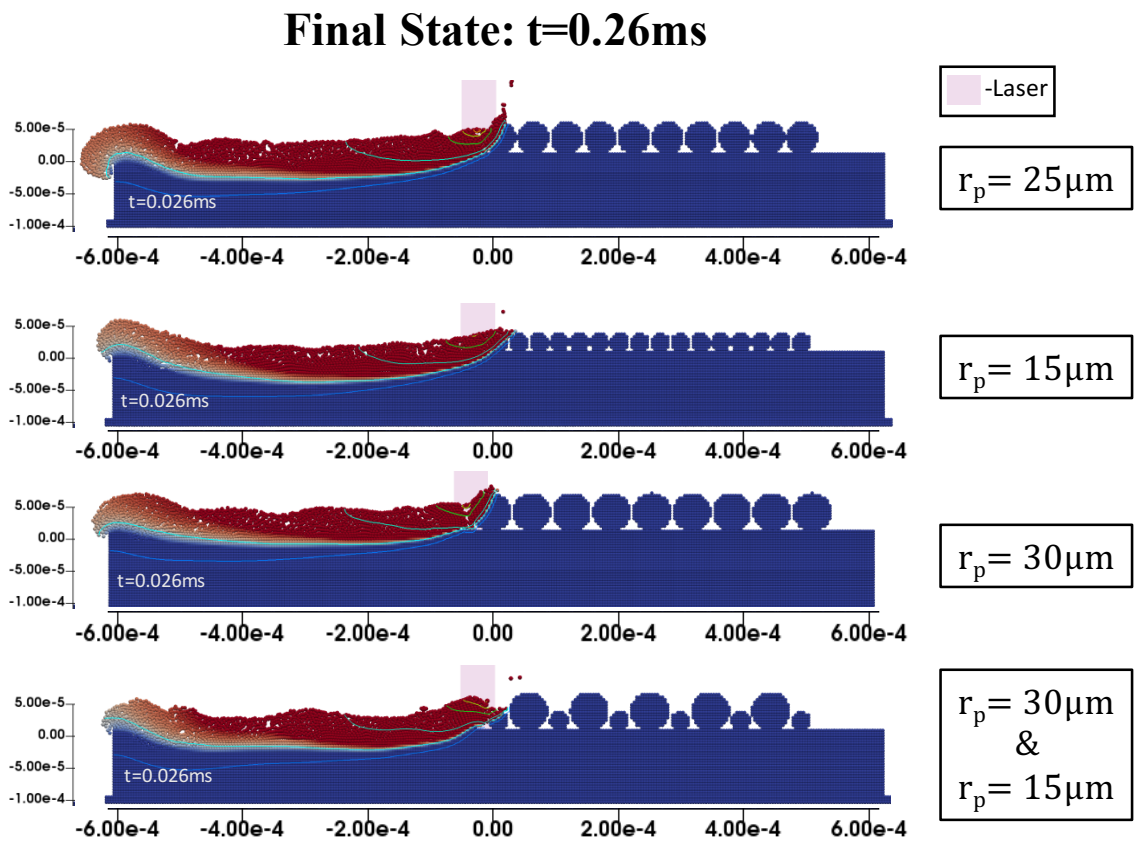

Figure 5.6: Snapshots of the material state and temperature contours for varying particle bed powder radii at $t = 0.26ms$.

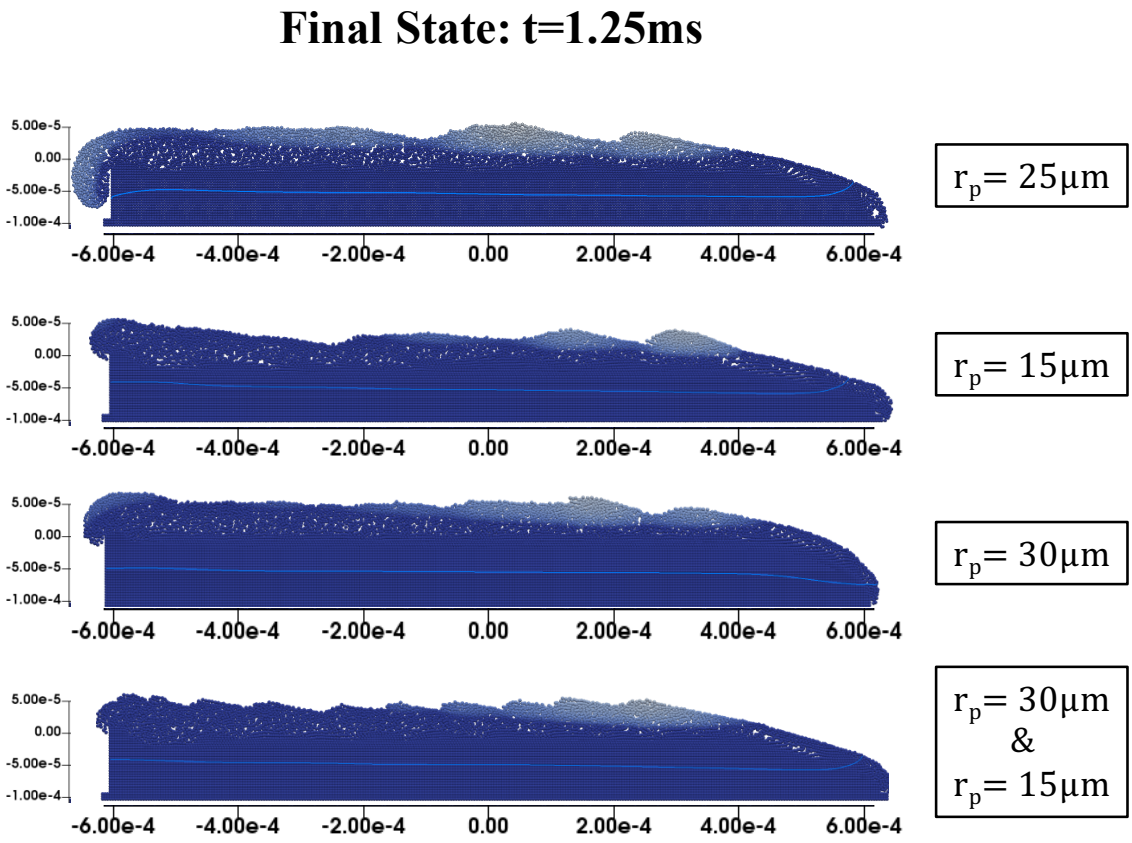

Figure 5.7: Snapshots of the material state and temperature contours for varying laser powers at $t = 1.25ms$.

Laser Width Variation A third parameter study was preformed varying laser beam width. A $150W$ laser beam with varying widths of $w_{2\sigma} = 27\mu m,\ 54\mu m,\ and\ 81\mu m$ was scanned for a 2D particle bed with powder radius of $r_p = 25\mu m$. The particle bed state at $t = 0.26ms$, mid-lasering, and $t = 1.25ms$, full resolidified bed, are presented below in Figure 5.8 and Figure 5.9respectively.

Qualitatively, several conclusions can be drawn. Its clear that smaller the laser beam the more violent and the larger the melt pool motion. This is the result of higher localized heating and hence the higher localized Marangoni convection. The smoothest final melt profile corresponds to the largest beam width. This intuitively makes sense as the temperature gradients are minimized and hence the Marangoni convection minimized as well. This minimizes the overall motion of the melt pool and the chance for the surface to break up and roughen on cooling. In addition the melt pool is significantly smaller for the $w_{2\sigma} = 81\mu m$. A smaller melt pool minimizes the chance of the melt pool to break up and form a rough surface. These results indicate using a larger laser width is preferable.

However, the larger the laser width the lower the resolution from the build. Its believed that a smaller laser spot size in combination with preheating of the powder bed can minimize the undesirable temperature gradients seen with the $w_{2\sigma} = 27\mu m$ experiment while maintaining a high resolution.

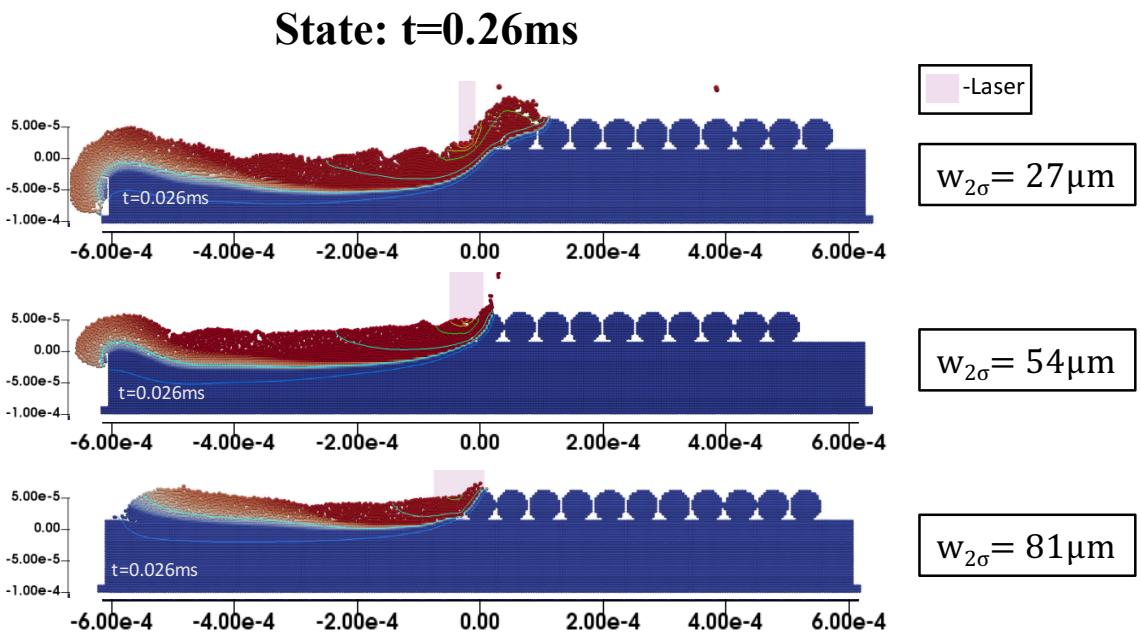

Figure 5.8: Snapshots of the material state and temperature contours for varying particle bed powder radii at $t = 0.26ms$.

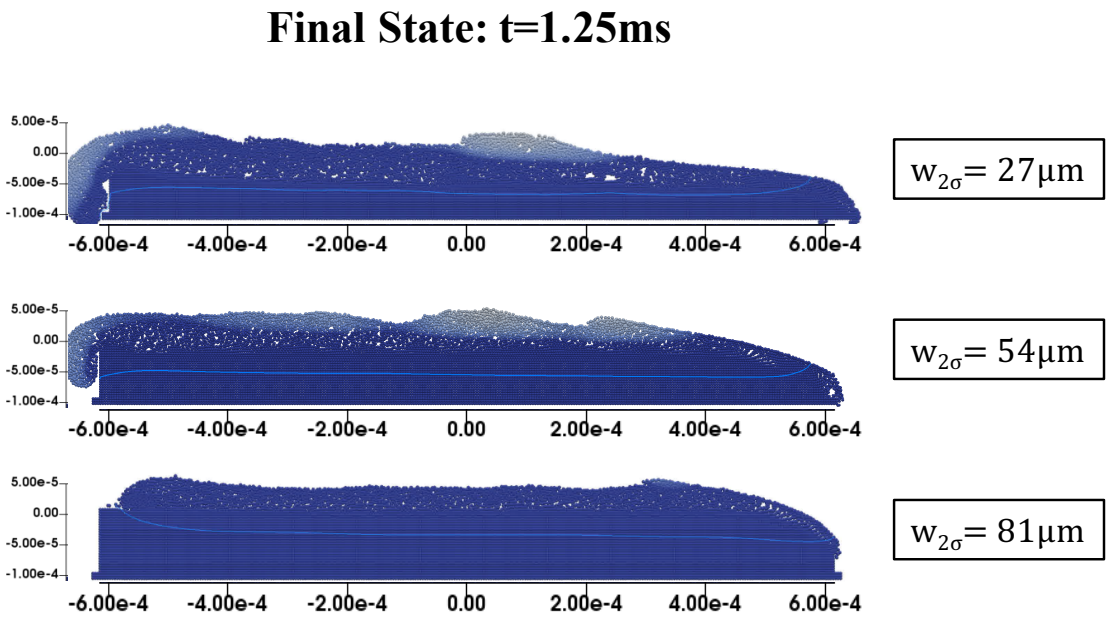

Figure 5.9: Snapshots of the material state and temperature contours for varying laser powers at $t = 1.25ms$.

Thermal Conduction Variation Study As mentioned previously, a major benefit of the Lagrangian nature of the SPH method, is the ability to easily simulate multi-phase problems. Boundary tracking is implicitly handled by the the numerical schemes as each SPH particles is associated with a specific phase. To demonstrate the capabilities of this method, an experiment based around the the proposed capability of the SLM to functionally dope a material was developed. In this study, every third particle was given twice conductivity of the other powder particles and substrate. The results of the track laser melting of the doped particle bed along with a control particle bed are given in Figure 5.10. A $100W$ laser with a width of $w_{2\sigma} = 54\mu m$ was used. The powder radii was $25\mu m$.

The distribution of the thermally enhanced particles is apparent in the initial configuration snapshot. From the final time snapshot its apparent that the effect of the enhanced thermal conductivity particles is minimal. The only differences between the solidified state of the doped bed and the control appears to be the development of periodic humps on the final surface profile. These humps are directly the result of the higher thermal conductivity particles. As seen in the mid-lasering snapshots, when a higher thermally conductive particle is melted, it leads to the development of a shorter-deeper melt pool. This makes sense as the higher thermal conductivity would transfer heat deeper into the material, deepening the melt pool, while increasing the rate of solidification of

the laser-pool surface, shortening the melt pool. These periodic periods of thermal pool shortening correspond to the location of the humps on the final surface profile.

A second interesting feature of this simulation is that the thermally conductive material becomes stratified in the track layer. This stratification could lead to an anisotropic thermally conductivity through the track and alter the macro-scale properties of the part. Discovering how multi-phase particle beds melt and coalesce could be a prime use for the AM-SPH method.

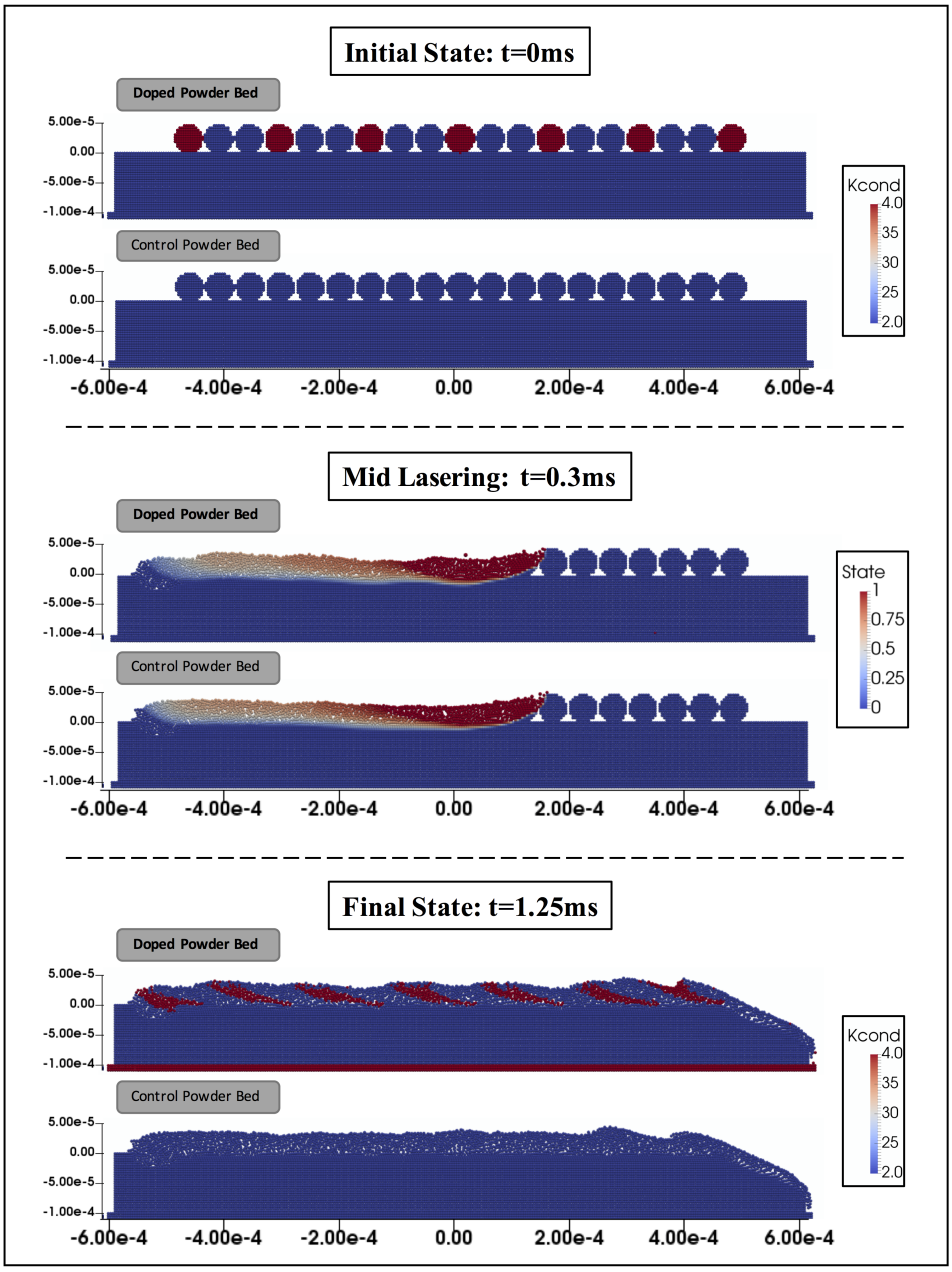

Figure 5.10: Plots of the state and thermal conductivity over time for both a doped particle bed with enhanced thermal conductivity and a control powder bed.

5.1.2 Laser Melting of a 3D Particle Bed

A 3D simulation of the laser melting of a shortened particle bed track was preformed. The material properties were the same as the spot laser validation test, Section 4.1. A regular distribution of particles was used. In actuality, the spacing would be more irregular due to the 3D nature of the particle bed The simulation parameters are given in Table 5.2. In order to prevent the overheating of ejected SPH particles, if an ejected SPH particles temperature reached $6000K$ it was removed from the simulation. A no-conduction/convection flux boundary condition was imposed on the top surface. The bottom surface of the substrate had a dirchlet temperature condition of $T = 293K$ that was implemented using a layer of boundary particles. The substrate layer was chosen to be thick-enough such that the effect of the boundary condition on temperature field was minimized. A laser with a power of $150W$ and a width of $w_{2\sigma} = 54\mu m$ was scanned over the particle bed. The scan speed was $2m/s$ and the powder particle radii $25\mu m$. The scale of the powder bed was only 6 particles, too small to gather quantitative data from, however large enough to confirm the capability of the AM-SPH method to simulate 3D problems.

Plots of the powder bed state over time are displayed in Figure 5.11. The 3D nature of the particle bed melt pool is apparent. Marangoni convection not only disturbs particles along the track direction but also moves the fluid laterally as well, evenly coating the melt surface. Contrary to the 2D simulations, the melt pool doesn't develop in advance of the laser beam. Melting of oncoming material is primarily from laser heating. The rate conduction is more extreme in the 3D model as compared to the 2D model as the meltpool is distrubuted over a wider area preventing the development of an advancing weldpool. This also reduced length of the weldpool tail. The higher rates of conduction may become less aparent with the simulation of a fully filled particled bed.

Overall the simulation is stable and appears physically accurate and capable of simulating 3D particled bed problems. However again the temperature of the surface SPH particles directly under the laser sources exceeded the vaporization temperature of the steel material. This indicates that a vaporization model with resulting recoil pressures needs be added to the model.

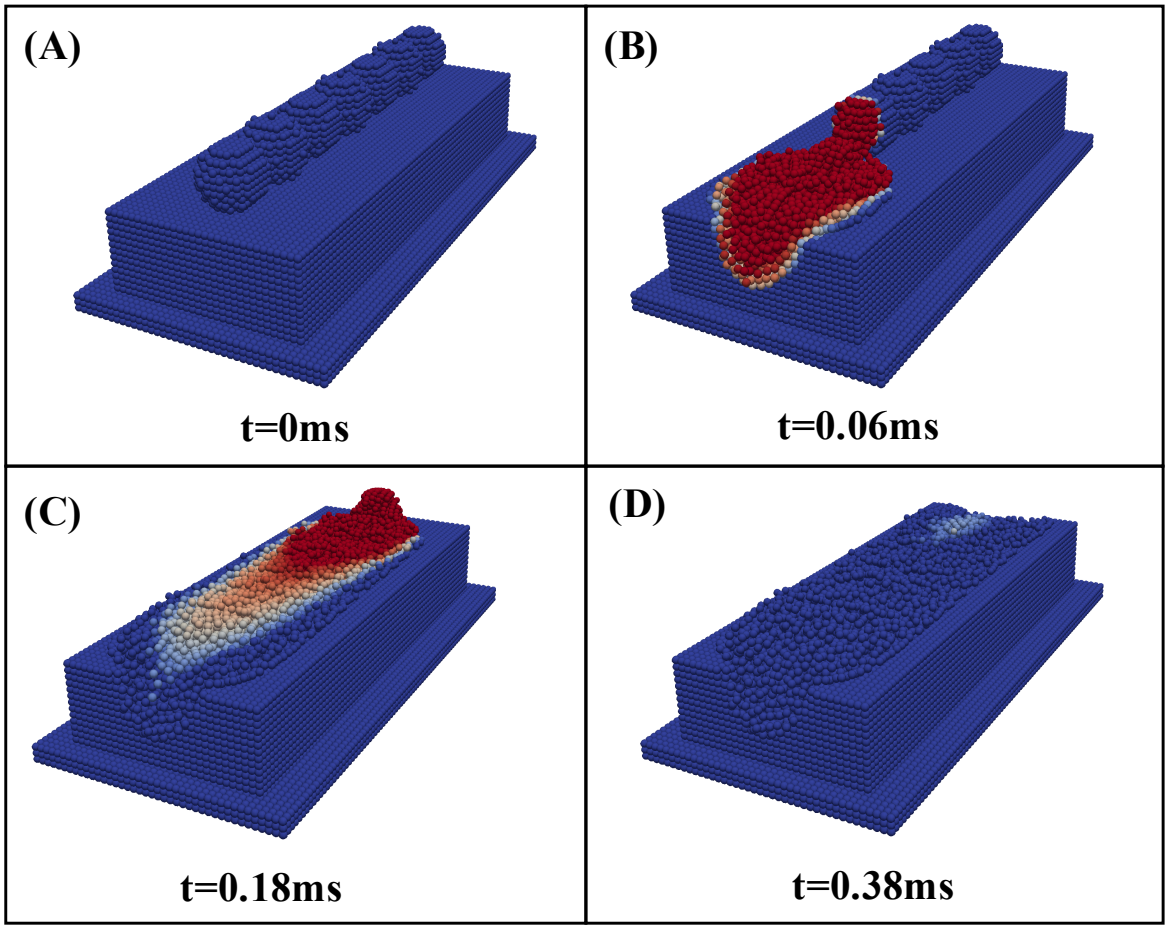

Figure 5.11: Snapshots of the material state over the length of the scan process for a 3D powder bed with a $150W$ laser and $25\mu m$ radius powder particles.

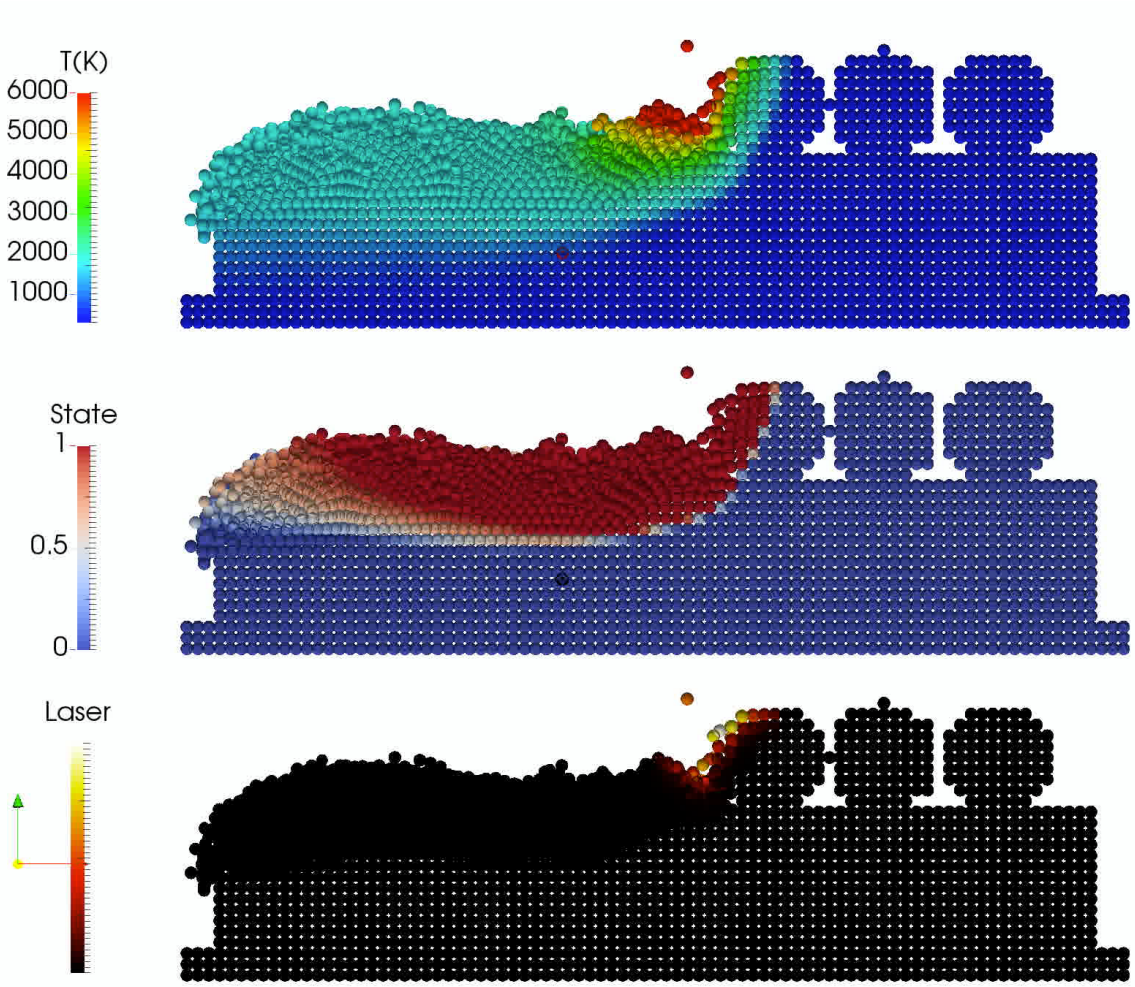

Figure 5.12: Vertical slices of the temperature, state, and laser field mid-lasering for the 3D powder bed experiment.

Chapter 6

Conclusion

In this work, an SPH methodology capable of simulating the thermal-mechanical-material fields in Additive Manufacturing processes was developed, validated, and used to conduct numerical experiments on the laser melting of a microscale metallic powder bed. Additive Manufacturing is set to revolutionize the manufacturing sector by allowing for the production of 3D, net-shape, customizable components in a fraction of the time and at a fraction of the time of traditional manufacturing methods. Numerical simulation, validated by physical experiments, is an extremely useful tool for optimizing and understanding existing AM technologies as well as developing novel ones.

In this work the applicability of the Smooth Particle Hydrodynamics Method, a Lagrangian mesh-free numerical scheme that is traditionally used for simulating large-scale fluids mechanics, to simulating AM processes was investigated. A novel AM-SPH methodology was developed, combining and adapting discretizations from disparate SPH fields as well developing necessary novel formulations, to be able to simulate AM processes using the SPH methodology for the first time. In particular an isothermally-incompressible formulation was developed to simulate the thermal-volumetric expansion of incompressible fluids undergoing extreme temperature changes. The AM-SPH methodology was validated using a spot-laser weld pool experiment. The results were promising with the method capable of closely replicating the melt pool dimension obtained from physical experimentation. However it was determined that a more efficient implementation of the code capable of higher resolution, longer time scale simulations was required to fully validate the method. In addition the novel isothermally-incompressible SPH formulation developed in this work was shown to be capable of accurately simulating thermal-volumetric expansion and contraction but incapable of simulating buoyancy flows.

To show the applicability of the AM-SPH methodology to simulating a real-world AM process, the track scale simulation of the Selective Laser Melting of a metallic Particle Bed was preformed. Due to the high computational expense of the current implementation of the AM-SPH methodology, only high resolution, full scale simulations in 2D were possible. Parameter studies were preformed, the physical phenomena of the process examined, and produced. They were only limited to 2D and hence not necessarily reflective of the real world process, however they confirmed the findings in literature([38]) that the dominant driving force of melt pool motion is Marangoni convection. A small scale simulation of the melting of a collection of 3D powder particles was also preformed to show the applicability of the method to 3D. The method was found to be capable of the simulating the 3D process.

The viability of SPH for simulating AM process was one of the overall goals of this work. In general, the method was found to be adequate and applicable to modeling AM process. The SPH method was hypothesized to be naturally suited for the simulation of AM process, with SLM in particular, because unlike mesh based method, it inherently tracks free-surfaces as well as boundary interfaces. This was found to be true as the solidification front and free-surface profile of the melt-pool were trivial to simulate with the SPH method. In addition, the lasering, melting, and flow of multi-phase particle beds was easy to simulate within the SPH method as well. However, it was noted that further

development needs to be preformed on the thermal and surface tension SPH discretizations to render them consistent on the free surface before the method can be used to its full potential

The efficiency of the SPH method as compared to traditional numerical methods(e.g. FEM, FDM) that have been applied to simulating AM process however is unclear. The current implementation of the code was inefficient, and serial, written more for research flexibility then pure speed making comparison with the few sources of literature that give simulation times impossible. However, one major setback noted by this author of the SPH method when simulating the SLM process was the need for smaller then expected time steps. At issue is the weakly-compressible formulation used in SPH. The method requires a stiff equation of state, high sound speed, to ensure the material remains incompressible and the simulation discretization remains stable with SPH particles that remain equally spaced and do not collapse on each other. The sound speed is typically set to be 10 times the max velocity experienced in the simulation and usually a Courant number between $0.15 - 0.25$ is necessary to achieve stability. For the lasering simulations these conditions were found to be inadequate. A courant condition of $C_0 \leq 0.05$ was found to be necessary for stability and sometimes a sound speed of up to 50 times the maximum velocity required. It was believed that the limiting factor in these cases was the massive forces placed on the SPH particles by the Marangoni surface tension. These significant forces compromise the incompressibility constraint and can lead to an unstable collapse of SPH particles upon one another. High fluid stiffness and hence small time steps are necessary to mitigate these effects. No CFL condition for Marangoni convection was found in literature but based on the size of the Marangoni forces, its believed to be more restrictive then the other conditions used in the model. Such restrictions may make the simulations of the SLM process out of reach of the AM-SPH method. Further work needs to be performed to confirm this.

However, the applicability of SPH to lower-force AM process is still viable. For example, the plastic 3D printing process. The simplicity of the SPH method in handling a wide range of geometries and fluid motions certainly sets it apart from the continuum method of FEM and FVM and its possible that other AM applications are more suited to it use. At the moment, its unlearn if SPH will be able compete with traditional numerical methods in simulating AM applications, however this preliminary work certainly shows the promise of the method and that it warrants future investigation.

Future Work In order to fully validate and utilize the developed AM-SPH methodology, its needs to be parallelized and optimized. Trivial parallelization is a main benefit of the SPH methodology and necessary for its use in industry. Optimization can be implemented through more efficient coding structures and routines. After an efficient code is implemented, the SLM process can be properly investigated in 3D and the AM-SPH method validated. As noted previously, SLM is truly a 3D process and many of the processes phenomena that of our interest to researchers(void entrapment, particle ejection, partial melting of powders) can only be investigated with a 3D model. Finally it would

be desirable to link the SPH methodology with the Discrete Element Method and a continuum method to reduce the computational cost. The continuum method could be used to simulate the substrate layer with the DEM used to capture the heating and motion of unmelted powder particles to reduce computational costs.

Bibliography

[1] Standard Terminology for Additive Manufacturing Technologies, (Withdrawn 2015). Technical Report ASTM F2792-12a, ASTM International, West Conshohocken, PA, 2012.

[2] S Adami, XY Hu, and NA Adams. A new surface-tension formulation for multi-phase SPH using a reproducing divergence approximation. *Journal of Computational Physics*, 229(13):5011–5021, 2010.

[3] AW Alshaer, BD Rogers, and L Li. Smoothed Particle Hydrodynamics (SPH) modelling of transient heat transfer in pulsed laser ablation of Al and associated free-surface problems. *Computational Materials Science*, 127:161–179, 2017.

[4] M. Antuono, A. Colagrossi, and S. Marrone. Numerical diffusive terms in weakly-compressible SPH schemes. *Computer Physics Communications*, 183(12):2570 – 2580, 2012.

[5] J. Bonet and T.-S.L. Lok. Variational and momentum preservation aspects of Smooth Particle Hydrodynamic formulations. *Computer Methods in Applied Mechanics and Engineering*, 180(1):97 – 115, 1999.

[6] JU Brackbill, Douglas B Kothe, and Charles Zemach. A continuum method for modeling surface tension. *Journal of computational physics*, 100(2):335–354, 1992.

[7] Milan Brandt, Martin Leary, Shou Jin Sun, et al. The Effect of Manufacturing Defects on the Fatigue Behaviour of Ti-6Al-4V Specimens Fabricated Using Selective Laser Melting. In *11th International Fatigue Congress*, volume 891 of *Advanced Materials Research*, pages 1519–1524. Trans Tech Publications, 5 2014.

[8] J.L. Cercos-Pita, R.A. Dalrymple, and A. Herault. Diffusive terms for the conservation of mass equation in SPH. *Applied Mathematical Modelling*, 40(19):8722 – 8736, 2016.

[9] Paul W Cleary and Joseph J Monaghan. Conduction Modelling Using Smoothed Particle Hydrodynamics. *Journal of Computational Physics*, 148(1):227 – 264, 1999.

[10] PW Cleary, J Ha, M Prakash, and T Nguyen. 3D SPH flow predictions and validation for high pressure die casting of automotive components. *Applied Mathematical Modelling*, 30(11):1406–1427, 2006.

[11] Andrea Colagrossi, Matteo Antuono, and David Le Touzé. Theoretical considerations on the free-surface role in the smoothed-particle-hydrodynamics model. *Physical Review E*, 79(5):056701, 2009.

[12] Andrea Colagrossi and Maurizio Landrini. Numerical simulation of interfacial flows by smoothed particle hydrodynamics. *Journal of computational physics*, 191(2):448–475, 2003.

[13] Andrea Colagrossi, Antonio Souto-Iglesias, Matteo Antuono, and Salvatore Marrone. Smoothed-particle-hydrodynamics modeling of dissipation mechanisms in gravity waves. *Physical Review E*, 87(2):023302, 2013.

[14] Sharen J Cummins and Murray Rudman. An SPH projection method. *Journal of computational physics*, 152(2):584–607, 1999.

[15] Stephen H Davis. *Theory of solidification*. Cambridge University Press, 2001.

[16] Paulo Hemerson de Moraes, Sergio Olate, Mario Cantín, et al. Anatomical reproducibility through 3D printing in cranio-maxillo-facial defects. *Int. j. morphol*, 33(3):826–830, 2015.

[17] Walter Dehnen and Hossam Aly. Improving convergence in smoothed particle hydrodynamics simulations without pairing instability. *Monthly Notices of the Royal Astronomical Society*, 425(2):1068–1082, 2012.

[18] Gary A Dilts. Moving-least-squares-particle hydrodynamics?I. Consistency and stability. *International Journal for Numerical Methods in Engineering*, 44(8):1115–1155, 1999.

[19] Gary A Dilts. Moving least-squares particle hydrodynamics II: conservation and boundaries. *International Journal for Numerical Methods in Engineering*, 48(10):1503–1524, 2000.

[20] Tobias Dubberstein, Hans-Peter Heller, Olga Fabrichnaya, Christos G Aneziris, and Olena Volkova. Determination of Viscosity for Liquid Fe–Cr–Mn–Ni Alloys. *steel research international*, 87(8):1024–1029, 2016.

[21] ENGINEERING.com. Background.

[22] R Fatehi, M Fayazbakhsh, and MT Manzari. On discretization of second-order derivatives in smoothed particle hydrodynamics. In *Proceedings of World Academy of Science, Engineering and Technology*, volume 30, pages 243–246, 2008.

[23] R. Fatehi and M. T. Manzari. A remedy for numerical oscillations in weakly compressible smoothed particle hydrodynamics. *International Journal for Numerical Methods in Fluids*, 67(9):1100–1114, 2011.

[24] D Fernandez-Gutierrez, A Souto-Iglesias, and TI Zohdi. A hybrid Lagrangian Voronoi–SPH scheme. *Computational Particle Mechanics*, pages 1–10, 2017.

[25] Rishi Ganeriwala and Tarek I. Zohdi. Multiphysics Modeling and Simulation of Selective Laser Sintering Manufacturing Processes. *Procedia CIRP*, 14:299 – 304, 2014.

[26] Ian Gibson, David W Rosen, Brent Stucker, et al. *Additive manufacturing technologies*, volume 238. Springer, 2010.

[27] Robert A Gingold and Joseph J Monaghan. Smoothed particle hydrodynamics: theory and application to non-spherical stars. *Monthly notices of the royal astronomical society*, 181(3):375–389, 1977.

[28] N. Grenier, M. Antuono, A. Colagrossi, D. Le Touzac, and B. Alessandrini. An Hamiltonian interface SPH formulation for multi-fluid and free surface flows. *Journal of Computational Physics*, 228(22):8380 – 8393, 2009.

[29] D D Gu, W Meiners, K Wissenbach, and R Poprawe. Laser additive manufacturing of metallic components: materials, processes and mechanisms. *International Materials Reviews*, 57(3):133–164, 2012.

[30] AV Gusarov and I Smurov. Modeling the interaction of laser radiation with powder bed at selective laser melting. *Physics Procedia*, 5:381–394, 2010.

[31] HT Hashemi and CM Sliepcevich. A numerical method for solving two-dimensional problems of heat conduction with change of phase. In *Chem. Eng. Prog. Symp. Series*, volume 63, pages 34–41, 1967.

[32] X He, P W Fuerschbach, and T DebRoy. Heat transfer and fluid flow during laser spot welding of 304 stainless steel. *Journal of Physics D: Applied Physics*, 36(12):1388, 2003.

[33] NE Hodge, RM Ferencz, and RM Vignes. Experimental comparison of residual stresses for a thermomechanical model for the simulation of selective laser melting. *Additive Manufacturing*, 12:159–168, 2016.

[34] https://manufacturing.llnl.gov/additive-manufacturing/metal-additive manufacturing. Metal Additive Manufacturing.

[35] H. Hu, F. Fetzer, P. Berger, and P. Eberhard. Simulation of laser welding using advanced particle methods. *GAMM Mitteilungen*, 39(2):149–169, 2016. cited By 0.

[36] Haoyue Hu and Peter Eberhard. Thermomechanically coupled conduction mode laser welding simulations using smoothed particle hydrodynamics. *Computational Particle Mechanics*, pages 1–14, 2016.

[37] S.A. Khairallah and A.T. Anderson. Mesoscopic Simulation Model of Selective Laser Melting of Stainless Steel Powder. *Journal of Materials Processing Technology*, 2014.

[38] Saad A Khairallah, Andrew T Anderson, Alexander Rubenchik, and Wayne E King. Laser powder-bed fusion additive manufacturing: Physics of complex melt flow and formation mechanisms of pores, spatter, and denudation zones. *Acta Materialia*, 108:36–45, 2016.

[39] Wayne E King, Holly D Barth, Victor M Castillo, et al. Observation of keyhole-mode laser melting in laser powder-bed fusion additive manufacturing. *Journal of Materials Processing Technology*, 214(12):2915–2925, 2014.

[40] WE King, AT Anderson, RM Ferencz, et al. Laser powder bed fusion additive manufacturing of metals; physics, computational, and materials challenges. *Applied Physics Reviews*, 2(4):041304, 2015.

[41] Carolin Körner, Elham Attar, and Peter Heinl. Mesoscopic simulation of selective beam melting processes. *Journal of Materials Processing Technology*, 211(6):978–987, 2011.

[42] YS Lee and W Zhang. Mesoscopic simulation of heat transfer and fluid flow in laser powder bed additive manufacturing. In *International Solid Free Form Fabrication Symposium, Austin*, pages 1154–1165, 2015.

[43] Agnes Leroy, Damien Violeau, Martin Ferrand, and Antoine Joly. Buoyancy modelling with incompressible SPH for laminar and turbulent flows. *International Journal for Numerical Methods in Fluids*, 78(8):455–474, 2015.

[44] Gary K Lewis and Eric Schlienger. Practical considerations and capabilities for laser assisted direct metal deposition. *Materials and Design*, 21(4):417 – 423, 2000.

[45] M.B. Liu I& G.R. Liu. Smoothed Particle Hydrodynamics (SPH): an Overview and Recent Devlopments. *Archives of computational methods in engineering*, 17.1(25-76), 2010.

[46] Salvatore Marrone, Andrea Colagrossi, Matteo Antuono, G Colicchio, and Giorgio Graziani. An accurate SPH modeling of viscous flows around bodies at low and moderate Reynolds numbers. *Journal of Computational Physics*, 245:456–475, 2013.

[47] Salvatore Marrone, Andrea Colagrossi, Andrea Di Mascio, and David Le Touzé. Analysis of free-surface flows through energy considerations: Single-phase versus two-phase modeling. *Phys. Rev. E*, 93:053113, May 2016.

[48] K. C. Mills. *Recommended values of thermophysical properties for selected commercial alloys. [electronic resource].* Cambridge : Woodhead, 2002, 2002.

[49] Diego Molteni and Andrea Colagrossi. A simple procedure to improve the pressure evaluation in hydrodynamic context using the SPH. *Computer Physics Communications*, 180(6):861 – 872, 2009.

[50] J.J Monaghan and R.A Gingold. Shock simulation by the particle method SPH. *Journal of Computational Physics*, 52(2):374 – 389, 1983.

[51] JJ Monaghan, Andrew Kos, and Nader Issa. Fluid motion generated by impact. *Journal of waterway, port, coastal, and ocean engineering*, 129(6):250–259, 2003.

[52] Joe J Monaghan. Simulating free surface flows with SPH. *Journal of computational physics*, 110(2):399–406, 1994.

[53] Joe J Monaghan. Smoothed particle hydrodynamics. *Reports on progress in physics*, 68(8):1703, 2005.

[54] Joseph P Morris. Simulating surface tension with smoothed particle hydrodynamics. *International journal for numerical methods in fluids*, 33(3):333–353, 2000.

[55] Joseph P Morris, Patrick J Fox, and Yi Zhu. Modeling low Reynolds number incompressible flows using SPH. *Journal of computational physics*, 136(1):214–226, 1997.

[56] A Munjiza and KRF Andrews. NBS contact detection algorithm for bodies of similar size. *International Journal for Numerical Methods in Engineering*, 43(1):131–149, 1998.

[57] W. Pitscheneder, T. DebRoy, K. Mundra, and R. Ebner. Role of sulfur and processing variables on the temporal evolution of weld pool geometry in multikilowatt laser beam welding of steels. *Welding J. Supplement*, 75:71–80, 1996.

[58] PW Randles and LD Libersky. Smoothed particle hydrodynamics: some recent improvements and applications. *Computer methods in applied mechanics and engineering*, 139(1-4):375–408, 1996.

[59] PW Randles and LD Libersky. Smoothed particle hydrodynamics: some recent improvements and applications. *Computer methods in applied mechanics and engineering*, 139(1-4):375–408, 1996.

[60] P Sahoo, T DebRoy, and MJ McNallan. Surface tension of binary metal?surface active solute systems under conditions relevant to welding metallurgy. *Metallurgical and Materials Transactions B*, 19(3):483–491, 1988.

[61] Babis Schoinochoritis, Dimitrios Chantzis, and Konstantinos Salonitis. Simulation of metallic powder bed additive manufacturing processes with the finite element method: A critical review. *Proceedings of the Institution of Mechanical Engineers, Part B: Journal of Engineering Manufacture*, 231(1):96–117, 2017.

[62] Donald Shepard. A two-dimensional interpolation function for irregularly-spaced data. In *Proceedings of the 1968 23rd ACM national conference*, pages 517–524. ACM, 1968.

[63] RN Singh, S Arafin, and AK George. Temperature-dependent thermo-elastic properties of s-, p-and d-block liquid metals. *Physica B: Condensed Matter*, 387(1):344–351, 2007.

[64] S Sun, M Brandt, and M Easton. Powder bed fusion processes: an overview. *Laser Additive Manufacturing: Materials, Design, Technologies, and Applications*, page 55, 2016.

[65] K. Szewc, J. Pozorski, and A. Taniasre. Modeling of natural convection with Smoothed Particle Hydrodynamics: Non-Boussinesq formulation. *International Journal of Heat and Mass Transfer*, 54(23):4807 – 4816, 2011.

[66] Mingming Tong and David J Browne. An incompressible multi-phase smoothed particle hydrodynamics (SPH) method for modelling thermocapillary flow. *International Journal of Heat and Mass Transfer*, 73:284–292, 2014.

[67] A. Ghasemi V., B. Firoozabadi, and M. Mahdinia. 2D numerical simulation of density currents using the SPH projection method. *European Journal of Mechanics - B/Fluids*, 38:38 – 46, 2013.

[68] Juan J Valencia and PN Quested. Thermophysical properties. *Modeling for Casting and Solidification Processing*, page 189, 2001.

[69] Holger Wendland. Piecewise polynomial, positive definite and compactly supported radial functions of minimal degree. *Advances in computational Mathematics*, 4(1):389–396, 1995.

[70] Mingyu Zhang, Hui Zhang, and Lili Zheng. Numerical investigation of substrate melting and deformation during thermal spray coating by SPH method. *Plasma Chemistry and Plasma Processing*, 29(1):55–68, 2009.

[71] T.I. Zohdi. Additive particle deposition and selective laser processing-a Additive particle deposition and selective laser processing-a computational manufacturing framework.

[72] T.I. Zohdi. Additive particle deposition and selective laser processing-a Additive particle deposition and selective laser processing-a computational manufacturing framework. *Computational Mechanics*, (54):171–191, 2014.

Appendix A

Code Layout

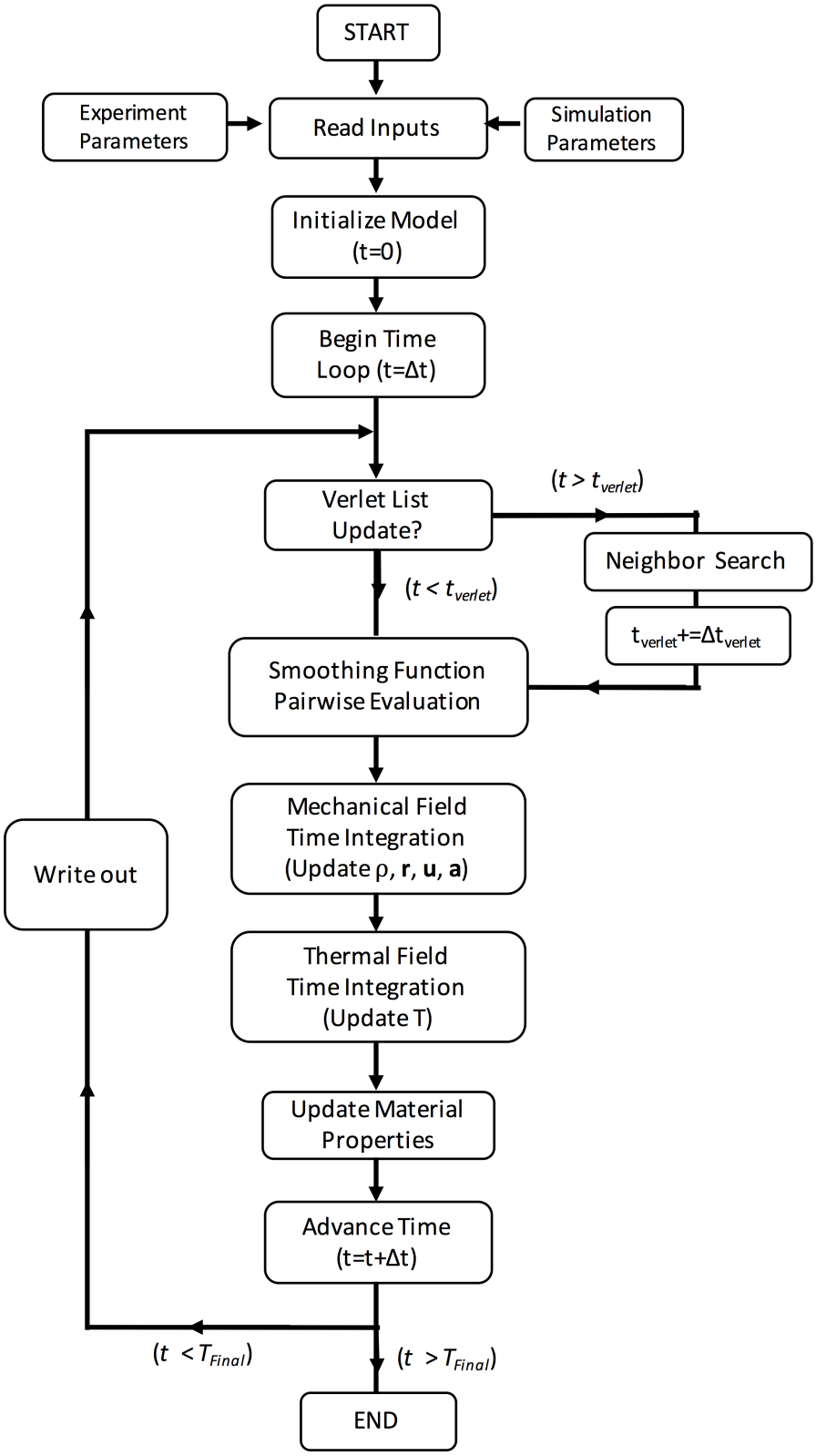
START
Experiment Parameters
Read Inputs
Simulation Parameters
Initialize Model (t=0)
Begin Time Loop (t=Δt)
Verlet List Update?
(t > t_verlet)
Neighbor Search
t_verlet+=Δt_verlet
(t < t_verlet)
Smoothing Function Pairwise Evaluation
Mechanical Field Time Integration (Update ρ, r, u, a)
Thermal Field Time Integration (Update T)
Update Material Properties
Advance Time (t=t+Δt)
Write out
(t < T_Final)
(t > T_Final)
END

Figure A.1

Appendix B

2D Particle Bed Parameter Studies

2D particle bed laser melting parameter studies were performed as described in Section 5.1.1. Additional results from those studies are presented below.

B.0.1 Laser Power Parameter Studies

Plots of the particles bed state at various stages of the scan process for $Laser\ Power = 50W,\ 100W,\ 150W,\ 200W$ are presented below.

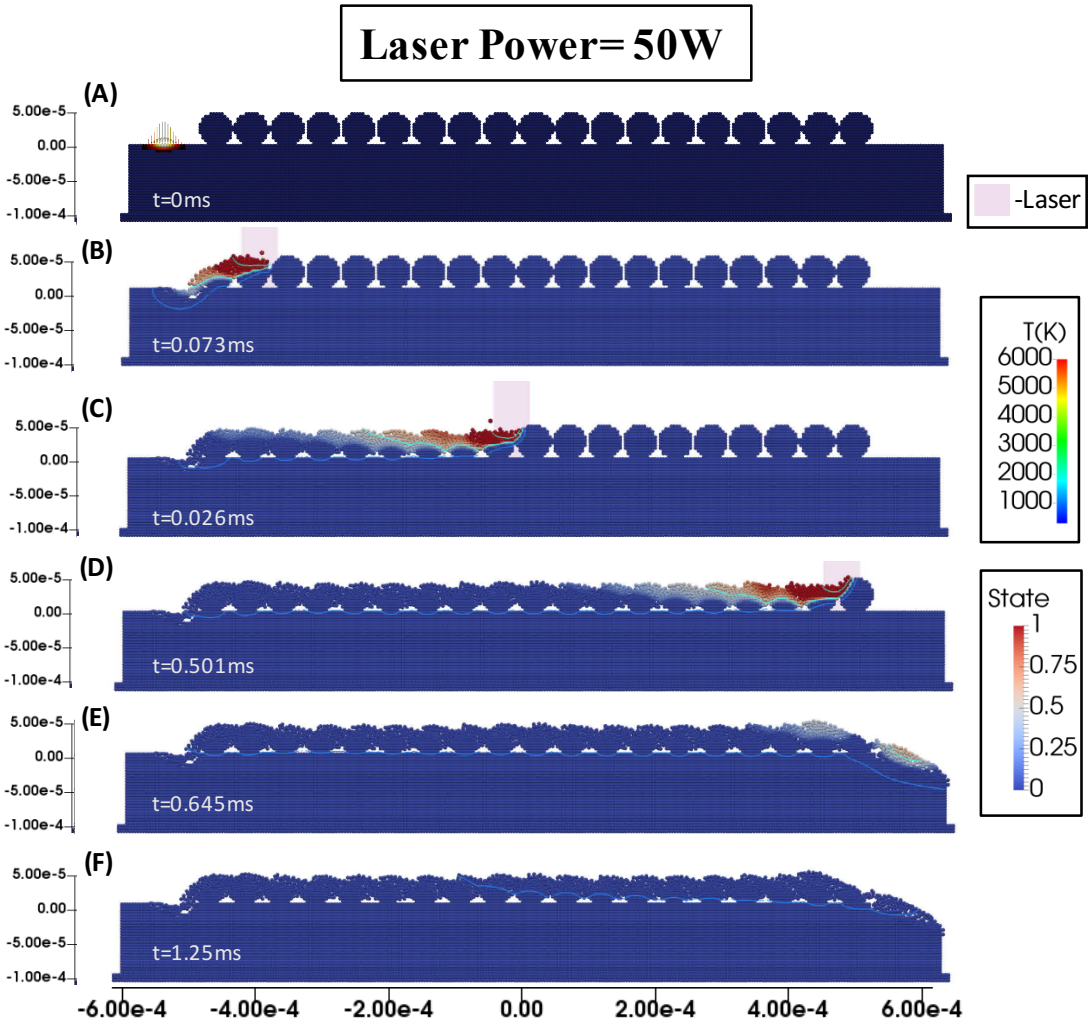

Figure B.1: Plots of the particle bed state at various statges of of the scan process for $Laser\ Power = 50W$.

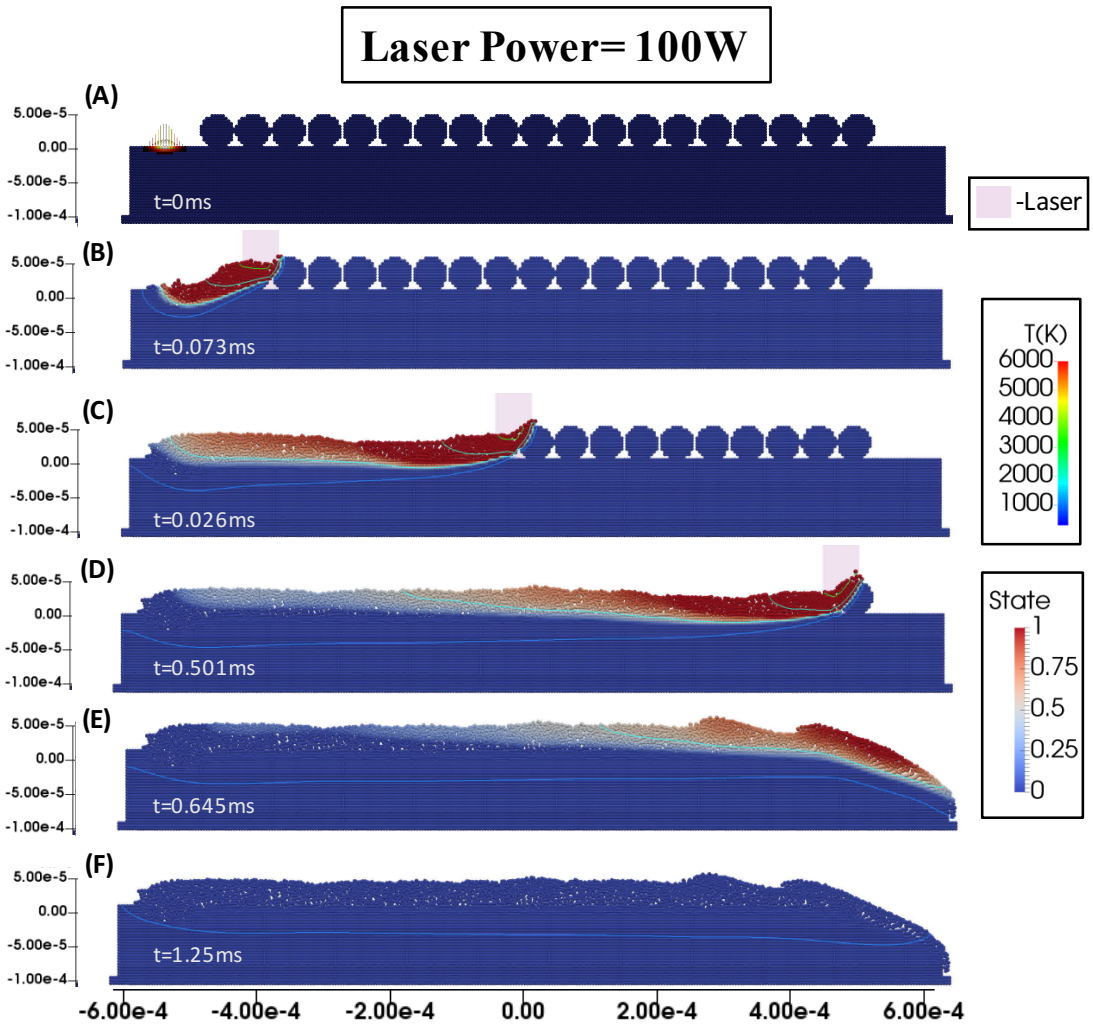

Figure B.2: Plots of the particle bed state at various statges of of the scan process for $Laser\ Power = 100W$.

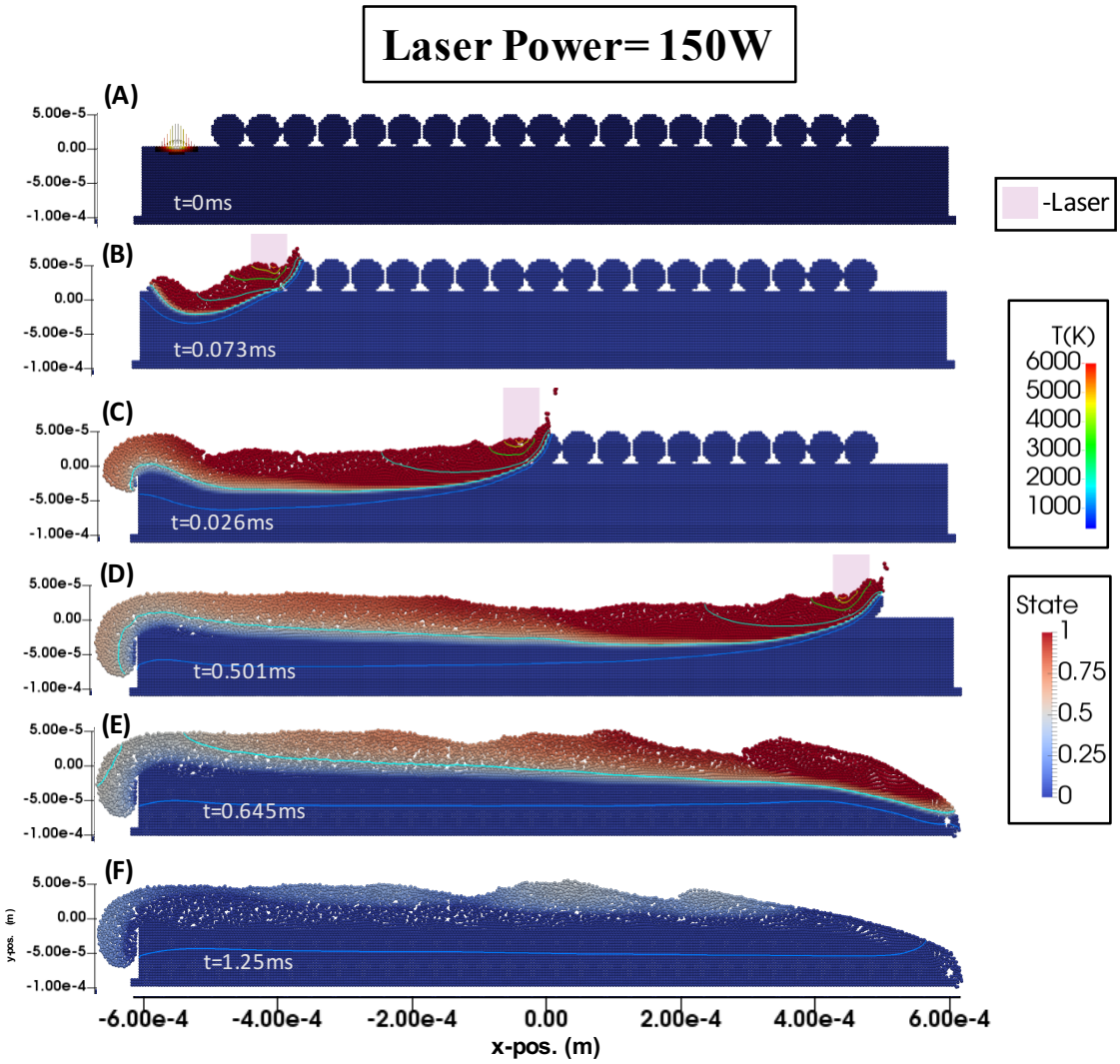

Figure B.3: Plots of the particle bed state at various statges of of the scan process for $Laser\ Power = 150W$.

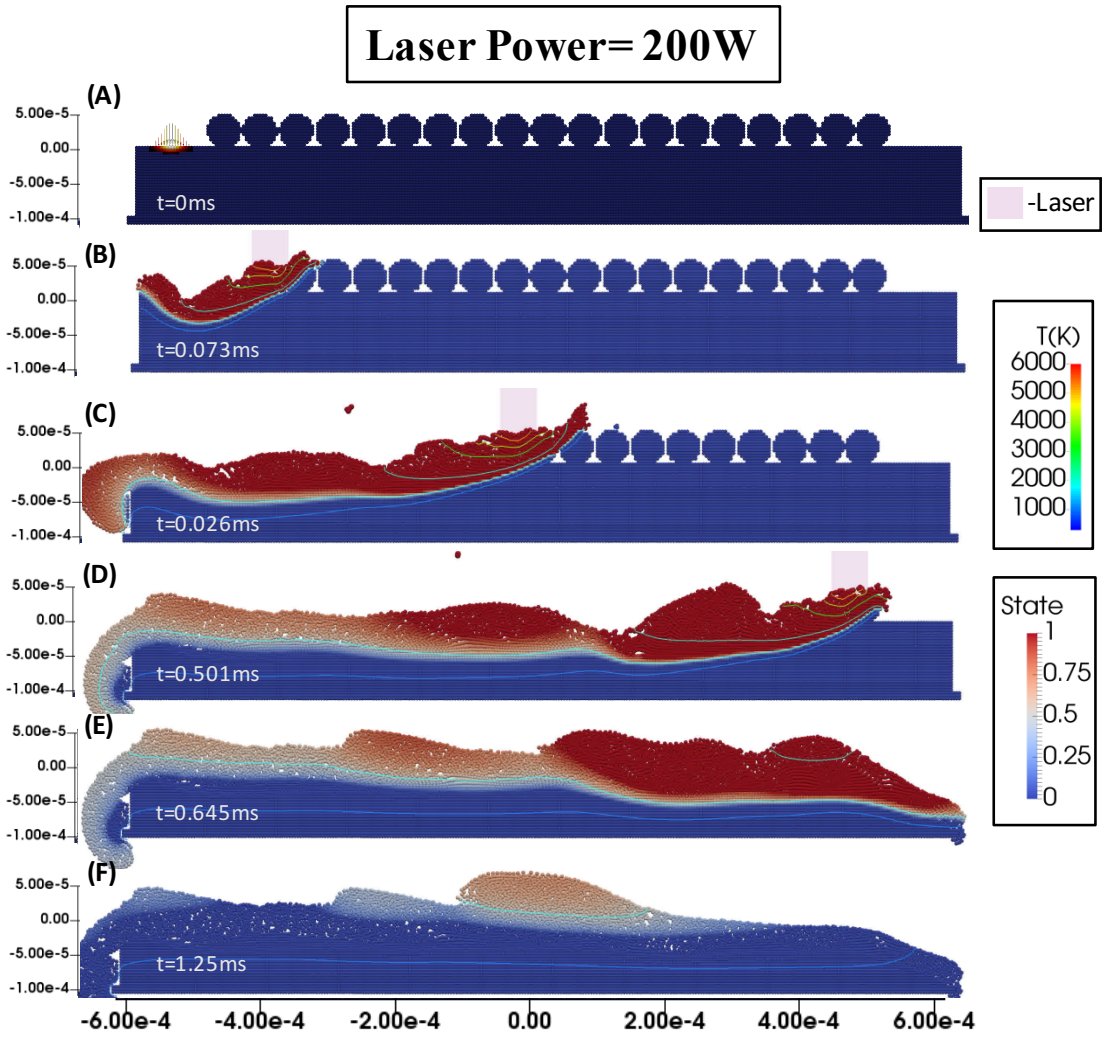

Figure B.4: Plots of the particle bed state at various statges of of the scan process for $Laser\ Power = 200W$.

B.0.2 Powder Particle Radius Parameter Studies

Plots of the powder bed-track state at various stages of a laser scan process for powder particle radii of $r_p = 15\mu m,\ 30\mu m,\ and\ mixed\ 30\mu m\ \&\ 15\mu m$. The $r_p = 25\mu m$ results can be found for the $150W$ laser from the laser power parameter study results.

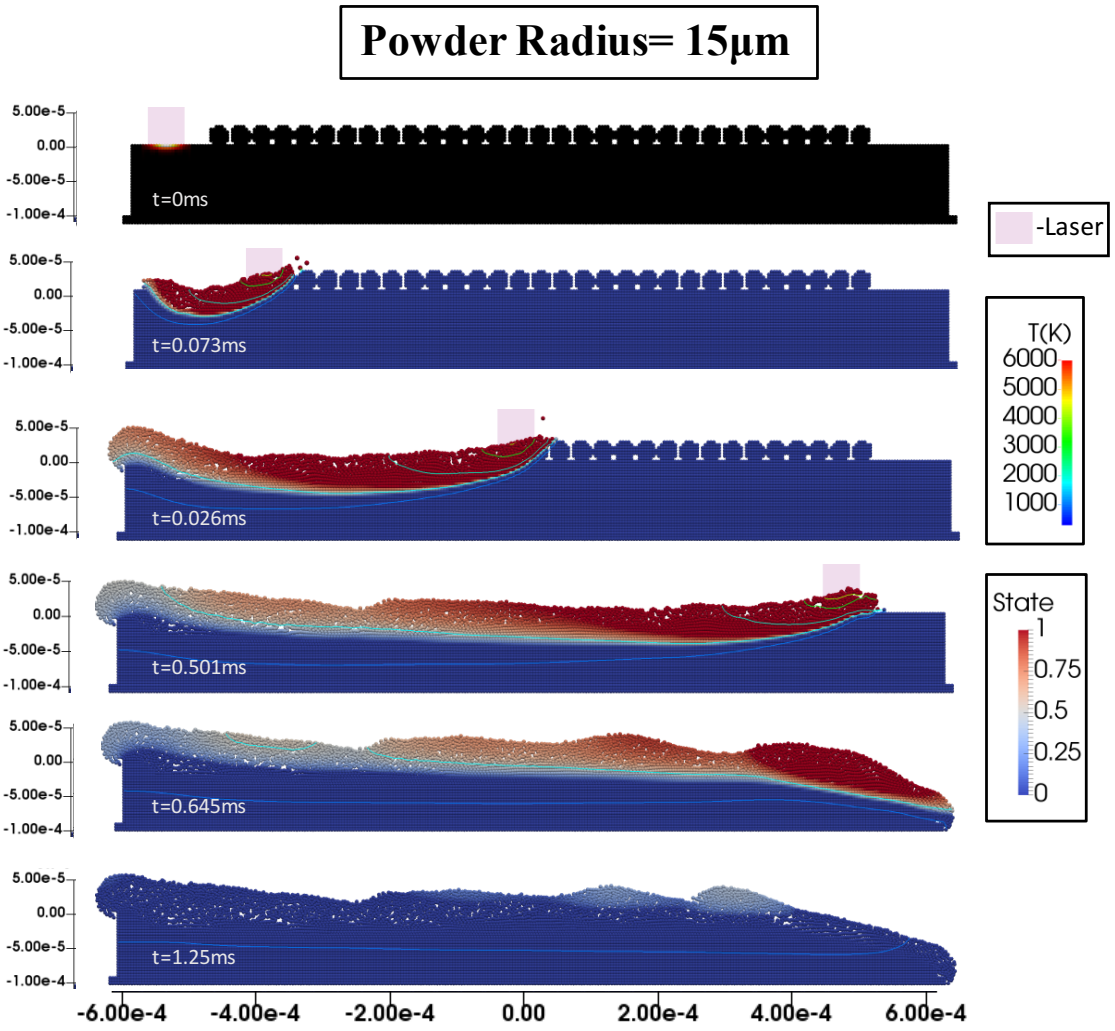

Figure B.5: Plots of the particle bed state at various statges of the scan process for $r_P = 15\mu m$.

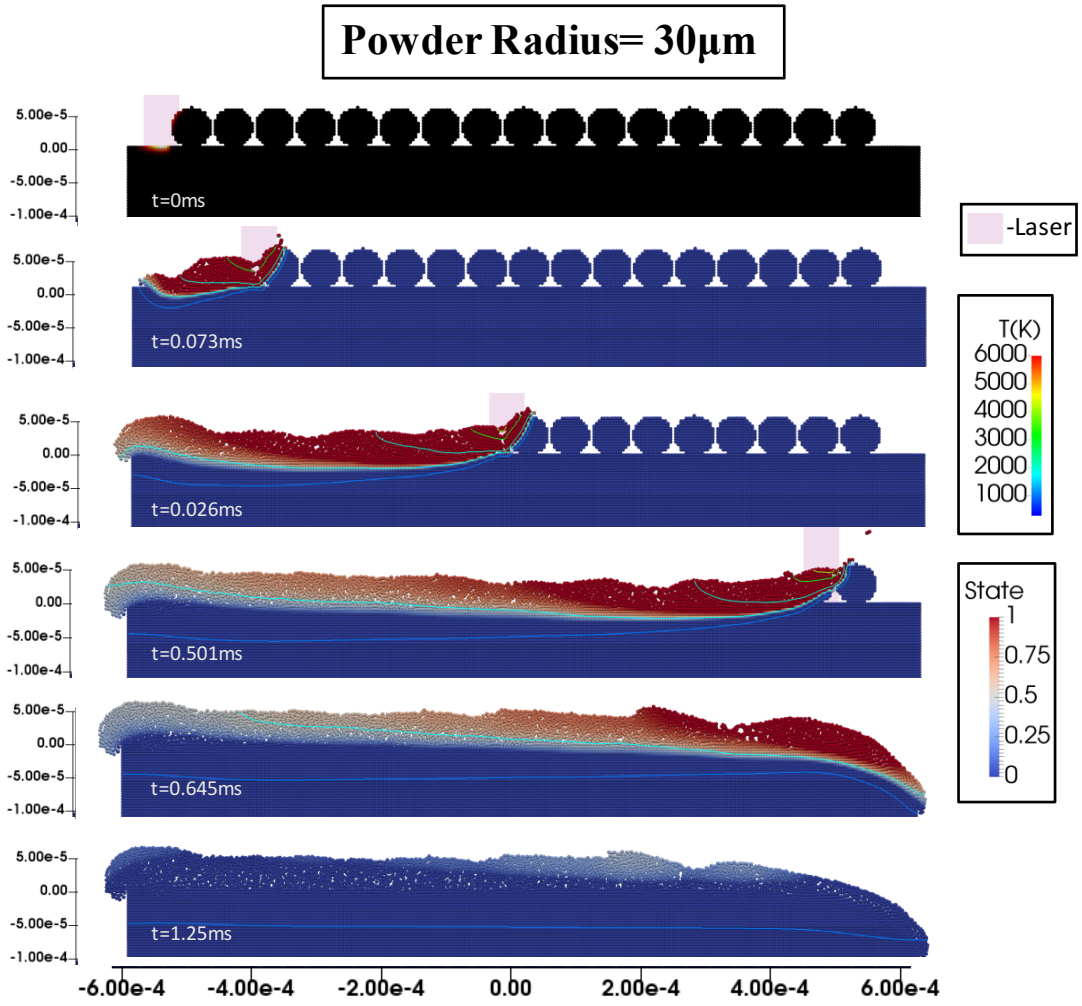

Figure B.6: Plots of the particle bed state at various statges of the scan process for $r_P = 30\mu m$.

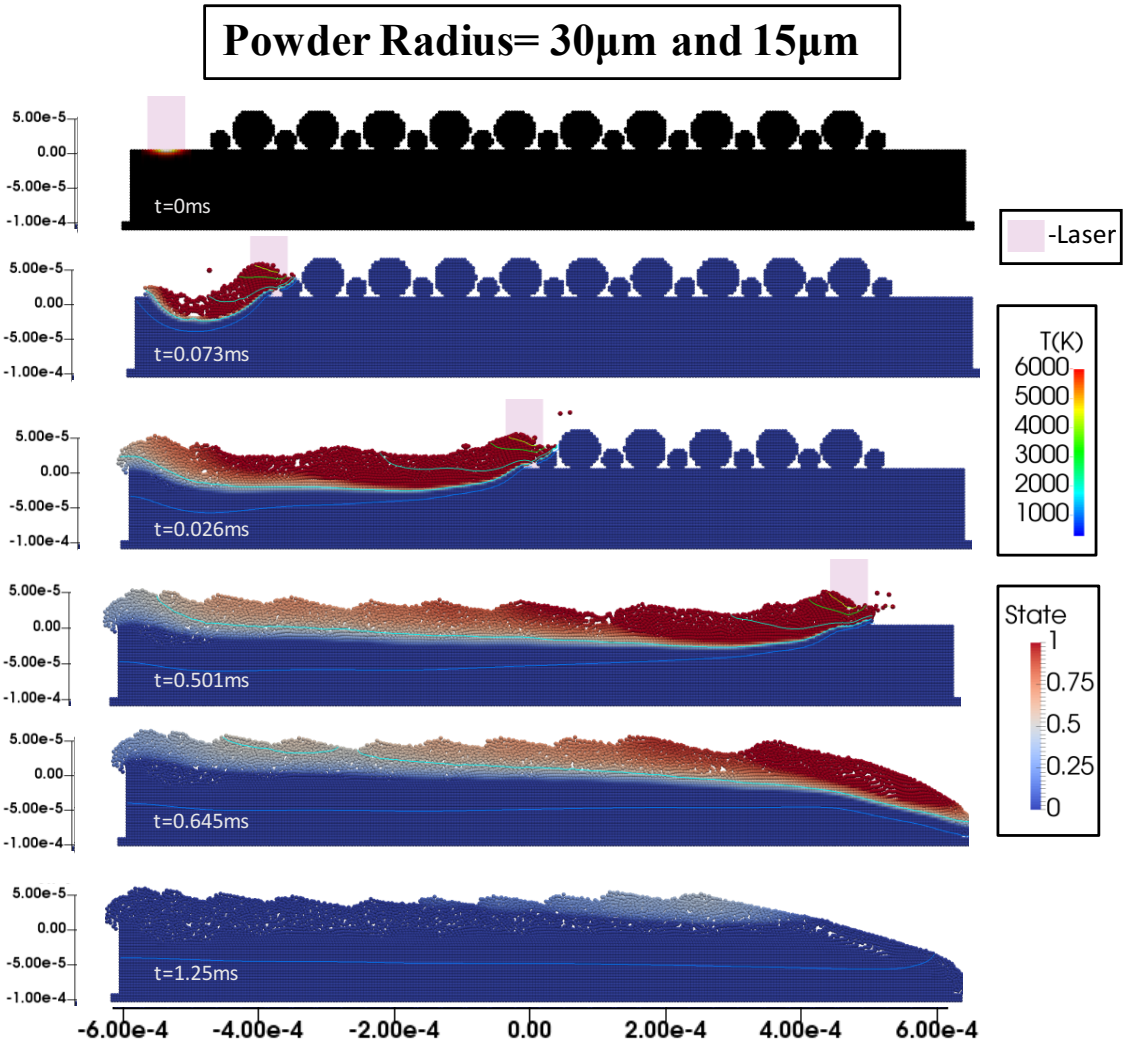

Figure B.7: Plots of the particle bed state at various statges of the scan process for $r_P = 30\mu m$ & $15\mu m$.